Kinetics assessment of the dry reforming of methane over a Ni-La_2O_3 catalyst

Victor Stivenson Sandoval Bohorquez

Tesis presentada como requisito para optar por el título de: Magister en Ingeniería Química

Advisor
Prof. Víctor Gabriel Baldovino Medrano
Doctor en Ingeniería Química

Co–advisors
Prof. Luz Marina Ballesteros Rueda
Doctora en Electroquímica, Ciencia y Tecnología

Edgar Mauricio Morales Valencia
Doctor en Ingeniería Química

Universidad Industrial de Santander
Facultad de Ingenierías Fisicoquímicas
Escuela de Ingeniería Química
Bucaramanga
2021

Acknowledgments

This work was funded by Agencia Nacional de Hidrocarburos –ANH– and Minciencias, Colombia, within the frame of the Project 1102–721–50962: "*Desarrollo de alternativas catalíticas para la reducción y valorización de emisiones de gases de efecto invernadero típicas de pozos y refinerías petroleras por combustión catalítica de VOCs y transformación de CO_2 y CH_4 en gas de síntesis*".

To:

Resurección B. C., Deimer S. B., Leonardo S. B. and Yeferson S. B.

Leidy E. C., Mathias S. E. and Paulett S. E.

Contents

List of Supplementary Information

List of Figures

Supplementary Information

List of Tables

Supplementary Information

Abstract

Title: Kinetics assessment of the dry reforming of methane over a Ni-La_2O_3 catalyst*****

Authors: Victor Stivenson Sandoval Bohorquez******

Keywords: Ni–La_2O_3 solid solution catalyst, dry reforming of methane, synthesis gas, kinetic modelling.

Description:

The dry reforming of methane is a promising technology for the abatement of CH_4 and CO_2. Solid solution Ni–La oxide catalysts are characterized by their long–term stability (100h) when tested at full conversion. The kinetics of dry reforming over this type of catalysts has been studied using both power–law and Langmuir–Hinshelwood based approaches. However, these studies typically deal with fitting the net CH_4 rate hence disregarding competing and parallel surface processes as well as the different possible configurations of the active surface. In this work, we synthesized a solid solution Ni–La oxide catalyst and tested six Langmuir–Hinshelwood mechanisms considering both single and dual active sites for assessing the kinetics of dry reforming and of the competing reverse water gas shift reaction and investigated the performance of the derived kinetic models. In doing this, it was found that: (1) all the net rates were better fitted by a single–site model that considered that the first C–H bond cleavage in methane occurred over a metal−oxygen pair site; (2) this model predicted the existence of a nearly saturated nickel surface with chemisorbed oxygen adatoms derived from the dissociation of CO_2; (3) the dissociation of CO_2 can either be an inhibitory or an irrelevant process, and it can also modify the apparent activation energy for CH_4 activation. These findings contribute to a better understanding of the kinetics of the dry reforming reaction and provide a robust kinetic model for the design and scale–up of the process.

---

*Magister tesis

**Facultad de Ingenierías Fisicoquímicas. Escuela de Ingeniería Química. Advisor: Prof. Víctor Gabriel Baldovino Medrano. Co-advisors: Prof. Luz Marina Ballesteros Rueda & Dr. Edgar Mauricio Morales-Valencia

Resumen

Título: Evaluación cinética del reformado seco de metano sobre un catalizador Ni–La_2O_3*****

Autores: Victor Stivenson Sandoval Bohorquez******

Palabras Clave: catalizador Ni–La_2O_3 en solución sólida, reformado seco de metano, gas de síntesis, modelamiento cinético.

Descripción:

El reformado seco de metano es una tecnología prometedora para la reducción de CH_4 y CO_2. Los catalizadores óxido Ni–La en solución sólida se caracterizan por su prolongada estabilidad (100 h) cuando se ensayan a conversión completa. La cinética del reformado seco sobre este tipo de catalizadores se ha estudiado utilizando enfoques basados tanto en la ley de potencia como en Langmuir–Hinshelwood. Sin embargo, estos estudios generalmente solo se ocupan del ajuste de la velocidad neta de CH_4, por lo tanto, ignoran los procesos superficiales paralelos y competitivos, así como las diferentes configuraciones posibles de la superficie activa. En este trabajo, sintetizamos un catalizador óxido Ni–La en solución sólida y evaluamos seis mecanismos de reacción tipo Langmuir–Hinshelwood considerando sitios activos simples y duales para evaluar la cinética del reformado seco y de la reacción inversa del gas al agua e investigamos el desempeño de los modelos cinéticos resultantes. Al hacer esto, se encontró que: (1) todas las velocidades netas fueron ajustadas adecuadamente por un modelo de un solo sitio que consideraba que la primera escisión del enlace C–H en el metano ocurría en un sitio par metal–oxígeno; (2) este modelo predijo la existencia de una superficie de níquel casi saturada con adatomos de oxígeno quimisorbidos, los cuales eran derivados de la disociación del CO_2; (3) la disociación del CO_2 puede ser un proceso inhibitorio o irrelevante, y también puede modificar la energía de activación aparente del CH_4. Estos hallazgos contribuyen a una mejor comprensión de la cinética de la reacción de reformado seco y proporcionan un modelo cinético robusto para el diseño y escalado del proceso.

---

*Tesis de Maestría

**Facultad de Ingenierías Fisicoquímicas. Escuela de Ingeniería Química. Director: Prof. Víctor Gabriel Baldovino Medrano. Codirectores: Prof. Luz Marina Ballesteros Rueda y Dr. Edgar Mauricio Morales Valencia

Introduction

The conversion of the two most abundant greenhouse gases, CO_2 and CH_4, into commercially valuable syngas, i.e., a mixture of CO and H_2, via the dry reforming of methane ($CH_4 + CO_2 \rightleftharpoons 2H_2 + 2CO$, $\Delta H^0_{298K} = 247.3 kJ.mol^{-1}$, $\Delta G^0_{298K} = 170.9 kJ.mol^{-1}$) remains a promising technology for mitigating climate change. The reaction yields a H_2:CO molar ratio equal to unity which is adequate for the synthesis of methanol, dimethyl ether, and Fisher–Tropsch derived hydrocarbons.(Usman et al., 2015; G. Zhang et al., 2018) Moreover, the reaction offers the possibility to exploit methane deposits that contains significant amounts of CO_2 as well as methane from anaerobic digestion.(Charisiou et al., 2016; Papadopoulou et al., 2012)

In general, the dry reforming of methane competes with parallel reactions such as the reverse water–gas shift reaction or RWGS ($H_2 + CO_2 \rightleftharpoons CO + H_2O$, $\Delta H^0_{298K} = 41.2 kJ.mol^{-1}$, $\Delta G^0_{298K} = 28.6 kJ.mol^{-1}$) which lowers H_2:CO molar ratios, methane dehydrogenation ($CH_4 \rightleftharpoons C + 2H_2$, $\Delta H^0_{298K} = 74.9 kJ.mol^{-1}$, $\Delta G^0_{298K} = 50.8 kJ.mol^{-1}$) and the so–called Boudouard reaction ($2CO \rightleftharpoons C + CO_2$, $\Delta H^0_{298K} = -172.5 kJ.mol^{-1}$, $\Delta G^0_{298K} = -120.1 kJ.mol^{-1}$). The latter two reactions are the sources of the chemisorbed carbon adatoms required for the diffusion and growth of carbon nanotubes.(Gili et al., 2018; Yuan et al., 2016) As shown in **Figure 1**, thermodynamically, dry reforming is promoted by a temperature increase and it prevails over its competing reactions at temperatures higher than 923K. However, the latter reactions are significant up to about 1173K,(Challiwala et al., 2017; Jafarbegloo et al., 2015) with which the formation of water and carbon are virtually inevitable at the typical operational temperatures (873–1073K).

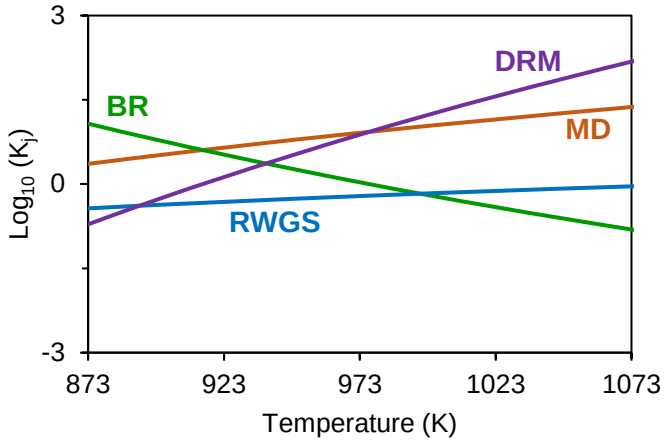

Figure 1. Logarithm of the equilibrium constant (K_j) at different temperatures. Dry reforming of methane (DRM), RWGS, methane dehydrogenation (MD) and Boudouard reaction (BR). The equilibrium constants were estimated with Aspen Plus® (AspenTech) using a model for a Gibbs reactor and the ideal gas package.

Nickel–based catalysts are the most studied catalysts for dry reforming due to their high activity and lower cost as compared to noble metals. Conventional catalysts consisting of supported nickel nanoparticles are prone to deactivation by coking due to the formation of carbon nanotubes because of the high carbon solubility (2.03atom % at 1270K) and diffusion rate in nickel.(Dahal & Batzill, 2014; Gili et al., 2019) In fact, carbon nanotubes can grow either on top of the nickel nanoparticles, tip–growth, or on the interface between the metal nanoparticle and the support, base–growth, depending on both the operational conditions and the metal particle size and shape.(Gili et al., 2019) The tip–growth of carbon nanotubes obstructs both the active sites and the pore network of the support, while the base–growth of carbon nanotubes pushes the metal nanoparticles away from the support hence destroying the catalyst and further plugging the reactor. Most strategies employed to reduce the coking degree of Ni–based catalysts focus on increasing the concentration of surface oxygen by alloying nickel with other metals, e.g. Ni–Co,(Tu et al., 2017) and Ni–Fe,(T. Zhang et al., 2020) using oxide supports with high mobility of oxygen, e.g. CeO_2,(Charisiou et al., 2016; Gonzalez-DelaCruz et al., 2008) ZrO_2,(J. W. Han et al., 2017; Usman

et al., 2015) MnO,(Gili et al., 2018) or by using oxide support able to generate carbonate–type species, e.g. CaO,(Wu et al., 2019; Z. Zhang & Verykios, 1996) La_2O_3,(Bonmassar et al., 2020; Faroldi et al., 2014; Slagtern et al., 1997) and Sm_2O_3.(Osazuwa et al., 2017) Among the latter oxides, it is known that La_2O_3 reacts with CO_2 to form $La_2O_2CO_3$ via acid–base interactions which may promote the removal of carbon species from the metal surface towards the metal–$La_2O_2CO_3$ interphase.(Bonmassar et al., 2020; Faroldi et al., 2014; Manoilova et al., 2004; Singh et al., 2016, 2017; Slagtern et al., 1997; Tsipouriari & Verykios, 1999; S. Wang et al., 2017) Therefore, this type of catalyst has raised considerable interest in the development of a scalable technology involving dry reforming. Particularly, Ni–La_2O_3 formulations obtained via the solid–state thermal decomposition of perovskite precursors (e.g. $LaNiO_3$, La_2NiO_4) have been investigated since this synthesis route can increase the metal–support interaction, hence alleviating the sintering/agglomeration of nickel that is considerable at temperatures above 863K.(Argyle & Bartholomew, 2015; Bonmassar et al., 2020; Singh et al., 2016, 2017)

Several investigations have been devoted to the kinetics of the dry reforming of methane over Ni–based catalysts using either power–law(Bradford & Vannice, 1996; Kim et al., 2007; Sierra-Gallego et al., 2008; Verykios, 2003) or Langmuir–Hinshelwood based models.(Bobrova et al., 2016; Kathiraser et al., 2015; Papadopoulou et al., 2012; Pichas et al., 2010; Tsipouriari & Verykios, 2001; J. Zhang et al., 2009) In general, it has been considered that the reaction involves the following key steps:(Fan et al., 2015; Kathiraser et al., 2015; Papadopoulou et al., 2012) (1) the cleavage of the C–H and C–O bonds of CH_4 and CO_2, respectively; (2) the formation of products (namely, CO, H_2, H_2O) via surface reaction of intermediates derived from the reactant activation, e.g. chemisorbed C, H, O, OH species; and, (3) the desorption of products. The models usually consider that either the cleavage of the C–H bond in methane or another specific surface

reaction can be the rate–determining step (RDS). The models also assume the existence of different types of active sites; particularly, a metallic single–site or a pair of sites located at the metal and at the support have been considered. Other approaches have also considered that one or more chemisorbed species are the most abundant surface intermediate (MASI).(Bobrova et al., 2016; Kathiraser et al., 2015; Papadopoulou et al., 2012; Pichas et al., 2010; Tsipouriari & Verykios, 2001; J. Zhang et al., 2009) Given such a diversity of approaches, a substantial number of alternative and often discordant kinetic models for methane dry reforming exist.(Kathiraser et al., 2015)

Table 1. *Langmuir–Hinshelwood models for Ni–La_2O_3 catalysts.*

MASI		Rate expression	Reference
Ni	**La_2O_3**		
C *	CO_2 #	$r_{CH_4} = \frac{K_{CH_4} k_2 K_{CO_2} k_4 p_{CH_4} p_{CO_2}}{K_{CH_4} k_2 K_{CO_2} p_{CH_4} p_{CO_2} + K_{CH_4} k_2 p_{CH_4} + K_{CO_2} k_4 p_{CO_2}}$ $K_{CH_4} k_2 = 2.61 \times 10^{-3}\, e^{-\frac{4300}{T}}$ $K_{CO_2} = 5.17 \times 10^{-5}\, e^{\frac{8700}{T}}$ $k_4 = 5.35 \times 10^{-1}\, e^{-\frac{7500}{T}}$	(Tsipouriari & Verykios, 2001)
CH_4 C *	CO_2 #	$r_{CH_4} = \frac{K_{CH_4} k_2 K_{CO_2} k_4 p_{CH_4} p_{CO_2}}{K_{CH_4} k_2 p_{CH_4} + K_{CO_2} k_4 p_{CO_2} + K_{CH_4} k_2 K_{CO_2} p_{CH_4} p_{CO_2} + K_{CH_4} K_{CO_2} k_4 p_{CH_4} p_{CO_2}}$ $K_{CH_4} = 1.41 \times 10^{-1}$ $k_2 = 2.23 \times 10^{-4}$ $K_{CO_2} = 1.60 \times 10^{-2}$ $k_4 = 1.32 \times 10^{-2}$	(Sierra-Gallego et al., 2008)
CH_4 C *	#	$r_{CH_4} = \frac{K_{CH_4} k_2 K_{CO_2} k_4 p_{CH_4} p_{CO_2}}{K_{CH_4} k_2 K_3 p_{CH_4} p_{CO_2} + K_{CH_4} k_2 p_{CH_4} + K_{CO_2} k_4 p_{CO_2}}$ $K_1 = 2.98 \times 10^{2}\, e^{-\frac{7500}{T}}$ $k_2 = 1.23 \times 10^{1}\, e^{-\frac{10200}{T}}$ $K_{CO_2} k_4 = 3.40 \times 10^{-2}\, e^{-\frac{7000}{T}}$	(Moradi et al., 2010; Múnera et al., 2007)

Where, r_{CH_4} (mol.g^{-1}.s^{-1}) is the net CH_4 rate, p_i (kPa) the partial pressure of i–th compound, K_{CH_4} (kPa^{-1}) and K_{CO_2} (kPa^{-1}) are the adsorption constants for CH_4 (**R1**) and CO_2 (**R3**), respectively, while k_2 (mol.g^{-1}.s^{-1}) and k_4 (mol.g^{-1}.s^{-1}) are the forward reaction constants for CH_4 dehydrogenation (**R2**) and oxidation of chemisorbed carbon (**R4**), respectively. MASI denotes Most abundant surface intermediate and # represents hereafter an active site over the La_2O_3

Concerning solid solution Ni–La_2O_3 catalysts, the catalytic cycle for the dry reforming of methane is commonly described by the following reaction steps:(Moradi et al., 2010; Sierra-Gallego et al., 2008; Slagtern et al., 1997; Tsipouriari & Verykios, 1999, 2001)

R1: $CH_4 + * \rightleftharpoons CH_4*$; CH_4 adsorption on Ni–sites denoted hereafter as *.

R2: $CH_4* \rightarrow C* + 2H_2$: dehydrogenation of methane leading to chemisorbed C atoms.

R3: $CO_2 + La_2O_3 \rightleftharpoons La_2O_2CO_3$: formation of lanthanum oxycarbonate.

R4: $La_2O_2CO_3 + C* \rightarrow 2CO + La_2O_3 + *$: decomposition of the oxycarbonate species to oxidize the chemisorbed C atoms over Ni–sites for the renewal of the metallic active site. The kinetic models derived in the literature from such a reaction pathway are summarized in **Table 1**. These expressions were developed by assuming that **R2** and **R4** are rate–determining and that the net rate of the chemisorbed C adatoms equals zero, i.e., **R2** – **R4** = 0. In general, the models differ from each other depending on the considered MASI over both the metal and support sites. Besides the disagreements stemming from the latter consideration, one of the critiques that may be posed over these studies is that none of them presented estimations of all kinetic and adsorption parameters. Indeed, some of the authors included in **Table 1**,(Moradi et al., 2010; Múnera et al., 2007) fed their models with parameters taken directly from the literature and this led to inconsistencies such as the determination of elevated activation energies (172–187kJ.mol^{-1}) for the oxidation of chemisorbed carbon (**R4**) which would imply that this step is rather difficult and hence the catalyst will deactivate by coking while they did not present experimental evidence for such behavior. Also, some other authors reported positive values of standard adsorption enthalpy which rarely occur besides reporting standard adsorption entropies that are higher than the limit of thermodynamic consistency (–41.8J.mol^{-1}.K^{-1}).(Boudart & Djega-Mariadassou, 1984; Vannice et al., 1979) In some other instances, the models and their parameters were not subjected to statistical

validation. All these aspects make these expressions inadequate for a robust reactor modelling and design, where is desired a model that describes the catalytic sequence of the dry reforming of methane reaction with a physicochemical and statistical basis.(Abbas et al., 2017; Benguerba et al., 2015; Dehimi et al., 2017)

Considering the above, the objective of this work was to study the kinetics of the dry reforming of methane over a solid solution Ni–La oxide catalyst of proven stability.(Baldovino-Medrano, V. G. Pérez-Martínez, 2003; Baldovino-Medrano & Pérez-Martínez, 2004; Sandoval Bohórquez et al., 2017) Particularly, seven kinetic models based on six plausible Langmuir–Hinshelwood reaction mechanisms were postulated and tested. These models considered that the catalytic cycles could occur over different types of active sites and that they could involve either a single active site or a pair of active sites. Also, all the assessed kinetic models considered the influence of the reaction steps involved in the generation of water via the competing reverse water gas reaction over the kinetics of dry reforming. The results of the investigation led to conclude that the best kinetic model representing the dry reforming of methane stems from the consideration that the cleavage of the C–H bond from methane takes place over a metal−oxygen pair site instead of over a metal–metal site. The model also predicted that the dissociation of CO_2 can inhibit dry reforming under certain reaction conditions by decreasing the apparent activation energy for CH_4 activation. This behavior is related to the dynamics of competition between methane dry reforming and the reverse water gas shift reaction. Overall, the present study helps to build a more robust and deep comprehension of the behavior of solid solution Ni–La oxide catalysts and paves the way for the rigorous modeling and scale–up of methane dry reforming reactors.

Chapter 1. Physicochemical properties and kinetic behavior of the Ni-La_2O_3 catalyst

In this chapter, the results of the physicochemical characterization of the synthesized catalyst, which includes a short–term stability test are first presented. After that, the effect of the operational conditions over the net rates of reactions is studied. Then, a description of the reaction mechanism and of the assumptions made in the formulation of the kinetic model that best represented the kinetic performance of the synthesized solid solution Ni–La oxide catalyst under dry reforming of methane conditions is shown. The experimental methods used in this study are comprehensively described in the Supplementary Information.

1.1. Results and Discussion

In order to guarantee the absence of heat and mass gradients in the reactor, criteria to ensure negligible radial and axial dispersion effects, sufficiently small radial and axial temperature gradients, absence of interfacial and intraparticle mass and heat transfer limitations, and low–pressure drop across the catalytic bed was verified, as summarized in **Table S2**. The details of the performed calculations can be found in the Supplementary Information, Section C. Thus, all rate and selectivity data reported herein are assumed to reflect the intrinsic catalytic events of the dry reforming of the methane over solid solution Ni–La oxide catalysts.

1.1.1. Physicochemical properties of the catalyst. Concerning the crystallinity of the catalyst, the XRD pattern for the as–synthesized solid solution Ni–La oxide presented three phases (**Figure 2A**); namely, tetragonal La_2NiO_4 or so–called Ruddlesden–Popper phase (layered–type perovskites), hexagonal $La(OH)_3$, and cubic NiO whose compositions were 55, 25 and 20wt%, respectively, as determined via semi–quantitative analysis. After the hydrogen reduction treatment made before each catalytic test, the observed phases were cubic Ni and hexagonal $La(OH)_3$ with a

composition of 24 and 76wt%, respectively. According to the above phase compositions, the total concentrations of Ni were 3992 and 4098µmol $Ni.g_{cat}^{-1}$ for the fresh and reduced samples of the catalysts, respectively. These concentrations agreed with the nominal concentration of nickel of the material: 4072µmol $Ni.g_{cat}^{-1}$. Crystallite diameters for NiO in the fresh sample and Ni in the reduced sample were estimated to be 30 and 50nm, respectively, as from calculations done with the Scherrer equation (**eq S2**) using the XRD peaks at 2θ of 37.3° and 44.6°, which corresponds to the diffraction planes for NiO(111) and Ni(111), respectively.(Dorofeev et al., 2012) The larger crystallite diameter for the Ni phase can be related to the fact that ~64mol% out of the total amount of Ni in the reduced sample was due to the reduction of the NiO phase present in the fresh catalyst. This also suggests that the increase in the crystallite size from NiO in the fresh sample to Ni upon reduction can be due to sintering.(Bandrowski et al., 1962; Szekely et al., 1973)

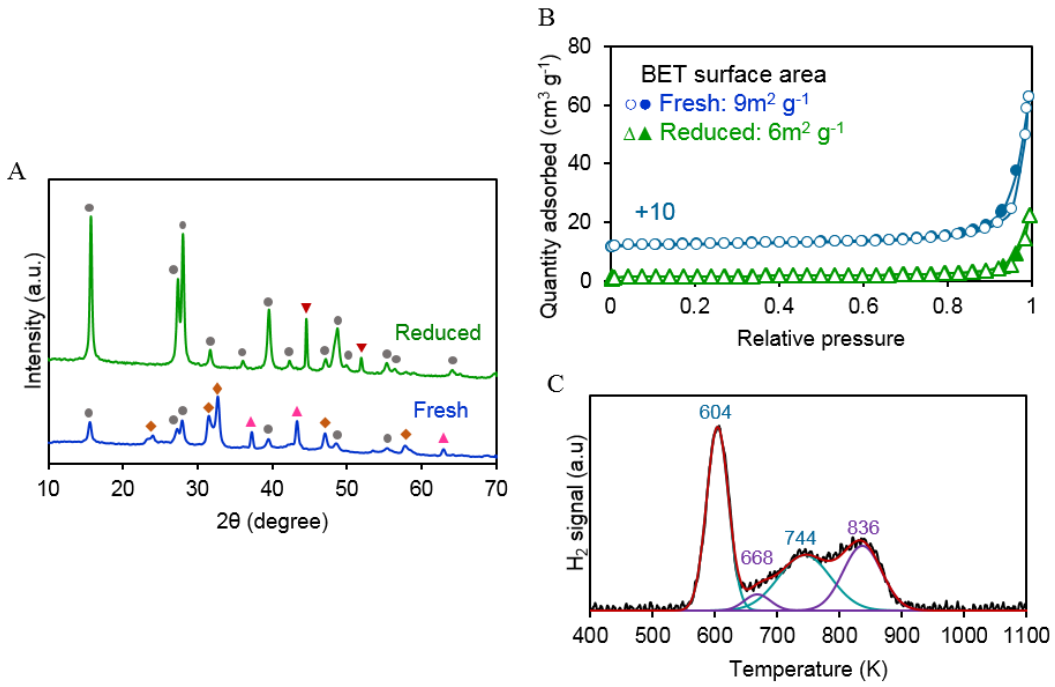

Figure 2. XRD pattern (A) and N_2 physisorption isotherms (B) of fresh (blue) and reduced sample (green, reduction under a H_2 space velocity of 1.7cm^3 g^{-1} s^{-1} and 1023K for 1h with heating rate of 0.083K s^{-1}) as well as the H_2–TPR profile (C) of the fresh catalyst. XRD caption: Hexagonal $La(OH)_3$ (●), tetragonal La_2NiO_4 (♦), cubic NiO (▲) and cubic Ni (▼). N_2 physisorption caption: Adsorption (○Δ) and desorption (●▲) branch.

On the other hand, the presence of $La(OH)_3$ is likely due to the fact that reduction was performed under pure H_2. $La(OH)_3$ is known to decompose to La_2O_3 and $La_2O_2CO_3$ phase under the presence of N_2 and CO_2, respectively, at temperatures above 673K.(Haibel et al., 2018; Ino et al., 1976) Therefore, a Ni–$La_2O_2CO_3$ mixed–phase should be present under the atmosphere of the dry reforming of methane process as demonstrated in previous works.(Bonmassar et al., 2020; Faroldi et al., 2014; Slagtern et al., 1997; Tsipouriari & Verykios, 1999) However, no direct proof from the analysis of spent catalysts is presented herein because of the impossibility of recovering it after the catalytic tests as considering the elevated bed dilution ratios (~99vol%) that were used to avoid temperature gradients in the catalytic bed.

The temperature–programmed reduction profile of the fresh catalyst is shown in **Figure 2C**. The profile displayed four reduction peaks. The first peak, which consumed 1725μmol $H_2.g_{cat}^{-1}$, had its maximum at 604K and was assigned to the reduction of the nickel oxide phase into metallic nickel.(Bandrowski et al., 1962; Szekely et al., 1973) The second peak with an uptake of 183μmol $H_2.g_{cat}^{-1}$ at 668K was ascribed to the reduction of non–stoichiometric oxygen (+δ) in $La_2NiO_{4+\delta}$ to form La_2NiO_4. Where the value of δ was determined to be 0.17 from the corresponding H_2 uptake. The estimated value of δ was within the range reported for this kind of material.(Fontaine et al., 2004) The third peak, which consumed 1229μmol $H_2.g_{cat}^{-1}$ at 744K, was associated with a second NiO reduction peak.(Bandrowski et al., 1962; Manukyan et al., 2015; Szekely et al., 1973) According to the literature, this peak is due to the reduction of bulk NiO in larger oxide particles, where the nucleation rate of metallic Ni from the surface to the bulk NiO and the outward diffusion of water is low at reduction temperatures lower than 700K hence leading to mixtures between NiO–Ni.(Bandrowski et al., 1962; Manukyan et al., 2015; Szekely et al., 1973) In this sense, the noncomplete reduction of NiO in the first peak at 604K yielded a NiO–Ni

product whose composition, as determined from the H_2 uptakes, was 42 and 58mol% of NiO and Ni, respectively. After that, such mixture was totally reduced into metallic Ni in the third reduction step centered at 744K. Finally, the fourth peak with an uptake of 1076μmol $H_2.g_{cat}^{-1}$ and centered at 836K was assigned to the reduction of La_2NiO_4 into Ni and La_2O_3 ($La_2NiO_4 + H_2 \rightleftharpoons Ni + La_2O_3 + H_2O$).(Choisnet et al., 1994; Sierra Gallego et al., 2008) According to the stoichiometry of the above reduction steps and H_2 uptakes, the total concentration of Ni in the sample was 4029μmol $Ni.g_{cat}^{-1}$ from which 73mol% corresponds to NiO. Such values were close to those estimated by XRD hence indicating that the degree of reduction of the sample was about 100%.

Regarding the texture of the catalyst, N_2 physisorption results (**Figure 2B**) showed that both the fresh and the reduced catalyst presented IUPAC's Type II isotherms which are characteristic of macroporous materials.(Thommes et al., 2015) According to the calculations made from the physisorption data, the BET surface area decreased from $9m^2.g_{cat}^{-1}$, C_{BET} = 770, for the fresh catalyst to $6m^2.g_{cat}^{-1}$, C_{BET} = 500, for the reduced catalyst. According to the literature, metal oxides synthesized via the citrate complexing method are composed of agglomerated semispherical–shaped particles, where the macropores are the result of interparticle voids.(Huízar-Félix et al., 2012; Sunde et al., 2016; Vargas et al., 2020) In this context, when the reduction process was performed, the particles of the catalyst sintered, which was evidenced from the XRD results, hence making less macropores.(Bergeret & Gallezot, 2008)

Calculations from H_2 chemisorption data resulted in a concentration of 19μmol $Ni.g_{cat}^{-1}$ at the surface of the catalyst. Accordingly, the dispersion of nickel was 0.46% and the mean particle diameter of nickel was 220nm (**eq S1**). Therefore, there was a four–times difference between the mean crystallite and particle size estimated from the DRX and chemisorption methods, respectively. Such a large difference could either be because of the polycrystalline nature of the

Ni particles (Bergeret & Gallezot, 2008) or because, for the type of catalyst studied herein, the Ni particles are typically encapsulated or incorporated into the oxide matrix of the Ni–La_2O_3 phase (Ro et al., 2018; Slagtern et al., 1997; Z. Zhang & Verykios, 1996). For the latter scenario, only a very small fraction of the reduced metal is exposed on the surface hence yielding such a low H_2 chemisorption capacity as the one determined herein. Whatever the explanation for the differences found between the estimation of particle size from XRD and chemisorption may be, the fact remains that the latter is the most adequate metrics to be considered for interpreting the catalytic behavior.

Finally, to assess the stability of the catalyst under the conditions of the methane dry reforming reaction, two catalytic tests were performed by flowing reactants (CH_4 and CO_2) and both reactants and products (CO and H_2) at 873K for 10h. The results of these tests in terms of the net reaction rates of CH_4 and CO_2 with time on stream demonstrates that both in the absence, **Figure 3A**, and in the presence, **Figure 3B**, of products the net CH_4 rate showed a stable steady–state value of ~0.40mol.kg_{cat}^{-1}.s^{-1}, while the net CO_2 rate displayed a stable steady–state value of ~0.55 and 1.05mol.kg_{cat}^{-1}.s^{-1} in the absence and presence of products, respectively. Therefore, the catalyst did not show deactivation within the sampling space of the current study; a result that agrees with previous findings concerning the behavior of Ni–La_2O_3 catalysts synthesized by the solid–state decomposition of perovskite–type precursors.(Bonmassar et al., 2020; Sierra-Gallego et al., 2008; Singh et al., 2016) Furthermore, this result also shows that the steps for CH_4 activation were not inhibited by the presence of reaction products, while the steps for the CO_2 activation were favored because, as explained below, the larger availability of H_2 in the reactor favors the conversion of this reactant via the RWGS reaction.

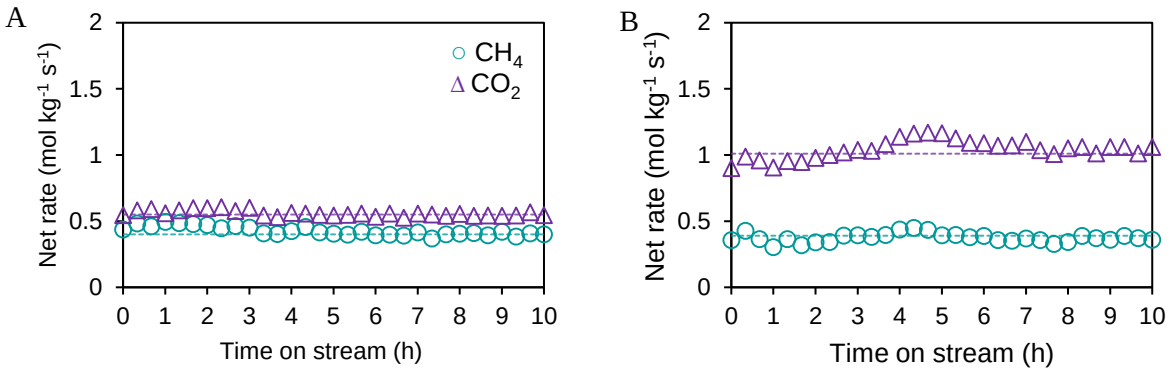

Figure 3. Catalyst activity in the absence (A) and in the presence (B) of H_2 and CO as a function of the time on stream (39.0kPa CH_4, 39.0kPa CO_2, 5.9kPa H_2 (B), 5.9kPa CO (B), balance N_2, 130kPa total pressure and 873K).

Ni–La_2O_3 based catalysts are usually synthesized via either the impregnation of nickel nitrate salts(Kang Li et al., 2019; Tsipouriari & Verykios, 1999; Z. Zhang & Verykios, 1995) or the solid–state decomposition of the perovskites $LaNiO_3$ and La_2NiO_4.(Batiot-Dupeyrat et al., 2005; Messaoudi et al., 2018; Pereñiguez et al., 2012; Rivas et al., 2010; Sierra Gallego et al., 2006, 2008) The latter method can yield solid solution Ni–La oxide catalysts with mean Ni particle sizes lower than 30nm and BET surface areas lower than $20 m^2.g_{cat}^{-1}$, depending on synthesis route of the parent perovskite and stable after (very) long time on stream.(Baldovino-Medrano, V. G. Pérez-Martínez, 2003; Baldovino-Medrano & Pérez-Martínez, 2004; Batiot-Dupeyrat et al., 2005; Messaoudi et al., 2018; Pereñiguez et al., 2012; Rivas et al., 2010; Sandoval Bohórquez et al., 2017; Sierra Gallego et al., 2006, 2008) Thus, although the catalyst precursor herein synthesized was composed of different phases, namely, NiO, La_2NiO_4 and $La(OH)_3$, its solid–state thermal decomposition yielded a Ni(220nm average particle size)–La oxide catalyst with stability comparable to that of the materials obtained from pure perovskite phases.

1.1.2. Overall catalytic performance. First of all, an analysis to classify the reaction products as primary, secondary, or higher is presented using the so–called delplot analysis.(Bhore et al., 1990) For the analysis, when either the selectivity or the selectivity/conversion ratio was

plotted versus the conversion and the intercept at zero conversion give information about primary or secondary products, respectively. The intercept at zero conversion can be evaluated via linear regression. Herein, correlation coefficients R^2 higher than 0.98 were always found (**Figure 4**, solid lines). **Figure 4** shows the first (**Figure 4A**) and second–rank (**Figure 4B**) delplot analysis plots for CH_4. Accordingly, among the three reaction products, H_2O, CO, and H_2, only water was determined to be a secondary product derived from methane because it showed a zero and a finite intercept of 6.9 ± 1.0 in the first– and second–rank plots, respectively. On the other hand, CO and H_2O were determined to be primary products from CO_2 with finite intercepts of 0.6 ± 0.1 and 0.2 ± 0.1, respectively, in the first–rank plots, **Figure 4C**.

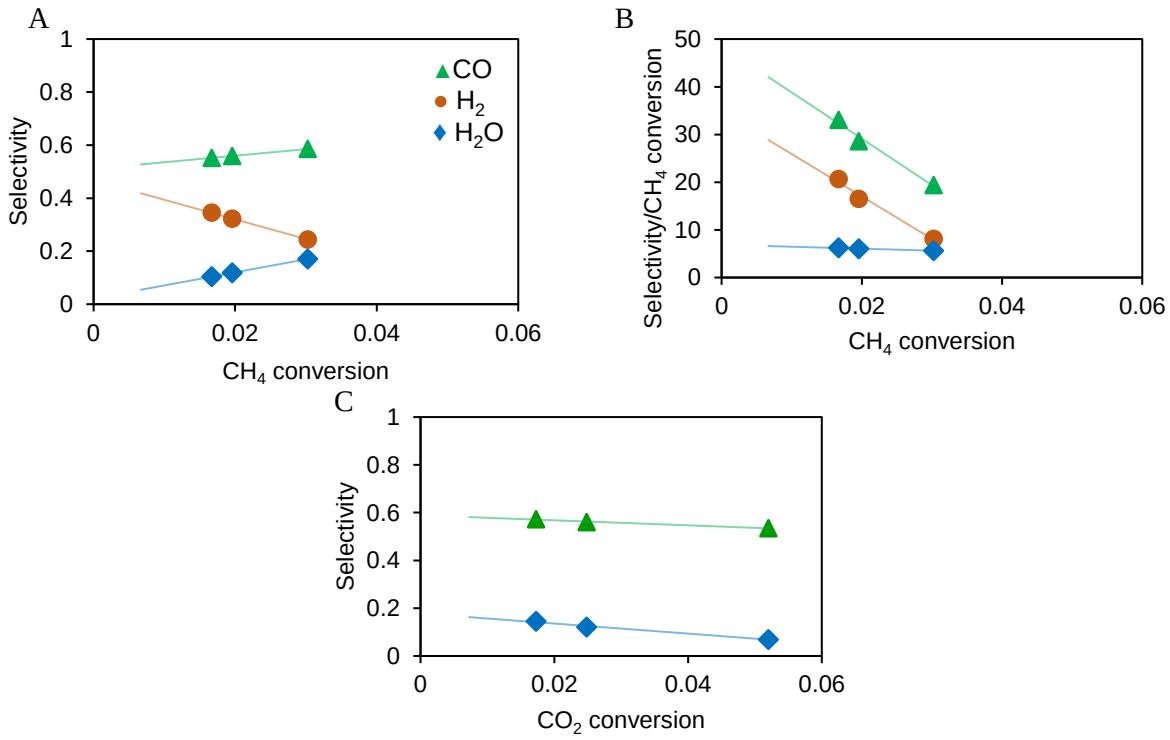

Figure 4. CH_4 (A) and CO_2 (C) first–rank as well as CH_4 second–rank (B) delplot analysis (39kPa of CO_2 (A and B) or CH_4 (C), N_2 balance, 130kPa total pressure and 923K). Symbols represent experimental observations and solid lines were calculated via linear regression, correlation coefficients $R^2 > 0.98$.

The results of the delplot analysis agree with what is known about the occurrence of the reverse water gas shift reaction during dry reforming of methane over Ni–based catalysts. Particularly, experimental(Chin et al., 2013; Tu et al., 2017; Wei & Iglesia, 2004a, 2004b) and molecular simulations(Fan et al., 2015; Kai Li et al., 2018; Xie et al., 2017) studies have reported that the RWGS reaction can proceed through the interaction of chemisorbed hydrogen from the dehydrogenation of CH_4 and oxygen adatoms from the dissociation of CO_2 ($CO_2^* + * \rightleftharpoons CO^* + O^*$) to produce chemisorbed hydroxyl species ($H^* + O^* \rightleftharpoons OH^* + *$) that in turn would react with another hydrogen adatom to produce adsorbed water ($H^* + OH^* \rightleftharpoons H_2O^* + *$).

The influence of the explored reaction conditions, i.e., the sampling space, on the catalyst activity and product distribution is presented below. In general, within the investigated sampling space, the effects of the partial pressure of the reactants and products as well as the temperature over the net reaction rates did not show statistically significant deviations from linearity; i.e., no quadratic and interaction effects (**eq S12**) were detected, see details in the Supplementary Information, Section B. For the following analyses, *t*–Student 95% confidence intervals were estimated for the grand media of the data, i.e., the media of all the performed experimental measurements, to provide a quick idea about which input variables have statistically relevant effects over the estimated reaction rates. In this sense, when the experimental values plotted in these graphs are found outside the estimated confidence interval for the grand media, the effect of the analyzed input variable over the response variable may be considered statistically significant. A similar method was proven to be of utility in previous works.(Caballero et al., 2019)

The effect of the partial pressures of the reactants over the net reaction rates is depicted in **Figure 5**. As observed, increasing the CH_4 pressure from 16.9 to 61.1kPa, **Figures 5A–C**, increased the net rates of CH_4, from 0.36 to 0.84mol.kg_{cat}^{-1}.s^{-1}, CO_2, from 0.57 to 0.98mol.kg_{cat}^{-}

$^{1}.s^{-1}$, CO, from 0.96 to 1.62mol.$kg_{cat}^{-1}.s^{-1}$, and H_2, from 0.40 to 1.01mol.$kg_{cat}^{-1}.s^{-1}$, significantly. In contrast, the net H_2O rate was kept constant at an average of 0.27 ± 0.05mol.$kg_{cat}^{-1}.s^{-1}$, **Figure 5C**. On the other hand, increasing the CO_2 pressure from 16.9 to 61.1kPa, **Figures 5D–F**, kept both the net rates of CO_2 and CO constant at an average of 0.75 ± 0.15mol.$kg_{cat}^{-1}.s^{-1}$ and 1.29 ± 0.28mol.$kg_{cat}^{-1}.s^{-1}$, respectively, while the net H_2O rate increased significantly, from 0.18 to 0.33mol.$kg_{cat}^{-1}.s^{-1}$ and the net H_2 rate decreased significantly, from 1.04 to 0.64mol.$kg_{cat}^{-1}.s^{-1}$, **Figure 5E**. On the other hand, the effect of the CO_2 pressure over the net CH_4 rate was negative, the rate decreased from 0.66 to 0.47mol.$kg_{cat}^{-1}.s^{-1}$, *p*–value of 0.055, **Figure S2A**. In this case, one would say that the effect of this input variable was negative but weak.

The influence of feeding products to the reactor is showed in **Figure 6**. In general, increasing the CO pressure from 0.3 to 11.4kPa, **Figures 6A–C**, did not affect any of the net rates. Therefore, one may conclude that all the reactions are zero–order with respect to CO. Similarly, when the partial pressure of H_2 was increased, from 0.3 to 11.4kPa, **Figures 6D–F**, the net CH_4 rate did not change significantly hence indicating that there was not inhibition of the methane dry reforming reaction by this product. This can also be perceived by comparing the grand media for the net CH_4 rate in the two experimental sets: 0.57 and 0.62mol.$kg_{cat}^{-1}.s^{-1}$ for the first and second one, respectively. Therefore, it is safe to assume that the dry reforming reaction is zero–order with respect to both CO and H_2. On the other hand, such an increment in the H_2 pressure increased significantly the net rates of CO_2, from 0.91 to 1.85mol.$kg_{cat}^{-1}.s^{-1}$, CO, from 1.32 to 2.26mol.$kg_{cat}^{-1}.s^{-1}$, and H_2O, from 0.28 to 1.36mol.$kg_{cat}^{-1}.s^{-1}$, although the H_2 rate decreased significantly, from 0.76 to –0.46mol.$kg_{cat}^{-1}.s^{-1}$, **Figure 6F**.

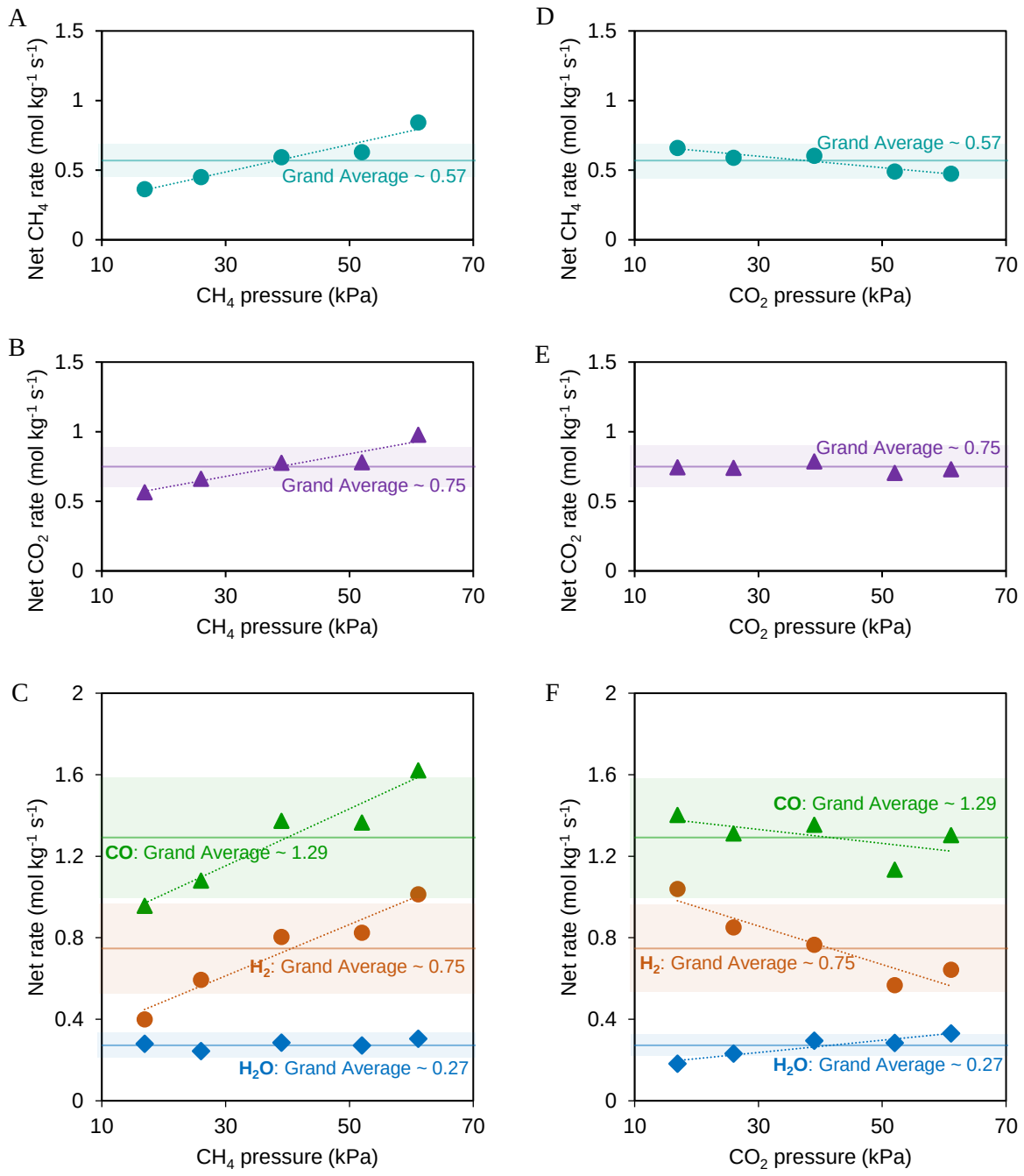

Figure 5. Main effect plots of the reactant pressure for a first set of experiments (conditions: 39kPa CH_4 (A–C) or CO_2 (D–F), balance N_2, 130kPa total pressure and 923K). Shaded areas correspond to *t*–Student confidence intervals for the mean built at a confidence level of 95%, with $n_{exp} - 1$ (i.e. 16) degrees of freedom.

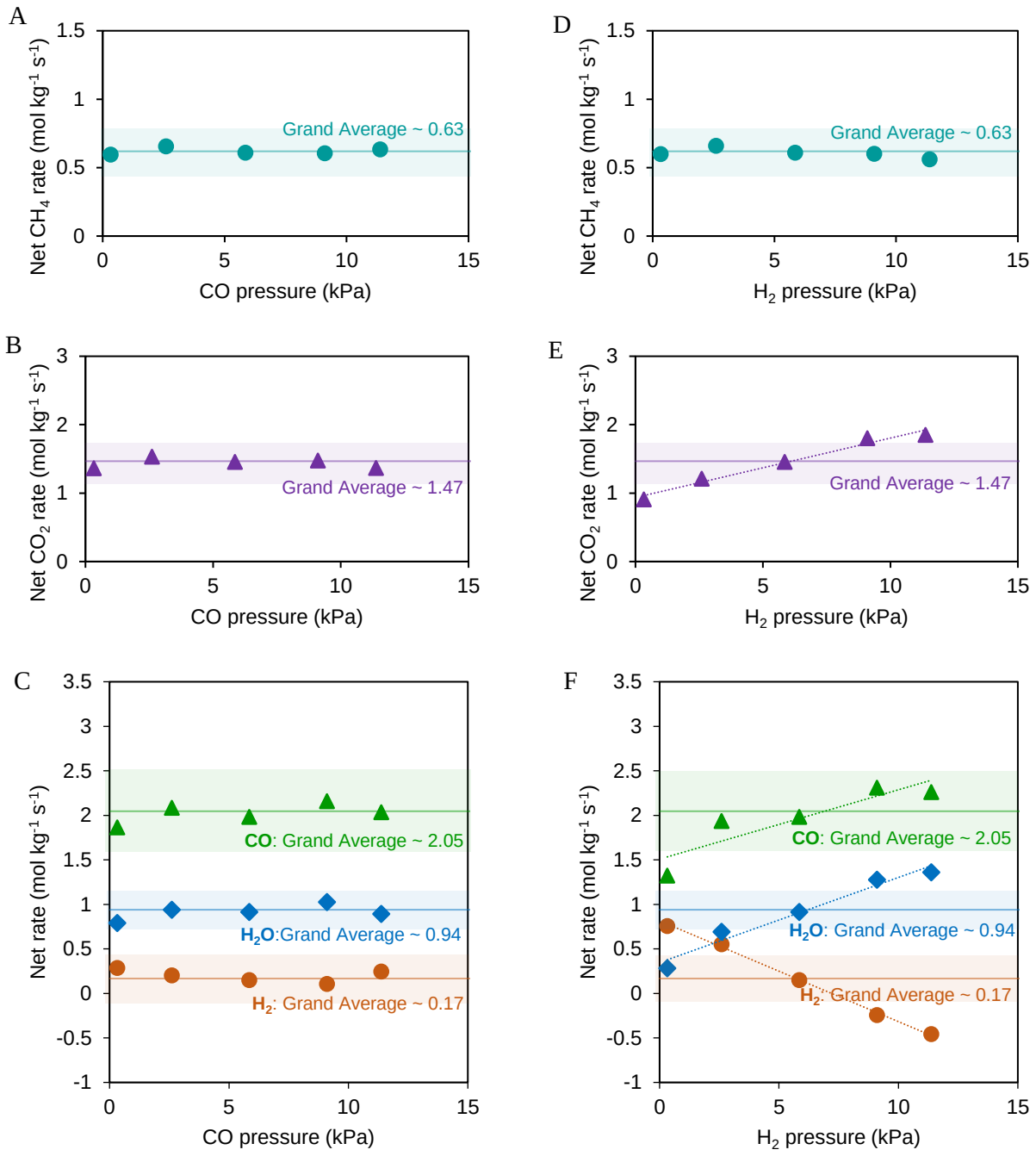

Figure 6. Main effect plots of product pressure for the second experimental set (conditions: 5.9kPa H_2 (A–C) or CO (D–F), 39kPa CH_4, 39kPa CO_2, balance N_2, 130kPa total pressure and 923K). Shaded areas correspond to *t*–Student confidence intervals for the mean built at a confidence level of 95%, with $n_{exp} - 1$ (i.e. 16) degrees of freedom.

These trends were also observed when the two experimental sets were contrasted, in specific, there was an increment from the first to the second set in the grand media of the net rates of CO_2, from 0.75 to 1.47mol.kg_{cat}^{-1}.s^{-1}, CO, from 1.29 to 2.05mol.kg_{cat}^{-1}.s^{-1}, and H_2O, from 0.27 to 0.94mol.kg_{cat}^{-1}.s^{-1}, while the net H_2 rate was reduced from 0.75 to 0.17mol.kg_{cat}^{-1}.s^{-1}. In this instance, the negative values of the net H_2 rates are due to a higher rate of conversion of the product in the RWGS reaction in front of its production rate from the dry reforming of methane reaction. For example, the stoichiometric relationship between the dry reforming of methane and RWGS reaction, as determined with the CH_4/H_2O ratio of the net rates, is 0.40 at 9.1kPa H_2 that, in other words, indicates 0.8mol H_2 produced in the dry reforming per 1mol H_2 converted in the RWGS reaction, so leading to the additional requirements of H_2. It is well–known that products can inhibit catalytic reaction rates because of competitive adsorption over the free active sites of the catalyst, and because of an increase of the reverse reaction rate of the steps involved in the product formation given its higher surface concentration. Taking this into account, the current results suggest that the CO coverage is low enough to avoid the inhibition of the dry reforming and RWGS reactions.

In the literature, the CH_4 conversion rate was reported to be independent of the partial pressure of CO_2, CO and H_2 over the partial pressure range of 5–400kPa for supported Ni(10nm)/MgO(Wei & Iglesia, 2004b), Ni(26nm)/MgO−ZrO_2(Tu et al., 2017) and Ni(30nm)/La_2O_3(Tsipouriari & Verykios, 2001) catalysts. Herein, we found evidence, supported by statistics, that the CO_2 affected weakly the net CH_4 rate while the CO and H_2 did not influence it. It has been reported that nonconfined Ni clusters on the support are more susceptible to oxygen deactivation by promoting the CO_2 dissociation than those embedded in the oxide.(Zuo et al., 2018) In this sense, the discrepancy with the cited reports that discarded the effect of the CO_2 over

the CH_4 conversion rate could be caused by the difference in Ni particle size and, in turn, by the metal–support interactions. Indeed, transmission electron microscopy analysis revealed that for spent solid solution Ni–La_2O_3 catalysts (923–1073K, space velocity = 3–35$cm^3.g^{-1}.s^{-1}$, 10–20kPa for both CH_4 and CO_2) with a mean metal size of 10–30nm there was a continuous layer of $La_2O_2CO_3$ covering the Ni particles.(Bonmassar et al., 2020; Singh et al., 2016) However, such a layer may not exist for the very large Ni particles of the solid solution Ni–La oxide catalyst studied herein.

To further explore the above hypothesis, a thermodynamic analysis of the chemical state of the Ni particles in the synthesized solid solution Ni–La oxide catalyst under the operational conditions was done. The analysis was made considering the free reaction energy required for the formation of bulk NiO with CO_2 ($Ni + CO_2 \rightleftharpoons NiO + CO$) that is related to the CO_2/CO pressure ratio in the reactor according to the following equation:

$$\Delta G^0 = RT \ln\left(\frac{a_{Ni}}{a_{NiO}}\frac{p_{CO_2}}{p_{CO}}\right) \quad (1)$$

Where, a_{Ni} and a_{NiO} refer to the thermodynamic activity of solid Ni and NiO, whose values are the unity for pure phases.(Tu et al., 2017) According to calculations, the free energy ranges from 47 to 48$kJ.mol^{-1}$ under the temperatures (838–1008K) tested herein. With which, the CO_2/CO pressure ratio required for the formation of bulk NiO is between 270–945 which are values significantly higher than those used in the present tests: 2–70. Thus, the bulk Ni atoms belonging to the solid solution Ni–La oxide catalyst should remain in a metallic state while the metal surface atoms should be oxidized under the current reaction conditions. In this sense, it is likely that the net CH_4 rate decrease because of an increment in the oxygen coverage when the CO_2 pressure increase. This behavior has also been observed for a Ni–Co(26nm)/MgO−ZrO_2 catalyst, where the incorporation of cobalt increased the cluster oxophilicity leading to a nearly saturated metal surface

with chemisorbed oxygen adatoms derived from the CO_2 dissociation.(Tu et al., 2017) In such a report, it was shown that an increase of the CO_2 pressure from 5 to 30kPa with 20kPa CH_4 at 873K decreased the forward turnover of CH_4 rate from about 14 to $7s^{-1}$. In our case, the increase of the CO_2 pressure from 26 to 52kPa with 26kPa CH_4 at 873K decreased the forward turnover CH_4 rate (**eq S6**) from 15 to $11s^{-1}$, i.e., the current solid solution Ni–La oxide catalyst would be less sensitive to an increment of CO_2 pressure in comparison to the Ni–Co/MgO−ZrO_2, hence agreeing with the fact that Ni would be less oxophilic in these systems than in a Ni–Co alloy.(Tu et al., 2017)

To summarize, the kinetic measurements showed that the dry reforming of methane reaction (or net CH_4 rate) was (1) promoted by increasing the CH_4 pressure, (2) weakly suppressed by the increment in the CO_2 pressure, and (3) unaffected by the CO and H_2 pressure. Such behavior suggests that the chemisorbed oxygen adatoms are a key intermediate in the catalytic sequence of dry reforming of methane over solid solution Ni–La oxide catalysts. The following section is devoted to further exploring this hypothesis.

1.1.3. Kinetic analysis of the results. ***1.1.3.1. Postulation of reaction mechanisms and kinetic models.*** Six different Langmuir–Hinshelwood reaction mechanisms and seven kinetic models were proposed to analyze the kinetics of methane dry reforming over the synthesized solid solution Ni–La oxide catalyst. These mechanisms were based on both the data collected herein and on the extensive literature on this topic.(Bai et al., 2019; Bonmassar et al., 2020; Fan et al., 2015; Gallego et al., 2016; Gili et al., 2018, 2019; Herrera et al., 2015; Kai Li et al., 2018; Papadopoulou et al., 2012; Slagtern et al., 1997; Tsipouriari & Verykios, 1999, 2001; Tu et al., 2017; Wei & Iglesia, 2004b; Xie et al., 2017; Zhu et al., 2009; Zuo et al., 2018) In this section, the kinetics of the process is analyzed under the light of the model that best fitted the experimental data and fulfilled the thermodynamic consistency criteria, **Table 2**. The competing models are

comprehensively explained in the Supplementary Information, Section E, and summarized in **Table S8**. The selected model was based on a reaction mechanism that considered a single–site mechanism in which, both, CO_2 and CH_4 are activated over Ni–sites (symbolized by *). Specifically, it considers that the first C–H bond cleavage on methane takes places over a metal–oxygen pair site (*–O*, step 1), which is followed by a cascade of C–H cleavage steps until chemisorbed C adatoms (step 2–4). In parallel to this, CO_2 is adsorbed (step 9) and dissociated into chemisorbed CO and O (step 5); afterward, the interaction between chemisorbed C and O adatoms produces another molecule of CO (step 6). Finally, the interaction of chemisorbed H and O adatoms produce OH species (step 7) which react with another H adatom to yield water (step 8).

Table 2. *Dry reforming and RWGS reaction steps with corresponding stoichiometric numbers.*

Step	Elementary step	Dry reforming	RWGS	Kinetic descriptor
1	$CH_4 + O^* + * \rightleftharpoons CH_3^* + OH^*$	1		k_1, K_1
2	$CH_3^* + * \rightleftharpoons CH_2^* + H^*$	1		k_2, K_2
3	$CH_2^* + * \rightleftharpoons CH^* + H^*$	1		k_3, K_3
4	$CH^* + * \rightleftharpoons C^* + H^*$	1		k_4, K_4
5	$CO_2^* + * \rightleftharpoons CO^* + O^*$	1	1	k_5, K_5
6	$C^* + O^* \rightleftharpoons CO^* + *$	1		k_6, K_6
7	$H^* + O^* \rightleftharpoons OH^* + *$	–1	1	k_7, K_7
8	$OH^* + H^* \rightleftharpoons H_2O^* + *$		1	k_8, K_8
9	$CO_2 + * \rightleftarrows CO_2^*$	1	1	K_{CO_2}
10	$H_2 + * + * \rightleftarrows H^* + H^*$	–2	1	K_H
11	$CO + * \rightleftarrows CO^*$	–2	–1	K_{CO}
12	$H_2O + * \rightleftarrows H_2O^*$		–1	K_{H_2O}
	Global reaction			
A	$CH_4 + CO_2 \rightleftharpoons 2CO + 2H_2$	1		
B	$CO_2 + H_2 \rightleftharpoons CO + H_2O$		1	

Key to symbols: *, an unoccupied metal site; #, an unoccupied oxide site; $\rightleftarrows$, a quasi–equilibrated step; and $\rightleftharpoons$, a reversible step; k_n and K_n are the forward reaction rate constant and the reaction equilibrium coefficient of the n–th elementary reaction step

The CO_2, CO, H_2 and H_2O (i–th species) adsorption steps were assumed to be quasi–equilibrated (**eq 2**). Specifically, dissociative adsorption of H_2 on Ni–sites were considered (**eq 3**). All the adsorbed reactants and product as well as the reaction intermediates; namely, CH_3, CH_2, CH, C, O and OH (j–th species), were accounted for the metal site balances (**eq 4**):

$$[i^*] = K_i \frac{p_i}{p^0} [*] \tag{2}$$

$$[H^*] = \sqrt{K_H \frac{p_{H_2}}{p^0}} [*] \tag{3}$$

$$[*]_{tot} = \sum[i^*] + \sum[j^*] + [*] \tag{4}$$

Where, p_i is the partial pressure of the i–th species, p^0 the standard pressure (1bar or 100kPa), $[i^*]$ is the surface concentration of i–th species over a Ni–site, $[*]$ is the concentration of unoccupied metal sites and $[*]_{tot}$ is the total concentration of active sites that was determined to be 19μmol $Ni.g_{cat}^{-1}$ from H_2 chemisorption. The reaction rate constant for the reverse reactions (k_n^r) was expressed by the forward reaction rate constant (k_n^f) and the reaction equilibrium coefficient (K_n):

$$k_n^r = \frac{k_n^f}{K_n} = \frac{k_n}{K_n} \tag{5}$$

The pseudo–steady state approximation was applied to the concentration of the intermediates (j–th species), i.e., their net production rate was set equal to zero.(Otyuskaya et al., 2018; Rajkhowa et al., 2017) With this, the following system of differential–algebraic equations (or DAE) was obtained:

$$\frac{dF_{CH_4}}{dw} = -k_1 \frac{p_{CH_4}}{p^0} [O^*][*] + \frac{k_1}{K_1} [CH_3^*][OH^*] \tag{6}$$

$$\frac{dF_{CO_2}}{dw} = -k_5 [CO_2^*][*] + \frac{k_5}{K_5} [CO^*][O^*] \tag{7}$$

$$\frac{\mathrm{dF_{CO}}}{\mathrm{dw}} = k_5[\mathrm{CO_2^*}][*] - \frac{k_5}{\mathrm{K_5}}[\mathrm{CO^*}][\mathrm{O^*}] + k_6[\mathrm{C^*}][\mathrm{O^*}] - \frac{k_6}{\mathrm{K_6}}[\mathrm{CO^*}][*] \tag{8}$$

$$2\frac{\mathrm{dF_{H_2}}}{\mathrm{dw}} = k_2[\mathrm{CH_3^*}][*] - \frac{k_2}{\mathrm{K_2}}[\mathrm{CH_2^*}][\mathrm{H^*}] + k_3[\mathrm{CH_2^*}][*] - \frac{k_3}{\mathrm{K_3}}[\mathrm{CH^*}][\mathrm{H^*}] + k_4[\mathrm{CH^*}][*] - \frac{k_4}{\mathrm{K_4}}[\mathrm{C^*}][\mathrm{H^*}] - k_7[\mathrm{H^*}][\mathrm{O^*}] + \frac{k_7}{\mathrm{K_7}}[\mathrm{OH^*}][*] - k_8[\mathrm{OH^*}][\mathrm{H^*}] + \frac{k_8}{\mathrm{K_8}}[\mathrm{H_2O^*}][*] \tag{9}$$

$$\frac{\mathrm{dF_{H_2O}}}{\mathrm{dw}} = k_8[\mathrm{OH^*}][\mathrm{H^*}] - \frac{k_8}{\mathrm{K_8}}[\mathrm{H_2O^*}][*] \tag{10}$$

$$k_1\frac{\mathrm{p_{CH_4}}}{\mathrm{p^0}}[\mathrm{O^*}][*] - \frac{k_1}{\mathrm{K_1}}[\mathrm{CH_3^*}][\mathrm{OH^*}] - k_2[\mathrm{CH_3^*}][*] + \frac{k_2}{\mathrm{K_2}}[\mathrm{CH_2^*}][\mathrm{H^*}] = 0 \tag{11}$$

$$k_2[\mathrm{CH_3^*}][*] - \frac{k_2}{\mathrm{K_2}}[\mathrm{CH_2^*}][\mathrm{H^*}] - k_3[\mathrm{CH_2^*}][*] + \frac{k_3}{\mathrm{K_3}}[\mathrm{CH^*}][\mathrm{H^*}] = 0 \tag{12}$$

$$k_3[\mathrm{CH_2^*}][*] - \frac{k_3}{\mathrm{K_3}}[\mathrm{CH^*}][\mathrm{H^*}] - k_4[\mathrm{CH^*}][*] + \frac{k_4}{\mathrm{K_4}}[\mathrm{C^*}][\mathrm{H^*}] = 0 \tag{13}$$

$$k_4[\mathrm{CH^*}][*] - \frac{k_4}{\mathrm{K_4}}[\mathrm{C^*}][\mathrm{H^*}] - k_6[\mathrm{C^*}][\mathrm{O^*}] + \frac{k_6}{\mathrm{K_6}}[\mathrm{CO^*}][*] = 0 \tag{14}$$

$$-k_1\frac{\mathrm{p_{CH_4}}}{\mathrm{p^0}}[\mathrm{O^*}][*] + \frac{k_1}{\mathrm{K_1}}[\mathrm{CH_3^*}][\mathrm{OH^*}] + k_5[\mathrm{CO_2^*}][*] - \frac{k_5}{\mathrm{K_5}}[\mathrm{CO^*}][\mathrm{O^*}] - k_6[\mathrm{C^*}][\mathrm{O^*}] + \frac{k_6}{\mathrm{K_6}}[\mathrm{CO^*}][*] - k_7[\mathrm{H^*}][\mathrm{O^*}] + \frac{k_7}{\mathrm{K_7}}[\mathrm{OH^*}][*] = 0 \tag{15}$$

$$k_1\frac{\mathrm{p_{CH_4}}}{\mathrm{p^0}}[\mathrm{O^*}][*] - \frac{k_1}{\mathrm{K_1}}[\mathrm{CH_3^*}][\mathrm{OH^*}] + k_7[\mathrm{H^*}][\mathrm{O^*}] - \frac{k_7}{\mathrm{K_7}}[\mathrm{OH^*}][*] - k_8[\mathrm{OH^*}][\mathrm{H^*}] + \frac{k_8}{\mathrm{K_8}}[\mathrm{H_2O^*}][*] = 0 \tag{16}$$

Where, the number two on the left term in **eq 9** corresponds to the stoichiometric coefficient in the dissociative H_2 adsorption (step 10 in **Table 2**) since the right term corresponds to the net H species rate, i.e., $2\,\mathrm{r_{H_2}} = \mathrm{r_{H^*}}$. The temperature dependence of the rate and equilibrium coefficients were expressed by the Arrhenius (**eq 17**) and van't Hoff (**eq 18**) equations, respectively:

$$k_\mathrm{n} = \mathrm{A_n}\,\mathrm{e}^{-\frac{\mathrm{E_{a,n}}}{\mathrm{RT}}} \tag{17}$$

$$\mathrm{K_n} = \mathrm{e}^{\frac{\Delta \mathrm{S_n^0}}{\mathrm{R}}}\,\mathrm{e}^{-\frac{\Delta \mathrm{H_n^0}}{\mathrm{RT}}} \tag{18}$$

Where, for the n–th reaction, A_n is the pre–exponential factor, $E_{a,n}$ the activation energy, ΔS_n^0 the standard reaction or adsorption entropy, ΔH_n^0 the standard reaction or adsorption enthalpy, T the reaction temperature, and R the universal gas constant. As it can be noted, this model accounted for eight rate coefficients, eight surface reaction equilibrium coefficients and four adsorption coefficients, with which the total number of kinetic parameters to be estimated equals forty. In order to reduce the number of the parameters to be estimated during the solution of the system of equations, the transition state theory (or TST) together with statistical thermodynamics was used to determinate the pre–exponential factors as well as the standard reaction and adsorption entropies of the model. This is explained in detail in the Supplementary Information, Section D. These parameters were kept fixed during the regression of models, with which, the number of adjustable parameters was halved.

1.1.3.2. Analysis of the solution of the kinetic models. The estimates for activation energies and standard surface reaction and adsorption enthalpies obtained from the weighted regression of the best kinetic model are presented in **Table 3**. **Table S9** shows these estimates for the competing models. The agreement between the experimental and calculated net rates with corresponding *F*–values and BIC is depicted in **Figure 7**. As observed, the model showed an *F*–value for the global significance of the regression that exceeded the tabulated *F*–value of 2.79. Furthermore, all parameters were estimated statistically significant with *t*–values ranging from 30 to 300, which are larger than the tabulated *t*–value of 1.96 as well as with very narrow confidence intervals. This model was the one that best described the experimental net rates, as it can be noted by comparing its parity diagram in **Figure 7** to that of the other models in **Figure S5**, and displayed the highest *F*–value and lowest BIC (**eq S46**), which implies the best fitting of the data.

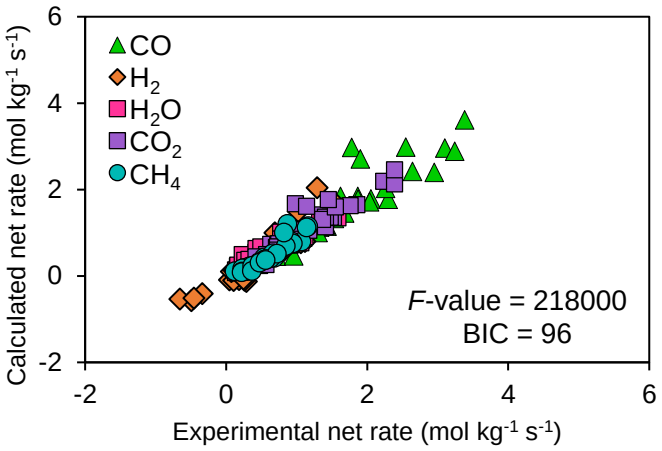

Figure 7. Parity diagram for comparing the experimental and calculated net rates of reactants conversion and products formation.

The physicochemical analysis of the kinetic and adsorption parameters showed that all adsorption enthalpies and entropies presented thermodynamic consistency (**eq S41–S45**) and both forward and reverse activation energies ($\Delta H_n^0 = E_{a,n}^f - E_{a,n}^r$) in the model were within the range of thermodynamic consistency proposed by Santacesaria(Santacesaria, 1997) which goes from 21 to 210kJ.mol^{-1}. Moreover, the calculated dry reforming and RWGS overall standard reaction entropies for the developed model were equal to 286 and 32J.mol^{-1}.K^{-1}, respectively, and they were in agreement with the experimental data; namely, 284.5 and 33.0J.mol^{-1}.K^{-1} at 923K for the dry reforming and the RWGS reactions, respectively.(Çengel & Boles, 2015) Similarly, the model displayed an overall dry reforming and RWGS standard reaction enthalpy of 260 ± 2 and 35 ± 1kJ.mol^{-1}, respectively, which is consistent with the experimental data; namely: 260.3 and 35.8kJ.mol^{-1} at 923K for the dry reforming and the RWGS reactions, respectively.(Çengel & Boles, 2015)

Table 3. *Kinetic parameters with their t–Student confidence intervals built at a 95% confidence level.*

Kinetic descriptor	A_n (kg.mol^{-1}.s^{-1})	$E_{a,n}$ (kJ.mol^{-1})	ΔS_n^0 (J.mol^{-1}.K^{-1})	ΔH_n^0 (kJ.mol^{-1})
k_1, K_1	1.4×10^{9}	93 ± 1	–41	–10 ± 1
k_2, K_2	7.1×10^{13}	90 ± 3	34	63 ± 2
k_3, K_3	6.1×10^{13}	83 ± 3	49	57 ± 2
k_4, K_4	3.1×10^{15}	90 ± 3	12	–28 ± 1
k_5, K_5	1.2×10^{13} (3×10^{14})[a]	66 ± 2	34	–53 ± 1
k_6, K_6	2.8×10^{13} (8×10^{13})[a]	95 ± 5	–2	–37 ± 2
k_7, K_7	7.4×10^{13}	89 ± 3	2	28 ± 1
k_8, K_8	4.1×10^{11} (2×10^{11})[a]	48 ± 3	–53	–27 ± 1
K_{CO_2}			–89	–13 ± 1
K_H			–51	–65 ± 1
K_{CO}			–94	–89 ± 3
K_{H_2O}			–96	–76 ± 2
DRM			286	260 ± 2
RWGS			32	35 ± 1

Pre–exponential factors for LH reactions according to Dumesic et al.(Dumesic et al., 1993): 10^{11}kg.mol^{-1}.s^{-1} for mobile transition state with rotation; 10^{13}kg.mol^{-1}.s^{-1} for mobile transition state without rotation; and 10^{15}kg.mol^{-1}.s^{-1} for immobile transition state without rotation.

[a] Pre–exponential factor estimated with the methodology proposed by Campbell et al.(Campbell et al., 2013)

In general, the estimated pre–exponential factors (**eq S50**) were identical to those reported by Dumesic et al.(Dumesic et al., 1993) and estimated with the methodology proposed by Campbell et al.(Campbell et al., 2013), **Table 3**. Similarly, the activation energies, as well as the standard reaction and adsorption enthalpies in this model, matched those reported in microkinetic modelling studies,(Dehimi et al., 2017; Herrera et al., 2015; Xie et al., 2017) molecular simulations over Ni surfaces,(Fan et al., 2015; Foppa et al., 2017; Z. Han et al., 2019; Kai Li et al., 2018; Zhu et al., 2009; Zuo et al., 2018) and experimental data.(Tu et al., 2017; Wei & Iglesia, 2004b) For example, the activation energy for the oxygen–assisted C–H bond cleavage (step 1, **Table 2**) was in close agreement with the experimental value of 95kJ.mol^{-1} for Ni–Co catalyst(Tu et al., 2017) and microkinetic studies of 88−93kJ.mol^{-1} for Ni–based catalysts.(Herrera et al., 2015; Xie et al., 2017) Likewise, the reaction enthalpy for this step matched with the value of –8.0kJ mol^{-1} reported

elsewhere.(Foppa et al., 2017) The values of the activation energy and reaction enthalpy for the sequential H–abstraction reactions (step 2–4) were in the range of 65–130kJ.mol^{-1},(Dehimi et al., 2017; Fan et al., 2015; Herrera et al., 2015; Kai Li et al., 2018; Xie et al., 2017) and even their trend, i.e., a decrease in the activation energy upon the first H–abstraction and increase again for the last H–scission was similar to those predicted with molecular simulations.(Fan et al., 2015; Z. Han et al., 2019; Kai Li et al., 2018; Zuo et al., 2018) Moreover, the steps involved in H_2O production (steps 7 and 8) displayed activation energies of 89 ± 3 and 48 ± 3kJ.mol^{-1}, respectively, which were close to the values of 104 and 41kJ.mol^{-1} reported in microkinetic models.(Herrera et al., 2015; Xie et al., 2017) Also, the corresponding standard enthalpies of 28 ± 1 and -27 ± 1kJ.mol^{-1} were in the reported range from 18 to 74kJ.mol^{-1} and –52 to 41kJ.mol^{-1}, respectively.(Dehimi et al., 2017; Fan et al., 2015; Herrera et al., 2015; Kai Li et al., 2018; Xie et al., 2017) Finally, the current model presented energy barriers for the CO_2 dissociation (step 5) and carbon oxidation (step 6) of 66 ± 2 and -95 ± 5kJ.mol^{-1}, respectively, that agreed with the ranges reported in the literature and that goes from 65–89kJ.mol^{-1} and from 54–153kJ.mol^{-1}, respectively.(Fan et al., 2015; Z. Han et al., 2019; Herrera et al., 2015; Kai Li et al., 2018; Xie et al., 2017; Zuo et al., 2018)

1.1.3.3. Coverage and degree of rate control analysis. Surface coverages ($\theta_i = [i^*]/[*]_{tot}$) for the intermediates CO, H, O, OH and free Ni–sites are depicted in **Figure 8**. The coverages predicted for CO_2, H_2O, and CH_x were lower than 0.001 so they were excluded from the analysis. It can be observed that by increasing the CH_4 pressure from 16.9 to 61.1kPa (**Figure 8A**, solid lines), the CO, H adatoms, OH and free sites coverages increased 1, 6%, 1% and 10%, respectively, while the O atoms coverage decreased 18%, respectively. However, raising the CO_2 pressure by the same magnitude as the one for CH_4 (**Figure 8B**, dashed lines) led to the opposite behavior with

similar values, except for OH coverage that stayed constant at 0.01. These trends show that an excess and a reduction of the oxygen adatoms over the surface, respectively, may either hinder or promote the net rates of CH_4, CO, and H_2.

Once the products are co–fed (**Figure 8B**), the grand media for the oxygen coverage decreased 21%, while for H, free sites and OH coverages increased 12%, 6%, and 1%, respectively. Particularly, raising the H_2 pressure from 0.3 to 11.4kPa (**Figure 8B**, solid lines) increased the OH, H and free sites coverages 1%, 19% and 8%, respectively, which caused the promotion in the RWGS reaction as observed experimentally. Even though the oxygen coverage decreased, it remained as the most abundant surface intermediate. Thus, the mechanism of CH_4 activation was unaffected. Of course, an increase of the H_2 partial pressure above 11.4kPa should lead to a reduction in the O coverage enough to shift the C−H bond cleavage from occurring on a metal−oxygen pair site (*−O*) to a metal−metal pair site (*−*). This, together with the larger increase in free site coverage than that of OH, may explain why raising the H_2 pressure did not inhibit the net rate of CH_4 within the sample space considered herein. On the other hand, rising the CO partial pressure from 0.3 to 11.4kPa (**Figure 8B**, dashed lines) led to an increase in the CO and free site coverages of 4% and 1%, respectively, while the O coverage decreased 5%, values that suggest the promotion of the CO oxidation into CO_2, thus inhibiting the net CO_2 rate. However, it was estimated that the reduction in the calculated net CO_2 rate was only 8% and statistically insignificant in the range of CO pressure studied (0.3−11.4kPa). Similarly, the low CO coverage as well as these small variations in the surface state caused by its pressure increase did not affect the net CH_4 rate, as said earlier.

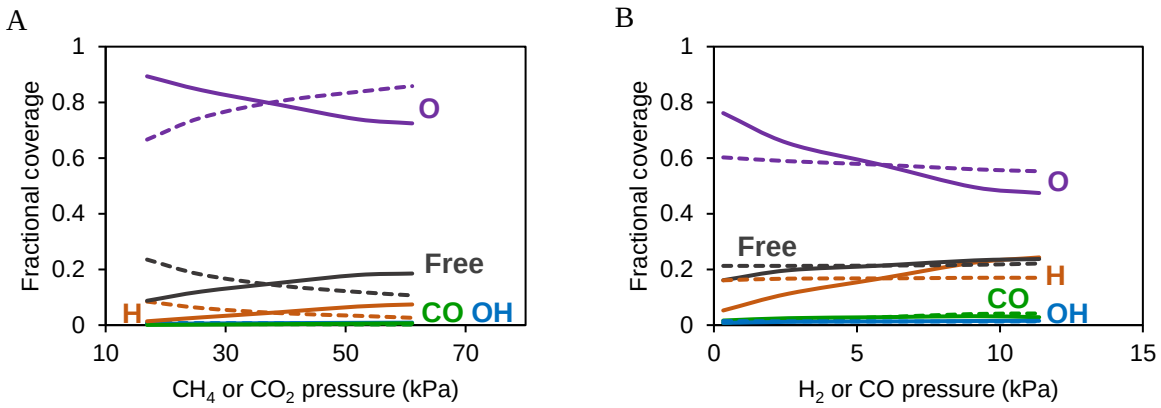

Figure 8. Calculated Ni surface coverage plotted versus reactants (A) and products (B) partial pressure. Dashed lines indicate the effect of the CO_2 (A) and CO (B) pressure. (conditions: 39.0kPa CH_4, 39.0kPa CO_2, 5.9kPa H_2 (B), 5.9kPa CO (B), balance N_2, 130kPa total pressure and 873K).

Figure 9 depicts the results of the degree of rate control (**eq S47**) analysis at different operational conditions. It was found that only two steps out of the twelve considered in the mechanism presented non–zero X_{RC} values; namely, the oxygen–assisted CH_4 activation step, step 1 in **Table 2**, and the CO_2 dissociation step, step 5. The degree of rate control values of the steps changed markedly in both the presence and absence of H_2 and CO, as observed in **Figure 9**. Herein, it was found that the C–H bond activation step presented a DRC value of 1.37 at 39.0kPa of both CH_4 and CO_2 and 923K, which was reduced to 1.00 once 5.9kPa of both H_2 and CO were co–fed. Also, at such conditions, the CO_2 dissociation steps showed a degree of rate control value of –0.40 in the absence of products, which changed to zero in the presence of products. Therefore, the oxygen–assisted C–H cleavage was the rate–determining step (or RDS) under all experimental conditions in agreement with that reported for Ni(Tu et al., 2017; Wei & Iglesia, 2004b) and Pt(Chin et al., 2013; Wei & Iglesia, 2004a) clusters, while the CO_2 dissociation was an inhibition step (i.e., $X_{RC} < 0$) for the dry reforming reaction that became irrelevant by co–feeding products. As observed, raising the CO_2 partial pressure from 16.9 to 61.1kPa (**Figure 9A**, dashed lines), increased the inhibition degree of the CO_2 dissociation by 22% as well as the degree of rate control

value for the CH_4 activation step by 30%. Such a trend is explained by the increment in oxygen coverage that nearly saturates the nickel active sites (**Figure 8A**). On the other hand, increasing the CH_4 partial pressure (**Figure 9A**, solid lines) led to the opposite behavior, a decrease of 22% in the inhibition effect of the CO_2 dissociation while the degree of rate control value for CH_4 activation was reduced at the same proportion towards the unity as it corresponds to a reaction determining step. This was due to the fact that a raise of the CH_4 pressure reduced oxygen coverage (**Figure 8A**) at the same time that it increased that of the free sites leading to an adequate metal–oxygen (*−O*) pair site balance, thus reducing the inhibition effect caused by the excess of chemisorbed O adatoms. Indeed, increasing the H_2 pressure from 0.3 to 5.9kPa (**Figure 9B**, D; solid lines) made the CO_2 dissociation step irrelevant, while the DRC for CH_4 activation step reached unity. The change in the CO_2 dissociation step from inhibiting to irrelevant after co–feeding products affected directly the CH_4 apparent activation energy (**eq S49**) that is representative for dry reforming. Indeed, the CH_4 apparent activation energy increased from 65 ± 10 to 91 ± 10kJ.mol^{-1} when products were co–fed. On the other hand, increasing the CO pressure did not change the degree of rate control values (**Figure 9B**, dashed lines).

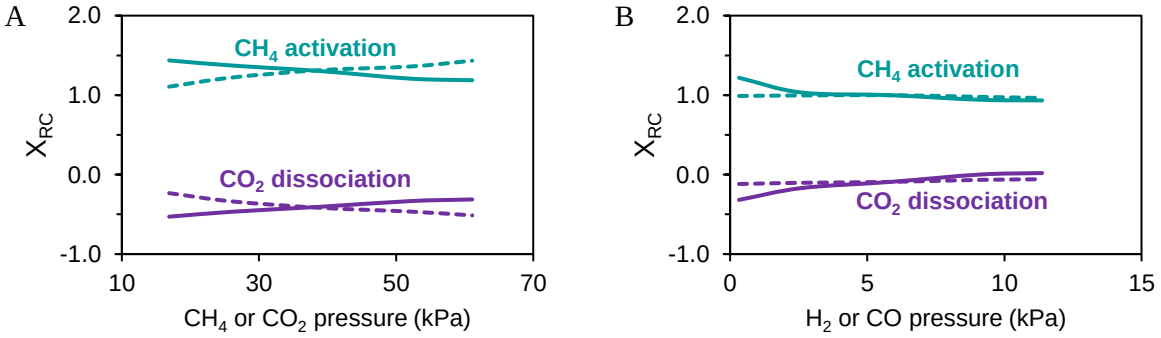

Figure 9. Calculated DRC of the oxygen–assisted CH_4 activation and CO_2 dissociation. Dashed lines indicate the effect of the CO_2 (A) and CO (B) pressure. (conditions: 39.0kPa CH_4, 39.0kPa CO_2, 5.9kPa H_2 (B), 5.9kPa CO (B), balance N_2, 130kPa total pressure and 873K).

Finally, the changes in apparent activation energy when a reaction is carried out in the presence of reaction products was recently discussed by Harris et al.(Harris et al., 2020), who found that the apparent activation energy of the NO oxidation (NO + ½ O_2 ⇌ NO_2) over a Cu–based catalyst increased from 22 to 45kJ.mol^{-1} when NO_2 was co–fed with the reactants. The authors reported that NO_2 inhibits the forward rate and demonstrated that this unaccounted NO_2 inhibition effect, in reactions performed without products in the input stream, breaks the differential reactor approximation (or CSTR) and leads to errors in the measured kinetic parameter. However, in this case, the inhibition of CO and H_2 were not significant (i.e., zero–order). In order to explain this trend, let us rearrange **eq S47** by taking the partial derivative with respect to the temperature on both sides of the division term and by using the concept stated in **eq S49** which leads to **eq 19**. This expression shows that the contribution of the n–th elementary step to the apparent activation (termed as $\left[E_i^{app}\right]_n$) of the net rate of i–th compound is its activation energy ($E_{a,n}$) weighted by its degree of rate control:

$$X_{RCi,n} = \frac{\frac{\partial \ln r_i}{\partial T}}{\frac{\partial \ln k_n}{\partial T}} = \frac{\left[E_i^{app}\right]_n}{E_{a,n}} \implies \left[E_i^{app}\right]_n = X_{RCi,n} E_{a,n} \qquad (19)$$

This expression is a generalized form of that reported by Jørgensen & Grönbeck(Jørgensen & Grönbeck, 2017) and Mao & Campbell(Mao & Campbell, 2019). In this way, as mentioned above, the grand average for the DRC value of the CO_2 dissociation step on the dry reforming was –0.4 that change to zero in presence of products, the former value together with its activation energy of 66 ± 2kJ.mol^{-1} leads to a contribution of –26 ± 1kJ.mol^{-1}, which is exactly the observed energy gap in apparent activation energies. Therefore, the measured increment in activation energy was due to a change in the degree of rate control by feeding products, in specific, a shift from an inhibitory to an irrelevant step. This behavior can also be interpreted as a change in the kinetic

behavior as the dry reforming reaction approaches equilibrium, where the availability of H_2 is higher, so kinetic measurements performed at different conversion levels can lead to different interpretations of the CO_2 influence over the reaction, and even a discrepancy in the kinetic parameters.

All the evidence presented above validates the working hypothesis that oxygen is a key intermediate in the catalytic sequence of dry reforming of methane over solid solution Ni–La oxide catalysts obtained via thermal decomposition of a perovskite–type precursor. Indeed, the kinetic modelling showed that such as intermediate almost saturated the nickel surface and allowed the C–H bond activation of methane to occur over a metal−oxygen pair site ($CH_4 + O^* + * \rightleftharpoons CH_3^* + OH^*$) instead of a metal−metal pair site ($CH_4 + * + * \rightleftharpoons CH_3^* + H^*$) as it occurs over supported Ni catalyst.(Tsipouriari & Verykios, 2001; Tu et al., 2017; Wei & Iglesia, 2004a, 2004b) In this sense, we suggest that such difference is due to the Ni particle size domain and, in turn, to the presence of exposed Ni particles which are more susceptible to oxidation, i.e., a more oxophilic metal surface, caused by a poor interaction between nickel and lanthanum oxide. The latter agrees with the fact that the CO_2 dissociates over a metal site ($CO_2^* + * \rightleftharpoons CO^* + O^*$) instead of the support (#) or interphase Ni−La_2O_3 (^{IN}) sites (**Table S8**). Therefore, the metal particle size and the metal−support interactions, which depend on the synthesis route of the catalyst, may influence the activation mechanism of the C–H and C–O bonds of both CH_4 and CO_2, respectively.

Chapter 2. Conclusions

This contribution made a kinetic assessment of the dry reforming of methane reaction over a solid solution Ni–La oxide based catalyst. This material was obtained via an *in–situ* reduction of a mixture between $La(OH)_3$, NiO and La_2NiO_4 phases. The reduced catalyst was composed of polycrystalline Ni particles whose average size was 220nm dispersed 0.45% over the lanthanum oxide matrix. The influence of the dry reforming reactants and products partial pressure, as well as the temperature over the net CH_4, CO_2, CO, H_2 and H_2O rates, was assessed after planning and executing a series of central composite statistical experiments. Based on these results and on previous literature studies, seven kinetic models based on six Langmuir–Hinshelwood type reaction mechanisms were formulated and tested for describing the dry reforming reaction and the influence of the competing reverse water gas shift reaction over the catalytic behavior. Among the tested models, the one considering that the first C–H cleavage of CH_4 takes place over a metal−oxygen (*−O*) pair site described best statistically and thermodynamically the kinetic of the studied reaction system. The first C–H cleavage of the CH_4 molecule was also determined to be the rate–determining step of the reaction. A degree of rate control analysis of the model allowed establishing that the CO_2 dissociation step may act as an inhibitor of the dry reforming reaction when products are absent of the reaction environment. Such behavior caused an increase in the apparent activation energy of methane and it was explained by a saturation of the surface of nickel with chemisorbed O adatoms. The results of this study help explain why solid solution Ni–La oxide catalysts perform highly and stably during methane dry reforming. Also, they provide a robust kinetic basis for the design and scale–up of the process.

References

Abbas, S. Z., Dupont, V., & Mahmud, T. (2017). Kinetics study and modelling of steam methane reforming process over a NiO/Al 2 O 3 catalyst in an adiabatic packed bed reactor. *International Journal of Hydrogen Energy*, *42*(5), 2889–2903. https://doi.org/10.1016/j.ijhydene.2016.11.093

Anderson, J. (1963). A criterion for isothermal behaviour of a catalyst pellet. *Chemical Engineering Science*, *18*(2), 147–148. https://doi.org/https://doi.org/10.1016/0009-2509(63)80023-8

Argyle, M., & Bartholomew, C. (2015). Heterogeneous Catalyst Deactivation and Regeneration: A Review. *Catalysts*, *5*(1), 145–269. https://doi.org/10.3390/catal5010145

Asadzadeh, F., Maleki-Kaklar, M., Soiltanalinejad, N., & Shabani, F. (2018). Central Composite Design Optimization of Zinc Removal from Contaminated Soil, Using Citric Acid as Biodegradable Chelant. *Scientific Reports*, *8*(1), 2633. https://doi.org/10.1038/s41598-018-20942-9

Bai, Y., Kirvassilis, D., Xu, L., & Mavrikakis, M. (2019). Atomic and molecular adsorption on Ni(111). *Surface Science*, *679*(June 2018), 240–253. https://doi.org/10.1016/j.susc.2018.08.004

Baldovino-Medrano, V. G. Pérez-Martínez, D. J. (2003). *Reformado de metano con CO2 sobre catalizadores Ni/La2O3 obtenidos a partir de la perovskita LaNiO3*. Universidad Industrial de Santander.

Baldovino-Medrano, V. G., & Pérez-Martínez, D. de J. (2004). *Reformado de metano con CO2 sobre catalizadores Ni/La2O3 obtenidos a partir de la perovskita LaNiO3*. Universidad Industrial de Santander.

Bandrowski, J., Bickling, C. R., Yang, K. H., & Hougen, O. A. (1962). Kinetics of the reduction of nickel oxide by hydrogen. *Chemical Engineering Science*, *17*(5), 379–390. https://doi.org/10.1016/0009-2509(62)80039-6

Batiot-Dupeyrat, C., Sierra Gallego, G. A., Mondragon, F., Barrault, J., & Tatibouët, J.-M. (2005). CO2 reforming of methane over LaNiO3 as precursor material. *Catalysis Today*, *107–108*, 474–480. https://doi.org/10.1016/j.cattod.2005.07.014

Benguerba, Y., Dehimi, L., Virginie, M., Dumas, C., & Ernst, B. (2015). Modelling of methane dry reforming over Ni/Al2O3 catalyst in a fixed-bed catalytic reactor. *Reaction Kinetics, Mechanisms and Catalysis*, *114*(1), 109–119. https://doi.org/10.1007/s11144-014-0772-5

Bergeret, G., & Gallezot, P. (2008). Particle Size and Dispersion Measurements. In *Handbook of Heterogeneous Catalysis*. Wiley-VCH Verlag GmbH & Co. KGaA. https://doi.org/10.1002/9783527610044.hetcat0038

Betancourt, R. (2008). *Transferencia Molecular de Calor, Masa y/o Cantidad de Movimiento*. Universidad Nacional de Colombia.

Bhore, N. A., Klein, M. T., & Bischoff, K. B. (1990). The delplot technique: a new method for reaction pathway analysis. *Industrial & Engineering Chemistry Research*, *29*(2), 313–316. https://doi.org/10.1021/ie00098a025

Bird, R. B., Stewart, W. E., & Lightfoot, E. N. (2007). Transport Phenomena. In *J. Wiley*.

Blöchl, P. E. (1994). Projector augmented-wave method. *Physical Review B*, *50*(24), 17953–17979. https://doi.org/10.1103/PhysRevB.50.17953

Bobrova, L. N., Bobin, A. S., Mezentseva, N. V., Sadykov, V. A., Thybaut, J. W., & Marin, G. B. (2016). Kinetic assessment of dry reforming of methane on Pt + Ni containing composite of fluorite-like structure. *Applied Catalysis B: Environmental*, *182*, 513–524.

https://doi.org/10.1016/j.apcatb.2015.09.049

Boggs, P. T., Donaldson, J. R., Byrd, R. h., & Schnabel, R. B. (1989). Algorithm 676: ODRPACK: software for weighted orthogonal distance regression. *ACM Transactions on Mathematical Software (TOMS)*, *15*(4), 348–364. https://doi.org/10.1145/76909.76913

Bonmassar, N., Bekheet, M. F., Schlicker, L., Gili, A., Gurlo, A., Doran, A., Gao, Y., Heggen, M., Bernardi, J., Klötzer, B., & Penner, S. (2020). In Situ-Determined Catalytically Active State of LaNiO 3 in Methane Dry Reforming. *ACS Catalysis*, *10*(2), 1102–1112. https://doi.org/10.1021/acscatal.9b03687

Boudart, M., & Djega-Mariadassou, G. (1984). *Kinetics of Heterogeneous Catalytic Reactions*. Princeton University Press.

Bradford, M. C. J., & Vannice, M. A. (1996). Catalytic reforming of methane with carbon dioxide over nickel catalysts II. Reaction kinetics. *Applied Catalysis A: General*, *142*(1), 97–122. https://doi.org/10.1016/0926-860X(96)00066-X

Brunauer, S., Emmett, P. H., & Teller, E. (1938). Adsorption of Gases in Multimolecular Layers. *Journal of the American Chemical Society*, *60*(2), 309–319. https://doi.org/10.1021/ja01269a023

Caballero, K. V., Guerrero-Amaya, H., & Baldovino-Medrano, V. G. (2019). Revisiting glycerol esterification with acetic acid over Amberlyst-35 via statistically designed experiments: Overcoming transport limitations. *Chemical Engineering Science*, *207*, 91–104. https://doi.org/10.1016/j.ces.2019.06.003

Campbell, C. T. (2017). The Degree of Rate Control: A Powerful Tool for Catalysis Research. *ACS Catalysis*, *7*(4), 2770–2779. https://doi.org/10.1021/acscatal.7b00115

Campbell, C. T., Árnadóttir, L., & Sellers, J. R. V. (2013). Kinetic Prefactors of Reactions on Solid

Surfaces. *Zeitschrift Für Physikalische Chemie*, *227*(9–11), 1435–1454. https://doi.org/10.1524/zpch.2013.0395

Campbell, C. T., & Sellers, J. R. V. (2012). The Entropies of Adsorbed Molecules. *Journal of the American Chemical Society*, *134*(43), 18109–18115. https://doi.org/10.1021/ja3080117

Campbell, C. T., Sprowl, L. H., & Árnadóttir, L. (2016). Equilibrium Constants and Rate Constants for Adsorbates: Two-Dimensional (2D) Ideal Gas, 2D Ideal Lattice Gas, and Ideal Hindered Translator Models. *The Journal of Physical Chemistry C*, *120*(19), 10283–10297. https://doi.org/10.1021/acs.jpcc.6b00975

Carberry, J. J., & Wendel, M. M. (1963). A computer model of the fixed bed catalytic reactor: The adiabatic and quasi-adiabatic cases. *AIChE Journal*, *9*(1), 129–133. https://doi.org/10.1002/aic.690090128

Castillo-Araiza, C. O., Chávez, G., Dutta, A., de los Reyes, J. A., Nuñez, S., & García-Martínez, J. C. (2015). Role of Pt–Pd/γ-Al2O3 on the HDS of 4,6-DMBT: Kinetic modeling & contribution analysis. *Fuel Processing Technology*, *132*, 164–172. https://doi.org/10.1016/j.fuproc.2014.12.028

Çengel, Y. A., & Boles, M. A. (2015). *Thermodynamics: An Engineering Approach* (8th ed.). McGraw-Hill Education.

Challiwala, M. S., Ghouri, M. M., Linke, P., El-Halwagi, M. M., & Elbashir, N. O. (2017). A combined thermo-kinetic analysis of various methane reforming technologies: Comparison with dry reforming. *Journal of CO2 Utilization*, *17*, 99–111. https://doi.org/10.1016/j.jcou.2016.11.008

Charisiou, N. D., Siakavelas, G., Papageridis, K. N., Baklavaridis, A., Tzounis, L., Avraam, D. G., & Goula, M. A. (2016). Syngas production via the biogas dry reforming reaction over nickel

supported on modified with CeO2 and/or La2O3 alumina catalysts. *Journal of Natural Gas Science and Engineering*, *31*, 164–183. https://doi.org/10.1016/j.jngse.2016.02.021

Chin, Y.-H. (Cathy), Buda, C., Neurock, M., & Iglesia, E. (2013). Consequences of Metal–Oxide Interconversion for C–H Bond Activation during CH 4 Reactions on Pd Catalysts. *Journal of the American Chemical Society*, *135*(41), 15425–15442. https://doi.org/10.1021/ja405004m

Choisnet, J., Abadzhieva, N., Stefanov, P., Klissurski, D., Bassat, J. M., Rives, V., & Minchev, L. (1994). X-ray photoelectron spectroscopy, temperature-programmed desorption and temperature-programmed reduction study of LaNiO3 and La2NiO4 +? catalysts for methanol oxidation. *Journal of the Chemical Society, Faraday Transactions*, *90*(13), 1987. https://doi.org/10.1039/ft9949001987

Chorkendorff, I., & Niemantsverdriet, J. W. (2003). *Concepts of Modern Catalysis and Kinetics*. Wiley-VCH Verlag GmbH & Co. KGaA. https://doi.org/10.1002/3527602658

Chu, C. F., & Ng, K. M. (1989). Flow in packed tubes with a small tube to particle diameter ratio. *AIChE Journal*, *35*(1), 148–158. https://doi.org/10.1002/aic.690350116

Dahal, A., & Batzill, M. (2014). Graphene–nickel interfaces: a review. *Nanoscale*, *6*(5), 2548. https://doi.org/10.1039/c3nr05279f

de Carvalho, J. R. F. G., & Delgado, J. M. P. Q. (2003). Effect of fluid properties on dispersion in flow through packed beds. *AIChE Journal*, *49*(8), 1980–1985. https://doi.org/10.1002/aic.690490808

de Matos, L. M., Matos, R. M., & Giudici, R. (2010). Experimental and numerical investigation of dynamic heat transfer parameters in packed bed. *Heat and Mass Transfer*, *46*(11–12), 1355–136. https://doi.org/10.1007/s00231-010-0659-6

Dehimi, L., Benguerba, Y., Virginie, M., & Hijazi, H. (2017). Microkinetic modelling of methane

dry reforming over Ni/Al2O3 catalyst. *International Journal of Hydrogen Energy*, *42*(30), 18930–18940. https://doi.org/10.1016/j.ijhydene.2017.05.231

Delgado, J. M. P. Q. (2006). A critical review of dispersion in packed beds. *Heat and Mass Transfer*, *42*(4), 279–310. https://doi.org/10.1007/s00231-005-0019-0

Ding, X., De Rogatis, L., Vesselli, E., Baraldi, A., Comelli, G., Rosei, R., Savio, L., Vattuone, L., Rocca, M., Fornasiero, P., Ancilotto, F., Baldereschi, A., & Peressi, M. (2007). Interaction of carbon dioxide with Ni(110): A combined experimental and theoretical study. *Physical Review B*, *76*(19), 195425. https://doi.org/10.1103/PhysRevB.76.195425

Dorofeev, G. A., Streletskii, A. N., Povstugar, I. V, Protasov, A. V, & Elsukov, E. P. (2012). Determination of nanoparticle sizes by X-ray diffraction. *Colloid Journal*, *74*(6), 675–685. https://doi.org/10.1134/S1061933X12060051

Dumesic, J. A., Rudd, D. F., Aparicio, L. M., Rekoske, J. E., & Treviño, A. A. (1993). *The Microkinetics of Heterogeneous Catalysis*. American Chemical Society.

Dwivedi, P. N., & Upadhyay, S. N. (1977). Particle-Fluid Mass Transfer in Fixed and Fluidized Beds. *Industrial & Engineering Chemistry Process Design and Development*, *16*(2), 157–165. https://doi.org/10.1021/i260062a001

Eisfeld, B., & Schnitzlein, K. (2001). The influence of confining walls on the pressure drop in packed beds. *Chemical Engineering Science*, *56*(14), 4321–4329. https://doi.org/10.1016/S0009-2509(00)00533-9

Erley, W., Wagner, H., & Mach, H. (1979). Adsorption sites and long range order — vibrational spectra for CO on Ni(111). *Surface Science*, *80*, 612–619. https://doi.org/10.1016/0039-6028(79)90724-6

Fan, C., Zhu, Y.-A., Yang, M.-L., Sui, Z.-J., Zhou, X.-G., & Chen, D. (2015). Density Functional

Theory-Assisted Microkinetic Analysis of Methane Dry Reforming on Ni Catalyst. *Industrial & Engineering Chemistry Research*, *54*(22), 5901–5913. https://doi.org/10.1021/acs.iecr.5b00563

Faroldi, B. M., Múnera, J. F., & Cornaglia, L. M. (2014). In situ characterization of phase transformation and reactivity of high surface area lanthanum-based Ru catalysts for the combined reforming of methane. *Applied Catalysis B: Environmental*, *150–151*, 126–137. https://doi.org/10.1016/j.apcatb.2013.12.005

Fogler, S. H. (1999). *Elements of chemical reaction engineering* (3rd ed.). Pearson Education, Inc.

Fontaine, M.-L., Laberty-Robert, C., Ansart, F., & Tailhades, P. (2004). Elaboration and characterization of La2NiO4+δ powders and thin films via a modified sol–gel process. *Journal of Solid State Chemistry*, *177*(4–5), 1471–1479. https://doi.org/10.1016/j.jssc.2003.11.032

Foppa, L., Margossian, T., Kim, S. M., Müller, C., Copéret, C., Larmier, K., & Comas-Vives, A. (2017). Contrasting the Role of Ni/Al2O3 Interfaces in Water–Gas Shift and Dry Reforming of Methane. *Journal of the American Chemical Society*, *139*(47), 17128–17139. https://doi.org/10.1021/jacs.7b08984

Fornarini, L., Conde, J. C., Alvani, C., Olevano, D., & Chiussi, S. (2008). Experimental determination of La2O3 thermal conductivity and its application to the thermal analysis of a-Ge/La2O3/c-Si laser annealing. *Thin Solid Films*, *516*(21), 7400–7405. https://doi.org/10.1016/j.tsf.2008.02.032

Gallego, J., Sierra-Gallego, G., Tapia, J., Mondragón, F., & Batiot-Dupeyrat, C. (2016). Activation of CO2 on Ni/La2O3: non-isothermal kinetic study on the basis of thermogravimetric studies. *Reaction Kinetics, Mechanisms and Catalysis*, *119*(1), 179–193.

https://doi.org/10.1007/s11144-016-1032-7

Geankoplis, C. J. (1993). *Transport Processes and Unit Operations* (3rd ed.). Prentice-Hall, Inc.

Ghanbarian, B., Hunt, A. G., Ewing, R. P., & Sahimi, M. (2013). Tortuosity in Porous Media: A Critical Review. *Soil Science Society of America Journal*, *77*(5), 1461–1477. https://doi.org/10.2136/sssaj2012.0435

Gili, A., Schlicker, L., Bekheet, M. F., Görke, O., Kober, D., Simon, U., Littlewood, P., Schomäcker, R., Doran, A., Gaissmaier, D., Jacob, T., Selve, S., & Gurlo, A. (2019). Revealing the Mechanism of Multiwalled Carbon Nanotube Growth on Supported Nickel Nanoparticles by in Situ Synchrotron X-ray Diffraction, Density Functional Theory, and Molecular Dynamics Simulations. *ACS Catalysis*, *9*(8), 6999–7011. https://doi.org/10.1021/acscatal.9b00733

Gili, A., Schlicker, L., Bekheet, M. F., Görke, O., Penner, S., Grünbacher, M., Götsch, T., Littlewood, P., Marks, T. J., Stair, P. C., Schomäcker, R., Doran, A., Selve, S., Simon, U., & Gurlo, A. (2018). Surface Carbon as a Reactive Intermediate in Dry Reforming of Methane to Syngas on a 5% Ni/MnO Catalyst. *ACS Catalysis*, *8*(9), 8739–8750. https://doi.org/10.1021/acscatal.8b01820

Gonzalez-DelaCruz, V. M., Holgado, J. P., Pereñíguez, R., & Caballero, A. (2008). Morphology changes induced by strong metal-support interaction on a Ni-ceria catalytic system. *Journal of Catalysis*, *257*(2), 307–314. https://doi.org/10.1016/j.jcat.2008.05.009

Haibel, E., Berendts, S., & Walter, D. (2018). Thermogravimetric and X-ray diffraction investigation on carbonated lanthanum oxide and lanthanum hydroxide formed in humid CO2 atmosphere. *Journal of Thermal Analysis and Calorimetry*, *134*(1), 261–267. https://doi.org/10.1007/s10973-018-7256-1

Han, J. W., Park, J. S., Choi, M. S., & Lee, H. (2017). Uncoupling the size and support effects of Ni catalysts for dry reforming of methane. *Applied Catalysis B: Environmental*, *203*, 625–632. https://doi.org/10.1016/j.apcatb.2016.10.069

Han, Z., Yang, Z., & Han, M. (2019). Comprehensive investigation of methane conversion over Ni(111) surface under a consistent DFT framework: Implications for anti-coking of SOFC anodes. *Applied Surface Science*, *480*(February), 243–255. https://doi.org/10.1016/j.apsusc.2019.02.084

Harris, J. W., Verma, A. A., Arvay, J. W., Shih, A. J., Delgass, W. N., & Ribeiro, F. H. (2020). Consequences of product inhibition in the quantification of kinetic parameters. *Journal of Catalysis*, *389*, 468–475. https://doi.org/10.1016/j.jcat.2020.06.014

Haynes, W. M. (2014). *CRC Handbook of Chemistry and Physics* (95th ed.). CRC Press.

Herrera, K., Maier, L., Tischer, S., Zellner, A., Stotz, H., & Deutschmann, O. (2015). Surface Reaction Kinetics of Steam- and CO2-Reforming as Well as Oxidation of Methane over Nickel-Based Catalysts. *Catalysts*, *5*(2), 871–904. https://doi.org/10.3390/catal5020871

Huízar-Félix, A. M., Hernández, T., de la Parra, S., Ibarra, J., & Kharisov, B. (2012). Sol–gel based Pechini method synthesis and characterization of Sm1−xCaxFeO3 perovskite 0.1≤x≤0.5. *Powder Technology*, *229*, 290–293. https://doi.org/10.1016/j.powtec.2012.06.057

Ino, E., Shimizu, K., & Yamate, T. (1976). Studies on Thermal Decomposition Process of Lanthanum Hydroxide. *Journal of the Society of Materials Science, Japan*, *25*(279), 1165–1168. https://doi.org/10.2472/jsms.25.1165

Jafarbegloo, M., Tarlani, A., Mesbah, A. W., & Sahebdelfar, S. (2015). Thermodynamic analysis of carbon dioxide reforming of methane and its practical relevance. *International Journal of Hydrogen Energy*, *40*(6), 2445–2451. https://doi.org/10.1016/j.ijhydene.2014.12.103

Jørgensen, M., & Grönbeck, H. (2017). Connection between macroscopic kinetic measurables and the degree of rate control. *Catalysis Science & Technology*, *7*(18), 4034–4040. https://doi.org/10.1039/C7CY01246B

Kass, R. E., & Raftery, A. E. (1995). Bayes Factors. *Journal of the American Statistical Association*, *90*(430), 773. https://doi.org/10.2307/2291091

Kathiraser, Y., Oemar, U., Saw, E. T., Li, Z., & Kawi, S. (2015). Kinetic and mechanistic aspects for CO2 reforming of methane over Ni based catalysts. *Chemical Engineering Journal*, *278*, 62–78. https://doi.org/10.1016/j.cej.2014.11.143

Kim, J.-W., Ha, J.-A., Jung, H., Ahn, B.-I., Lee, S.-H., & Choi, J.-G. (2007). Kinetic analysis of supported Ni-catalyzed CO2/CH4 reactions using photoacoustic spectroscopy. *Physical Chemistry Chemical Physics*, *9*(43), 5828. https://doi.org/10.1039/b709102h

Kresse, G., & Furthmüller, J. (1996). Efficient iterative schemes for ab initio total-energy calculations using a plane-wave basis set. *Physical Review B*, *54*(16), 11169–11186. https://doi.org/10.1103/PhysRevB.54.11169

Li, Kai, He, F., Yu, H., Wang, Y., & Wu, Z. (2018). Theoretical study on the reaction mechanism of carbon dioxide reforming of methane on La and La2O3 modified Ni(111) surface. *Journal of Catalysis*, *364*, 248–261. https://doi.org/10.1016/j.jcat.2018.05.026

Li, Kang, Chang, X., Pei, C., Li, X., Chen, S., Zhang, X., Assabumrungrat, S., Zhao, Z.-J., Zeng, L., & Gong, J. (2019). Ordered mesoporous Ni/La2O3 catalysts with interfacial synergism towards CO2 activation in dry reforming of methane. *Applied Catalysis B: Environmental*, *259*(May), 118092. https://doi.org/10.1016/j.apcatb.2019.118092

Li, S., Tang, H., Gong, D., Ma, Z., & Liu, Y. (2017). Loading Ni/La2O3 on SiO2 for CO methanation from syngas. *Catalysis Today*, *297*(March), 298–307.

https://doi.org/10.1016/j.cattod.2017.06.014

Manoilova, O. V., Podkolzin, S. G., Tope, B., Lercher, J., Stangland, E. E., Goupil, J.-M., & Weckhuysen, B. M. (2004). Surface Acidity and Basicity of La2O3 , LaOCl, and LaCl3 Characterized by IR Spectroscopy, TPD, and DFT Calculations. *The Journal of Physical Chemistry B*, *108*(40), 15770–15781. https://doi.org/10.1021/jp040311m

Manukyan, K. V., Avetisyan, A. G., Shuck, C. E., Chatilyan, H. A., Rouvimov, S., Kharatyan, S. L., & Mukasyan, A. S. (2015). Nickel Oxide Reduction by Hydrogen: Kinetics and Structural Transformations. *The Journal of Physical Chemistry C*, *119*(28), 16131–16138. https://doi.org/10.1021/acs.jpcc.5b04313

Mao, Z., & Campbell, C. T. (2019). Apparent Activation Energies in Complex Reaction Mechanisms: A Simple Relationship via Degrees of Rate Control. *ACS Catalysis*, *9*(10), 9465–9473. https://doi.org/10.1021/acscatal.9b02761

Marquardt, D. W. (1963). An Algorithm for Least-Squares Estimation of Nonlinear Parameters. *Journal of the Society for Industrial and Applied Mathematics*, *11*(2), 431–441. https://doi.org/10.1137/0111030

Massalmi, H. A., & Maymó, J. A. (1969). Error in handling finite conversion reactor data by the differential method. *Journal of Catalysis*, *14*(1), 61–68. https://doi.org/10.1016/0021-9517(69)90356-X

McCabe, W. L., Smith, J. C., & Harriott, P. (2005). Unit Operations of Chemical Engineering. In *McGraw-Hill*.

McQuarrie, D. A. (1973). *Statistical Mechanics*. Harper & Row.

Mears, D. E. (1971a). Diagnostic criteria for heat transport limitations in fixed bed reactors. *Journal of Catalysis*, *20*(2), 127–131. https://doi.org/10.1016/0021-9517(71)90073-X

Mears, D. E. (1971b). Tests for Transport Limitations in Experimental Catalytic Reactors. *Industrial & Engineering Chemistry Process Design and Development*, *10*(4), 541–547. https://doi.org/10.1021/i260040a020

Messaoudi, H., Thomas, S., Djaidja, A., Slyemi, S., & Barama, A. (2018). Study of LaxNiO y and LaxNiO/MgAl2O4 catalysts in dry reforming of methane. *Journal of CO2 Utilization*, *24*(December 2017), 40–49. https://doi.org/10.1016/j.jcou.2017.12.002

Methfessel, M., & Paxton, A. T. (1989). High-precision sampling for Brillouin-zone integration in metals. *Physical Review B*, *40*(6), 3616–3621. https://doi.org/10.1103/PhysRevB.40.3616

Minette, F., Lugo-Pimentel, M., Modroukas, D., Davis, A. W., Gill, R., Castaldi, M. J., & De Wilde, J. (2018). Intrinsic kinetics of steam methane reforming on a thin, nanostructured and adherent Ni coating. *Applied Catalysis B: Environmental*, *238*(April), 184–197. https://doi.org/10.1016/j.apcatb.2018.07.015

Monkhorst, H. J., & Pack, J. D. (1976). Special points for Brillouin-zone integrations. *Physical Review B*, *13*(12), 5188–5192. https://doi.org/10.1103/PhysRevB.13.5188

Montgomery, D. C. (2012). *Design and Analysis of Experiments* (8th ed.). John Wiley & Sons, Inc.

Moradi, G. R., Rahmanzadeh, M., & Sharifnia, S. (2010). Kinetic investigation of CO2 reforming of CH4 over La–Ni based perovskite. *Chemical Engineering Journal*, *162*(2), 787–791. https://doi.org/10.1016/j.cej.2010.06.006

Múnera, J. F., Irusta, S., Cornaglia, L. M., Lombardo, E. A., Vargas Cesar, D., & Schmal, M. (2007). Kinetics and reaction pathway of the CO2reforming of methane on Rh supported on lanthanum-based solid. *Journal of Catalysis*, *245*(1), 25–34. https://doi.org/10.1016/j.jcat.2006.09.008

Murakhtina, T., Delle Site, L., & Sebastiani, D. (2006). Vibrational Frequencies of Water Adsorbed on (111) and (221) Nickel Surfaces from First Principle Calculations. *ChemPhysChem*, *7*(6), 1215–1219. https://doi.org/10.1002/cphc.200500642

NIST. (2013). *NIST/SEMATECH e-Handbook of Statistical Methods*. https://doi.org/https://doi.org/10.18434/M32189

Osazuwa, O. U., Setiabudi, H. D., Abdullah, S., & Cheng, C. K. (2017). Syngas production from methane dry reforming over SmCoO 3 perovskite catalyst: Kinetics and mechanistic studies. *International Journal of Hydrogen Energy*, *42*(15), 9707–9721. https://doi.org/10.1016/j.ijhydene.2017.03.061

Otyuskaya, D., Thybaut, J. W., Alexiadis, V., Alekseeva, M., Venderbosch, R., Yakovlev, V., & Marin, G. B. (2018). Fast pyrolysis oil stabilization kinetics over a Ni-Cu catalyst using propionic acid as a model compound. *Applied Catalysis B: Environmental*, *233*(March), 46–57. https://doi.org/10.1016/j.apcatb.2018.03.062

Papadopoulou, C., Matralis, H., & Verykios, X. (2012). Utilization of Biogas as a Renewable Carbon Source: Dry Reforming of Methane. In L. Guczi & A. Erdôhelyi (Eds.), *Catalysis for Alternative Energy Generation* (pp. 57–127). Springer New York. https://doi.org/10.1007/978-1-4614-0344-9_3

Perdew, J. P., & Wang, Y. (1992). Accurate and simple analytic representation of the electron-gas correlation energy. *Physical Review B*, *45*(23), 13244–13249. https://doi.org/10.1103/PhysRevB.45.13244

Pereñiguez, R., Gonzalez-delaCruz, V. M., Caballero, A., & Holgado, J. P. (2012). LaNiO3 as a precursor of Ni/La2O3 for CO2 reforming of CH4: Effect of the presence of an amorphous NiO phase. *Applied Catalysis B: Environmental*, *123–124*, 324–332.

https://doi.org/10.1016/j.apcatb.2012.04.044

Pichas, C., Pomonis, P., Petrakis, D., & Ladavos, A. (2010). Kinetic study of the catalytic dry reforming of CH4 with CO2 over La2−xSrxNiO4 perovskite-type oxides. *Applied Catalysis A: General*, *386*(1–2), 116–123. https://doi.org/10.1016/j.apcata.2010.07.043

Powell, R. W., Tye, R. P., & Hickman, M. J. (1965). The thermal conductivity of nickel. *International Journal of Heat and Mass Transfer*, *8*(5), 679–688. https://doi.org/10.1016/0017-9310(65)90017-7

Rajkhowa, T., Marin, G. B., & Thybaut, J. W. (2017). A comprehensive kinetic model for Cu catalyzed liquid phase glycerol hydrogenolysis. *Applied Catalysis B: Environmental*, *205*, 469–480. https://doi.org/10.1016/j.apcatb.2016.12.042

Rivas, I., Alvarez, J., Pietri, E., Pérez-Zurita, M. J., & Goldwasser, M. R. (2010). Perovskite-type oxides in methane dry reforming: Effect of their incorporation into a mesoporous SBA-15 silica-host. *Catalysis Today*, *149*(3–4), 388–393. https://doi.org/10.1016/j.cattod.2009.05.028

Ro, I., Resasco, J., & Christopher, P. (2018). Approaches for Understanding and Controlling Interfacial Effects in Oxide-Supported Metal Catalysts. *ACS Catalysis*, *8*(8), 7368–7387. https://doi.org/10.1021/acscatal.8b02071

Rosenbrock, H. H. (1960). An Automatic Method for Finding the Greatest or Least Value of a Function. *The Computer Journal*, *3*(3), 175–184. https://doi.org/10.1093/comjnl/3.3.175

Rouquerol, J., Llewellyn, P., & Rouquerol, F. (2007). Is the bet equation applicable to microporous adsorbents? In *Studies in Surface Science and Catalysis* (Vol. 160, pp. 49–56). Elsevier B.V. https://doi.org/10.1016/S0167-2991(07)80008-5

Sandoval-Bohorquez, V. S., Rozo, E. A. V., & Baldovino-Medrano, V. G. (2020). A method for

the highly accurate quantification of gas streams by on-line chromatography. *Journal of Chromatography A*, *1626*, 461355. https://doi.org/10.1016/j.chroma.2020.461355

Sandoval Bohórquez, V. S., Peña Prada, J. A., Pérez-Martínez, D. de J., & Baldovino-Medrano, V. G. (2017). Reformado de metano con CO2 sobre catalizadores Ni/La2O3 obtenidos a partir de la perovskita LaNiO3. *Memorias Del X Simposio Colombiano de Catálisis*. https://doi.org/ISSN: 2619-6042

Santacesaria, E. (1997). Kinetics and transport phenomena. *Catalysis Today*, *34*(3–4), 393–400. https://doi.org/10.1016/S0920-5861(96)00061-2

Sergeev, O. A., Shashkov, A. G., & Umanskii, A. S. (1982). Thermophysical properties of quartz glass. *Journal of Engineering Physics*, *43*(6), 1375–1383. https://doi.org/10.1007/BF00824797

Sierra-Gallego, G., Batiot-Dupeyrat, C., Barrault, J., & Mondragón, F. (2008). Dual Active-Site Mechanism for Dry Methane Reforming over Ni/La2O3 Produced from LaNiO3 Perovskite. *Industrial & Engineering Chemistry Research*, *47*(23), 9272–9278. https://doi.org/10.1021/ie800281t

Sierra Gallego, G., Mondragón, F., Barrault, J., Tatibouët, J.-M., & Batiot-Dupeyrat, C. (2006). CO2 reforming of CH4 over La–Ni based perovskite precursors. *Applied Catalysis A: General*, *311*, 164–171. https://doi.org/10.1016/j.apcata.2006.06.024

Sierra Gallego, G., Mondragón, F., Tatibouët, J.-M., Barrault, J., & Batiot-Dupeyrat, C. (2008). Carbon dioxide reforming of methane over La2NiO4 as catalyst precursor—Characterization of carbon deposition. *Catalysis Today*, *133–135*(1–4), 200–209. https://doi.org/10.1016/j.cattod.2007.12.075

Singh, S., Prestat, E., Huang, L.-F., Rondinelli, J. M., Haigh, S. J., & Rosen, B. A. (2017). Role of

2D and 3D defects on the reduction of LaNiO3 nanoparticles for catalysis. *Scientific Reports*, *7*(1), 10080. https://doi.org/10.1038/s41598-017-10703-5

Singh, S., Zubenko, D., & Rosen, B. A. (2016). Influence of LaNiO3 Shape on Its Solid-Phase Crystallization into Coke-Free Reforming Catalysts. *ACS Catalysis*, *6*(7), 4199–4205. https://doi.org/10.1021/acscatal.6b00673

Slagtern, A., Schuurman, Y., Leclercq, C., Verykios, X., & Mirodatos, C. (1997). Specific Features Concerning the Mechanism of Methane Reforming by Carbon Dioxide over Ni/La2O3Catalyst. *Journal of Catalysis*, *172*(1), 118–126. https://doi.org/10.1006/jcat.1997.1823

Sprowl, L. H., Campbell, C. T., & Árnadóttir, L. (2016). Hindered Translator and Hindered Rotor Models for Adsorbates: Partition Functions and Entropies. *The Journal of Physical Chemistry C*, *120*(18), 9719–9731. https://doi.org/10.1021/acs.jpcc.5b11616

Sunde, T. O. L., Grande, T., & Einarsrud, M.-A. (2016). Modified Pechini Synthesis of Oxide Powders and Thin Films. In *Handbook of Sol-Gel Science and Technology* (pp. 1–30). Springer International Publishing. https://doi.org/10.1007/978-3-319-19454-7_130-1

Szekely, J., Lin, C. I., & Sohn, H. Y. (1973). A structural model for gas—solid reactions with a moving boundary—V an experimental study of the reduction of porous nickel-oxide pellets with hydrogen. *Chemical Engineering Science*, *28*(11), 1975–1989. https://doi.org/10.1016/0009-2509(73)85042-0

Thommes, M., Kaneko, K., Neimark, A. V., Olivier, J. P., Rodriguez-Reinoso, F., Rouquerol, J., & Sing, K. S. W. (2015). Physisorption of gases, with special reference to the evaluation of surface area and pore size distribution (IUPAC Technical Report). *Pure and Applied Chemistry*, *87*(9–10), 1051–1069. https://doi.org/10.1515/pac-2014-1117

Toch, K., Thybaut, J. W., & Marin, G. B. (2015). A systematic methodology for kinetic modeling of chemical reactions applied to n -hexane hydroisomerization. *AIChE Journal*, *61*(3), 880–892. https://doi.org/10.1002/aic.14680

Tsipouriari, V., & Verykios, X. (1999). Carbon and Oxygen Reaction Pathways of CO2 Reforming of Methane over Ni/La2O3 and Ni/Al2O3 Catalysts Studied by Isotopic Tracing Techniques. *Journal of Catalysis*, *94*, 85–94.

Tsipouriari, V., & Verykios, X. (2001). Kinetic study of the catalytic reforming of methane with carbon dioxide to synthesis gas over Ni/La2O3 catalyst. *Catalysis Today*, *64*(1–2), 83–90. https://doi.org/10.1016/S0920-5861(00)00511-3

Tsyganenko, A. A., Lamotte, J., Gallas, J. P., & Lavalley, J. C. (1989). Infrared study of low-temperature carbon monoxide adsorption on lanthanum sesquioxide. *The Journal of Physical Chemistry*, *93*(10), 4179–4183. https://doi.org/10.1021/j100347a057

Tu, W., Ghoussoub, M., Singh, C. V., & Chin, Y.-H. C. (2017). Consequences of Surface Oxophilicity of Ni, Ni-Co, and Co Clusters on Methane Activation. *Journal of the American Chemical Society*, *139*(20), 6928–6945. https://doi.org/10.1021/jacs.7b01632

Usman, M., Wan Daud, W. M. A., & Abbas, H. F. (2015). Dry reforming of methane: Influence of process parameters—A review. *Renewable and Sustainable Energy Reviews*, *45*, 710–744. https://doi.org/10.1016/j.rser.2015.02.026

Vannice, M. A. (2005). *Kinetics of Catalytic Reactions*. Springer Science+Business Media, Inc.

Vannice, M. A., Hyun, S., Kalpakci, B., & Liauh, W. (1979). Entropies of adsorption in heterogeneous catalytic reactions. *Journal of Catalysis*, *56*(3), 358–362. https://doi.org/10.1016/0021-9517(79)90128-3

Vargas, M. A., Diosa, J. E., & Mosquera, E. (2020). The structural, optical and magnetic property

of iron oxides submicron particles synthesized by the Pechini method from steel industry wastes. *Journal of Magnetism and Magnetic Materials*, *513*, 167243. https://doi.org/10.1016/j.jmmm.2020.167243

Verykios, X. (2003). Catalytic dry reforming of natural gas for the production of chemicals and hydrogen. *International Journal of Hydrogen Energy*, *28*(10), 1045–1063. https://doi.org/10.1016/S0360-3199(02)00215-X

Wang, J., Carson, J. K., North, M. F., & Cleland, D. J. (2006). A new approach to modelling the effective thermal conductivity of heterogeneous materials. *International Journal of Heat and Mass Transfer*, *49*(17–18), 3075–3083. https://doi.org/10.1016/j.ijheatmasstransfer.2006.02.007

Wang, S.-G., Liao, X.-Y., Hu, J., Cao, D.-B., Li, Y.-W., Wang, J., & Jiao, H. (2007). Kinetic aspect of CO2 reforming of CH4 on Ni(111): A density functional theory calculation. *Surface Science*, *601*(5), 1271–1284. https://doi.org/10.1016/j.susc.2006.12.059

Wang, S., Cong, L., Zhao, C., Li, Y., Pang, Y., Zhao, Y., Li, S., & Sun, Y. (2017). First principles studies of CO2 and O2 chemisorption on La2O3 surfaces. *Phys. Chem. Chem. Phys.*, *19*(39), 26799–26811. https://doi.org/10.1039/C7CP05471H

Wei, J., & Iglesia, E. (2004a). Mechanism and Site Requirements for Activation and Chemical Conversion of Methane on Supported Pt Clusters and Turnover Rate Comparisons among Noble Metals. *The Journal of Physical Chemistry B*, *108*(13), 4094–4103. https://doi.org/10.1021/jp036985z

Wei, J., & Iglesia, E. (2004b). Isotopic and kinetic assessment of the mechanism of reactions of CH4 with CO2 or H2O to form synthesis gas and carbon on nickel catalysts. *Journal of Catalysis*, *224*(2), 370–383. https://doi.org/10.1016/j.jcat.2004.02.032

Weisz, P. B., & Prater, C. D. (1954). Interpretation of Measurements in Experimental Catalysis. *Advances in Catalysis*, *6*, 143–196. https://doi.org/10.1016/S0360-0564(08)60390-9

Wojdyr, M. (2010). Fityk : a general-purpose peak fitting program. *Journal of Applied Crystallography*, *43*(5), 1126–1128. https://doi.org/10.1107/S0021889810030499

Wu, P., Tao, Y., Ling, H., Chen, Z., Ding, J., Zeng, X., Liao, X., Stampfl, C., & Huang, J. (2019). Cooperation of Ni and CaO at Interface for CO 2 Reforming of CH 4 : A Combined Theoretical and Experimental Study. *ACS Catalysis*, *9*(11), 10060–10069. https://doi.org/10.1021/acscatal.9b02286

Xie, Z., Liao, Q., Liu, M., Yang, Z., & Zhang, L. (2017). Micro-kinetic modeling study of dry reforming of methane over the Ni-based catalyst. *Energy Conversion and Management*, *153*(August), 526–537. https://doi.org/10.1016/j.enconman.2017.10.022

Young, L. C., & Finlayson, B. A. (1973). Axial Dispersion in Nonisothermal Packed Bed Chemical Reactors. *Industrial & Engineering Chemistry Fundamentals*, *12*(4), 412–422. https://doi.org/10.1021/i160048a004

Yuan, K., Zhong, J.-Q., Zhou, X., Xu, L., Bergman, S. L., Wu, K., Xu, G. Q., Bernasek, S. L., Li, H. X., & Chen, W. (2016). Dynamic Oxygen on Surface: Catalytic Intermediate and Coking Barrier in the Modeled CO 2 Reforming of CH 4 on Ni (111). *ACS Catalysis*, *6*(7), 4330–4339. https://doi.org/10.1021/acscatal.6b00357

Zhang, G., Liu, J., Xu, Y., & Sun, Y. (2018). A review of CH4–CO2 reforming to synthesis gas over Ni-based catalysts in recent years (2010–2017). *International Journal of Hydrogen Energy*, *43*(32), 15030–15054. https://doi.org/10.1016/j.ijhydene.2018.06.091

Zhang, J., Wang, H., & Dalai, A. K. (2009). Kinetic Studies of Carbon Dioxide Reforming of Methane over Ni−Co/Al−Mg−O Bimetallic Catalyst. *Industrial & Engineering Chemistry*

Research, *48*(2), 677–684. https://doi.org/10.1021/ie801078p

Zhang, T., Liu, Z., Zhu, Y.-A., Liu, Z., Sui, Z., Zhu, K., & Zhou, X. (2020). Dry reforming of methane on Ni-Fe-MgO catalysts: Influence of Fe on carbon-resistant property and kinetics. *Applied Catalysis B: Environmental*, *264*(February 2019), 118497. https://doi.org/10.1016/j.apcatb.2019.118497

Zhang, Z., & Verykios, X. (1996). Carbon dioxide reforming of methane to synthesis gas over Ni/La2O3 catalysts. *Applied Catalysis A: General*, *138*(1), 109–133. https://doi.org/10.1016/0926-860X(95)00238-3

Zhang, Z., & Verykios, X. E. (1995). A stable and active nickel-based catalyst for carbon dioxide reforming of methane to synthesis gas. *Journal of the Chemical Society, Chemical Communications*, *1*, 71. https://doi.org/10.1039/c39950000071

Zhu, Y. A., Chen, D., Zhou, X. G., & Yuan, W. K. (2009). DFT studies of dry reforming of methane on Ni catalyst. *Catalysis Today*, *148*(3–4), 260–267. https://doi.org/10.1016/j.cattod.2009.08.022

Zuo, Z., Liu, S., Wang, Z., Liu, C., Huang, W., Huang, J., & Liu, P. (2018). Dry Reforming of Methane on Single-Site Ni/MgO Catalysts: Importance of Site Confinement [Research-article]. *ACS Catalysis*, *8*(10), 9821–9835. https://doi.org/10.1021/acscatal.8b02277

Supplementary Information

Section A. Experimental Methods

Synthesis of the catalyst. A Ni–La_2O_3 based catalyst was prepared via the decomposition of a perovskite type precursors synthesized by the citrate complexing method.(S. Li et al., 2017) For the method, adequate amounts of nickel (Merck, 99.9%) and lanthanum (ITW, 99.9%) nitrates were dissolved in deionized water with continuous stirring at 303K. Afterward, citric acid (Merck, 99.9%) and ethylene glycol (Sigma, 99%) were added to the solution of the nitrates. The molar ratio of the components of the solution was: Ni(1)/La(1)/citric acid(2.5)/ethylene glycol(1)/deionized water(220). The solution was aged at 343K until gelation. The gel was left to dry overnight keeping the temperature at 373K and then it was calcined in static oven at 773K for 2h using a heating rate of 0.083K.s^{-1}.

Assessment of physicochemical properties. The textural properties of the catalyst after its synthesis and after its reduction with H_2 at 1023K were evaluated from data produced after measuring the sorption of N_2 (Linde, Grade 5.0) at 77K in a high vacuum 3FLEXTM instrument (Micromeritics). Before the analysis, samples of ~0.5g were degassed first at 393K for 2h and then at 673K overnight under vacuum of 1Pa. The specific surface area of the material was estimated with the Brunauer–Emmett–Teller (BET) method and following the CBET optimization routine proposed by Rouquerol.(Brunauer et al., 1938; Rouquerol et al., 2007)

The number of surface exposed nickel atoms (M_{Ni}), further assumed to be equal to the number of active sites with a stoichiometry of 1/1 for H/Ni, was estimated from static volumetric H_2 chemisorption measurements done at 308K on the same 3FLEX^{TM} instrument mentioned before. For the measurements, a sample of ~0.5g catalyst was placed in a quartz fixed bed U–tube reactor (0.7cm ID). The sample was first degassed at 383K for 3h under vacuum of 100mPa and

then treated with a flow of H_2 (Linde, Grade 5.0, space velocity = 0.7$cm^3.g^{-1}.s^{-1}$) at 1023K for 2h, heating rate = 0.083$K.s^{-1}$. Afterwards, the sample was allowed to cool down to 308K for the analysis under vacuum of 1mPa. Two H_2 uptake isotherms were recorded consecutively from 0.1 to 10kPa, and between these measurements, the sample was evacuated under vacuum of 1mPa at 308K for 0.25h. The irreversible H_2 uptake was calculated by extrapolating the difference between these two isotherms to zero pressure. From these results, the mean Ni particle size ($\langle d_{chem} \rangle$) was estimated according to **eq S1**:

$$\langle d_{chem} \rangle = \frac{C}{D_{Ni}} \quad \text{(S1)}$$

Where, D_{Ni} is the dispersion of nickel and C is a shape factor equal to 1.01 considering spherical particles with equal surface proportion of the index planes Ni(111), Ni(110) and Ni(100).(Bergeret & Gallezot, 2008)

The hydrogen temperature–programmed of reduction (TPR) profile of the catalyst, sample weight of ~0.2g, was recorded between 400K and 1100K, heating rate = 0.083$K.s^{-1}$, under a flow of a 10vol% mixture of H_2/argon (Linde, Grade 5.0, space velocity = 4.2$cm^3.g^{-1}.s^{-1}$) using a CATLAB instrument (Hiden Analytical) equipped with a quartz fixed bed reactor (0.7cm ID) and coupled to a QGA mass spectrometer (Hiden Analytical) calibrated with gas pulses of 15µL. The sample was flushed with argon (Linde, Grade 5.0, space velocity = 4.2$cm^3.g^{-1}.s^{-1}$) at 393K for 1h and then at 673K for another 3h before recording the TPR profile. The deconvolution of the reduction peaks was made with Fityk® software using the Gaussian function.(Wojdyr, 2010) The peak areas obtained from this analysis were used together with the calibration pulses to determine the H_2 uptakes.

The crystallinity of the catalyst was assessed by recording X–ray diffraction patterns (XRD) of samples after its synthesis and after its reduction with H_2 at 1023K. XRD patterns were recorded with a D8–Advance (Bruker) diffractometer provided with a Lineal LynxEye detector and using CuKα radiation (40kV, 40mA). The diffraction patterns were obtained over 10–70° 2θ range at a scan rate of $2°.min^{-1}$ and with a step size of 0.02°. The identification and semi–quantitative analysis of the observed crystalline phases were performed with Match!® software (Crystal Impact). The mean crystallite sizes ($\langle d_{xrd} \rangle$) were estimated using the Scherrer equation:

$$\langle d_{xrd} \rangle = \frac{K\lambda}{B \cos\theta} \quad \text{(S2)}$$

Where, λ is the radiation wavelength (0.1542nm for CuKα radiation), 2θ, in radians, is the scattering angle selected for estimating the average crystallite size, B the integral broadening of the diffraction peak at 2θ in radians, and K a constant of ~1.07 for spherical–shaped particles.(Vannice, 2005)

Experimental set–up. The catalytic tests were carried out in a quartz fixed bed reactor (1.1cm ID) packed with 180–300mm fresh catalyst mixed with quartz (Merck, 99.9%) to avoid axial or radial temperature gradients. The explored operational conditions were 838–1008K, 130kPa total pressure, space velocity equal to $2220 cm^3.g^{-1}.s^{-1}$ and several concentrations of CH_4, CO_2, CO (all Cryogas, Grade 4.0), H_2 and N_2 (both Linde, Grade 5.0). A simplified flowsheet of the experimental set–up is depicted in **Figure S1**. All gases were fed to the reactor via mass flow controllers (Alicat) with an accuracy of ±0.1% of full scale. The operating pressure was set at the reactor outlet using a back–pressure regulator (Alicat) with an accuracy of ±0.3% of full scale. The temperature of the system was monitored in the catalytic bed and close to the external wall of the reactor with K thermocouples enclosed within stainless–steel 316 sheets (1/8in OD) and established to the desired value using a programmable logic controller (Rockwell) with an

accuracy of ± 1K. The difference between the recorded temperatures in the bed and the external wall of the reactor was kept lower than 5K.

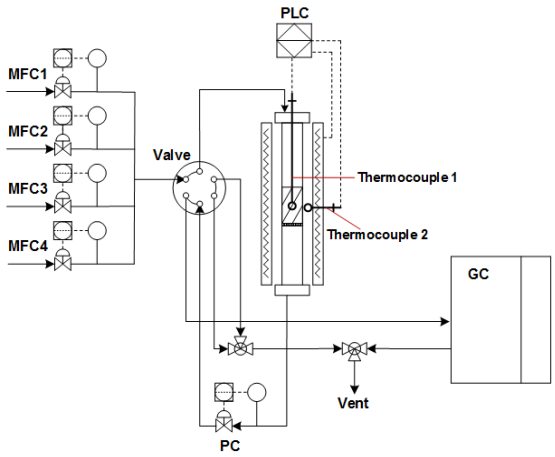

Figure S1. Schematic overview of the experimental setup (MFC, PC, and PLC indicate mass flow, pressure, and programmable logic controllers, respectively).

For the tests, the samples of the fresh catalyst of 3mg, were treated with a 10vol% flow of H_2/N_2 (space velocity = 280 $cm^3.g^{-1}.s^{-1}$) at 1023K for 2h, heating rate = 0.083$K.s^{-1}$. Then, the reactor was flushed with N_2 until no detectable amounts of H_2 in the outlet stream of the reactor. Afterward, the reactor was allowed to cool down to the selected reaction temperature and then fed with the selected reaction mixture.

The analysis of the reactor effluent was made on–line with a GC–2014 chromatograph (Shimadzu) equipped with 80/100 Hayesep Q (300cm) and 60/80 Mol–Sieve 5A (300cm) packed columns, and a thermal conductivity detector (TCD) coupled to a methanizer and to a flame ionization detector (FID). The methanizer consists of a Ni catalyst bed that transforms CO and CO_2 into CH_4 ($CO_x + (2+x)H_2 \rightarrow CH_4 + xH_2O$) at 648K for their indirect detection in the FID. For the analysis, the temperature of the columns of the instrument was kept at 373K using argon (Linde, Grade 5.0) as the carrier gas (20$cm^3.min^{-1}$). Meanwhile, the TCD and FID detectors were

operated at 433K and 473K, respectively. The concentrations of H_2 and N_2 (i–th species, **eq S3**) were quantified with the data from the TCD, while CH_4, CO_2, CO (j–th species, **eq S4**) were quantified with the data from the FID. The following equations were used for quantification:

$$\mathrm{F_i} = b_\mathrm{i} * \frac{\mathrm{A_{i,TCD}}}{\mathrm{A_{N_2,TCD}}} * \mathrm{F^0_{N_2}} \tag{S3}$$

$$\mathrm{F_j} = \frac{b_\mathrm{j}}{a_\mathrm{j}} * \frac{\mathrm{A_{j,FID}}}{\mathrm{A_{N_2,TCD}}} * \mathrm{F^0_{N_2}} \tag{S4}$$

Where, $\mathrm{F_{i\,or\,j}}$ is the estimated molar flow; $\mathrm{F^0_{N_2}}$ is the inlet N_2 molar flow; $\mathrm{A_{i\,or\,j}}$ is the chromatographic peak area of the corresponding analyte either in the TCD or FID; $b_{\mathrm{i\,or\,j}}$ is the response factor for each analyte; and, a_j is a proportionality factor between the FID and TCD peak areas of j–th species (i.e. $\mathrm{A_{j,FID}} = a_\mathrm{j}\,\mathrm{A_{j,TCD}}$). Full details of the method implemented for gas quantification are discussed elsewhere.(Sandoval-Bohorquez et al., 2020)

Expression of the results. Reaction rates were estimated at reactant conversions below 10% to ensure differential conditions where primary reactions prevail. Net reaction rates ($\mathrm{r_{net,i}}$) were reported as moles of reactant converted per unit time per weight of catalyst (w), with the assumption that the differential plug flow reactor could be treated as a continuous stirred tank reactor (CSTR).(Massalmi & Maymó, 1969) The net reaction rates were thus estimated as:

$$\mathrm{r_{net,i}} = \frac{\mathrm{F_i} - \mathrm{F_i^0}}{\mathrm{w}} \tag{S5}$$

Where, $\mathrm{F_i^0}$ and $\mathrm{F_i}$ are the inlet and outlet molar flows, respectively, of the reactants and products. The forward CH_4 turnover rate ($\mathrm{r_{f,CH_4}}$), that is net CH_4 rate per exposed Ni active site ($\mathrm{M_{Ni}}$) and corrected from the approach to thermodynamic equilibrium ($1 - \eta_\mathrm{n}$), is expressed as:(Wei & Iglesia, 2004b)

$$r_{f,CH_4} = \frac{r_{net,CH_4}}{M_{Ni}(1-\eta_{DRM})} \quad \text{(S6)}$$

Where, η_n is the approach to equilibrium parameter of the dry reforming reaction that was evaluated according to **eq S7**:(Wei & Iglesia, 2004b)

$$\eta_{DRM} = \frac{p_{H_2}^2 p_{CO}^2}{p_{CH_4} p_{CO_2}} \frac{1}{K_{eq,DRM}} \quad \text{(S7)}$$

Where, $K_{eq,DRM}$ is the reaction equilibrium constant of the dry reforming reaction at a given temperature, p_i is the average of inlet and outlet i–th compound partial pressure in the catalytic bed (atm). The equilibrium constants were estimated by performing calculations with Aspen Plus® (AspenTech) using a model for a Gibbs reactor and the ideal gas package. The selectivity (s_i) were reported as the ratio net rate of i–th product to the total net rate of formation of the products as in **eq S8**:

$$s_i = \frac{r_i}{\sum r_i} = \frac{F_i - F_i^0}{\sum (F_i - F_i^0)} \quad \text{(S8)}$$

Mass balances were defined as the ratio of the total mass of an atomic Z species; namely carbon, oxygen, or hydrogen, leaving the reactor to that entering it (**eq S9**). Steady state carbon balances around 1.000 ± 0.005 (standard deviation) were achieved during all reaction tests. This suggested that the catalyst did not undergo appreciable carbon deposition during the reaction tests. On the other hand, the water molar flow at the exit of the reactor was estimated from the coupling of the carbon, oxygen, and hydrogen elemental balances (**eq S10**) since its quantification by online–GC was unfeasible.

$$ZB = \frac{\sum_i N_{z,i} * F_i}{\sum_i N_{z,i} * F_i^0} \quad \text{(S9)}$$

$$F_{H_2O} = \frac{1}{2}\left[(F_{CO} - F_{CO}^0) - \left(F_{H_2} - F_{H_2}^0\right)\right] \quad \text{(S10)}$$

Where, ZB represents the mass balance for a given Z species (i.e. C, O or H), and $N_{Z,i}$ the number of Z species atoms present in the i–th compound.

Section B. Experimental Design

The experimental planning of the catalytic tests was based on factorial experimental designs. The advantages of this kind of approach is that allows to recognize, if exist, iterative effects, reduce the number of experiments and provide statistical support to the trends observed in the rate data.(Montgomery, 2012) Here, two sets of experiments were made following a central composing design (or CCD) with eight cubic experimental points, six axial points, and three replicates at the center point were done. In the first set, the CH_4 and CO_2 partial pressure, and temperature were varied, while in the second set, the CO and H_2 pressure as well as the temperature were changed using a CH_4 and CO_2 pressure of 39.0kPa for both CH_4 and CO_2. **Table S1** shows the level values of the partial pressures and temperature in the experimental design as well as their corresponding net rates of CH_4, CO_2, CO, H_2 and H_2O. Therein, the axial points were estimated from **eq S11**:

$$X_{\pm\alpha} = X_0 \pm \frac{\alpha}{2} * (X_{+1} - X_{-1}) \quad \text{(S11)}$$

Where, X is the value of the independent variables at the axial points ($X_{\pm\alpha}$), central point (X_0), highest (X_{+1}) and lowest (X_{-1}) cubic points, and α (1.7) the distance from the center point to the axial points.

Table S1. *Details of the central composing design.*

Experimental set	Input variables	Level				
		−α	**+1**	**0**	**+1**	**+α**
First	CH_4 or CO_2 pressure (kPa)	16.9	29.0	39.0	52.0	61.1
Second	H_2 or CO pressure (kPa)	0.3	2.6	5.9	9.1	11.4
First and second	Temperature (K)	838	873	923	973	1008

First experimental set							
Level			**Net rate (mol kg^{-1} s^{-1})**				
Temp.	**CH_4 pressure**	**CO_2 pressure**	**CH_4**	**CO_2**	**CO**	**H_2**	**H_2O**
0	0	0	0.54	0.71	1.22	0.71	0.25
+1	+1	+1	0.82	1.14	1.90	1.02	0.44
+α	0	0	1.14	1.45	2.55	1.53	0.51
−α	0	0	0.22	0.32	0.49	0.18	0.15
–1	–1	+1	0.22	0.35	0.52	0.17	0.17
0	−α	0	0.36	0.57	0.96	0.40	0.28
–1	–1	–1	0.30	0.47	0.71	0.36	0.18
0	+α	0	0.84	0.98	1.62	1.01	0.30
0	0	0	0.55	0.74	1.22	0.71	0.26
+1	+1	–1	0.87	0.98	1.78	1.29	0.24
0	0	+α	0.47	0.73	1.30	0.64	0.33
+1	–1	–1	0.72	0.93	1.68	1.12	0.28
–1	+1	–1	0.46	0.57	1.07	0.64	0.22
–1	+1	+1	0.37	0.42	0.71	0.35	0.18
0	0	−α	0.66	0.74	1.40	1.04	0.18
+1	–1	+1	0.56	0.90	1.41	0.72	0.34
0	0	0	0.57	0.73	1.43	0.82	0.31

Second experimental set							
Level			**Net rate (mol kg^{-1} s^{-1})**				
Temp.	**CO pressure**	**H_2 pressure**	**CH_4**	**CO_2**	**CO**	**H_2**	**H_2O**
0	0	0	0.54	1.52	1.87	0.05	0.91
−α	0	0	0.12	0.63	0.71	–0.34	0.52
–1	+1	+1	0.23	1.17	1.37	–0.66	1.01
+1	–1	+1	0.89	2.23	3.10	0.07	1.51
+1	+1	+1	0.94	2.39	3.24	0.11	1.57
0	0	−α	0.60	0.91	1.32	0.76	0.28
–1	–1	+1	0.35	1.41	1.54	–0.50	1.02
–1	+1	–1	0.33	0.79	1.08	0.11	0.49
+1	+1	–1	0.92	1.55	2.95	0.87	1.04
0	0	0	0.68	1.48	2.05	0.26	0.89
+α	0	0	1.16	2.39	3.38	0.69	1.35
0	0	+α	0.56	1.85	2.26	–0.46	1.36
+1	–1	–1	1.07	1.76	2.64	1.06	0.79
–1	–1	–1	0.32	0.73	1.07	0.18	0.44
0	−α	0	0.59	1.36	1.87	0.29	0.79
0	+α	0	0.63	1.37	2.04	0.25	0.89
0	0	0	0.61	1.41	2.30	0.10	1.10

The CCD is based on a surface response optimization methodology to fit the following second–order polynomial model:(Asadzadeh et al., 2018)

$$Y = \beta_0 + \sum_{i=1}^{k} \beta_i X_i + \sum_{i=1}^{k} \beta_{ii} X_{ii}^2 + \sum_{i=1}^{k-1} \sum_{j=2}^{k} \beta_{ij} X_i X_j + \varepsilon \qquad i \neq j \tag{S12}$$

Where, Y represents a given response variable, X_i and X_j are the input variables of the experiment, and β_0, β_i, β_{ii}, and β_{ij} are coefficients representing the intercept, linear, quadratic, and interaction effects over the response variable, respectively. On the other hand, the random error (ε) term expresses the measure of the difference between the observed and the values predicted by the model. The statistical analysis of the results was performed with the Minitab® software (Minitab). Pareto charts were made to assess the effect of each input factor on the net reaction rates, **Figure S2**. Normal probability plots were used to verify the assumption that the residuals are normally distributed. In addition, the assumption of constant variance was tested by doing plots of the residuals of the surface response model of the data versus the predicted values and of the residuals versus the order of the catalytic runs.(Montgomery, 2012; NIST, 2013) **Figure S3** summarizes all the residual test plots for the specific case of the net CO reaction rate given that the other net reaction rates behaved similarly. As observed, the assumption that the residuals are normally distributed (**Figure S3A, D**) was fulfilled because of the linear trend as well as the high *p*–values obtained in the Anderson–Darling (AD) test. The assumption that the residuals have constant variance (**Figure S3B, E**) is also satisfied given that the residual points fell randomly on both sides of zero with no recognizable patterns. Finally, the assumption that the residuals are independent (**Figure S3C, F**) were confirmed since there were no trends or patterns in the residuals when displayed in order of execution.

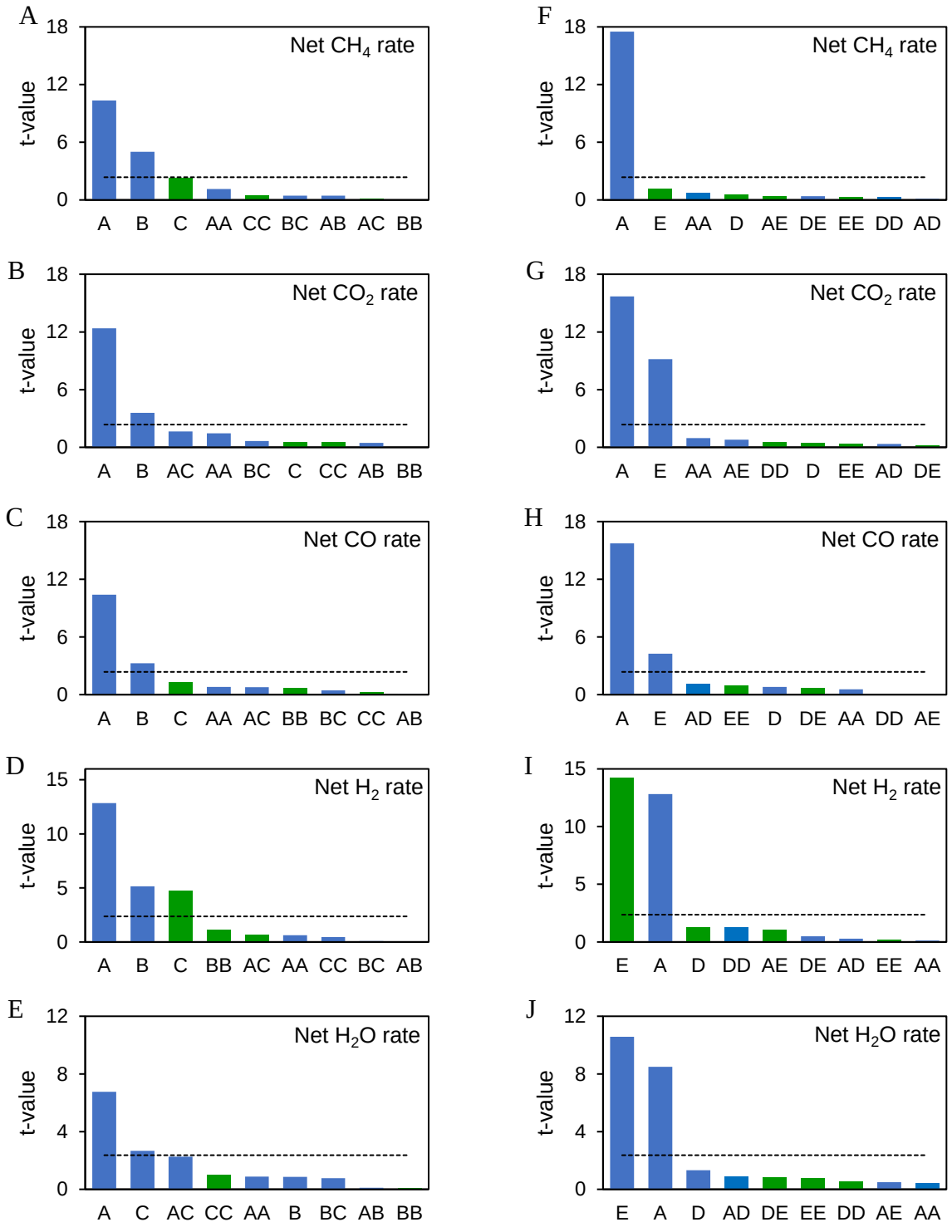

Figure S2. Pareto charts for the first (A–E) and second (F–J) experimental block. Temperature (A) was tested in K, while the CH_4 (B), CO_2 (C), CO (D) and H_2 (E) partial pressure in kPa. Positive and negative effects are denoted with color blue and green, respectively. Dash horizontal lines correspond to the tabulated *t*–value at a confidence level of 95%, with $n_{exp} - n_p$ (i.e., 7) degrees of freedom.

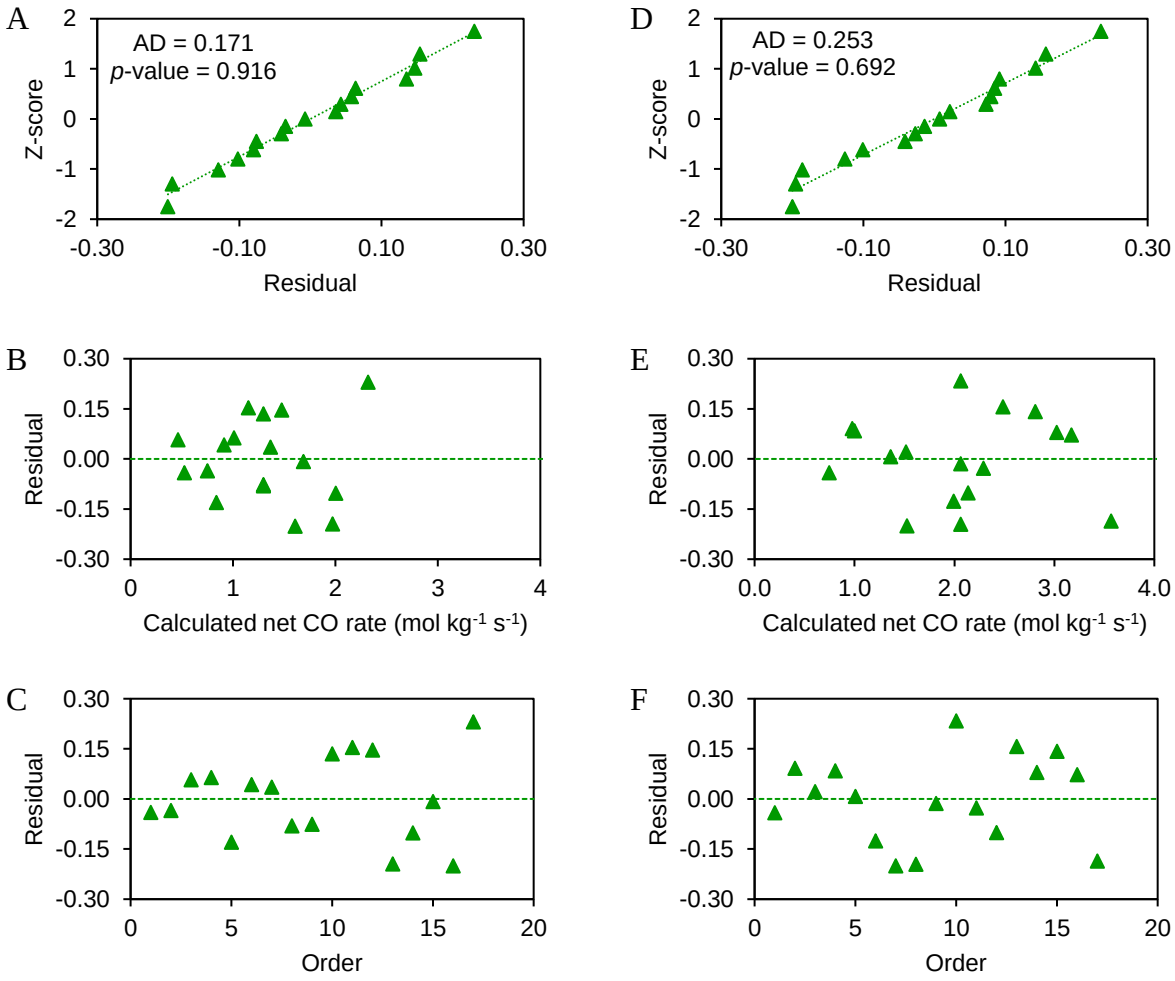

Figure S3. Residuals analysis plots: normality (A and D; the Anderson–Darling (AD) test was used to assess normality), residuals versus fits (B and E) and residuals versus experiment run order (C, F) for the net CO rate in the first (A–C) and second (D–F) experimental block. Residual was defined as the difference between the experimental and calculated values.

Section C. Assessment of Mass and Heat Transfer Limitations

In order to study the intrinsic kinetics of a catalytic reaction, it is required that the operational conditions guarantee the absence of heat and mass gradients in the reactor, i.e., the reactor must be operated under a regime of strict kinetic control.(Vannice, 2005) In this sense, the following conditions must be met: negligible radial and axial dispersion effects, sufficiently small radial and axial temperature gradients, absence of interfacial and intraparticle mass and heat transfer limitations, and low–pressure drop across the catalytic bed.(Minette et al., 2018) The

criteria considered to assess the above conditions are summarized in **Table S2**. Therein, the values of A (except for the first and third expression) and B were obtained considering a maximum relative difference between the observed and intrinsic net rates (Δr_{rel}) of 5% as recommended by Mears(Mears, 1971b), apparent activation energy (E_a) of 64kJ.mol^{-1}, reaction order (n) of 1, net CH_4 rate (r_A) of 1.10mol.kg^{-1}.s^{-1} measured at 1008K, catalyst particle density (ρ_c) of 3200kg.m^{-3} estimated by Archimedes' principle as well as the empiric correlations in **eq S13–S39**. The details of the performed calculations can be found in **Table S3**. In general, all the above–mentioned conditions were met, i.e., all inequalities in **Table S2** (A < B) were fulfilled, so mass and heat transfer limitations were ruled out.

Table S2. *Criteria to ensure the regime of kinetic control.*

Criteria	Expression (A < B)	A	B	Reference
Axial dispersion	$20 < \frac{L}{d_p}$	20	23	(Carberry & Wendel, 1963)
	$\frac{r_A \rho_b d_p}{C_0 u_s} < Pe_{Da}$	0.1	0.5	(Young & Finlayson, 1973)
Radial dispersion	$10 < \frac{d_t}{d_p}$	10	45	(Chu & Ng, 1989)
Radial temperature difference	$\Delta T_{r,B} = \left(1 + 8Bi_w \frac{d_p}{d_t}\right) \frac{\lvert\Delta H\rvert r_A \rho_B d_t^2}{32\lambda_{r,eff}} < \Delta r_{rel} \frac{RT_w^2}{E_a}$	5.9	6.7	(Mears, 1971a, 1971b)
Interphase heat transfer limitations	$\Delta T_{gs} = \frac{\lvert\Delta H\rvert r_A \rho_c d_p}{6h_{gs}} < \Delta r_{rel} \frac{RT^2}{E_a}$	5.2	6.6	(Mears, 1971a, 1971b)
Intraparticle heat transfer limitations	$\Delta T_{int,s} = \frac{\lvert\Delta H\rvert r_A \rho_c d_p^2}{60\lambda_c} < \Delta r_{rel} \frac{RT^2}{E_a}$	0.1	6.6	(Anderson, 1963)
Interphase mass transfer limitations ($\times 10^{-4}$)	$\Delta C_{A,gs} = \frac{r_A \rho_c}{k_{gs} a_{vs}} < \Delta r_{rel} \frac{C_A}{n}$	0.1	2.3	(Mears, 1971b)
Intraparticle mass transfer limitations	$\phi = \left(\frac{n+1}{2}\right) \frac{r_A \rho_c}{D_{A,eff} C_{As} a_{vs}^2} < 1$	0.1	1.0	(Weisz & Prater, 1954)
Small pressure drop	$\Delta P < 0.2 \frac{P_t}{n}$	0.3	26	(Minette et al., 2018)

Table S3. *Parameters employed to assess the mass and heat transfer limitation criteria.*

Parameter	Value	Comments
Bulk fluid temperature (K)	1008	T
Inner reactor wall temperature (K)	1013	T_w
Total pressure (kPa)	130	P
CH_4:CO_2:N_2 molar fraction	0.3:0.3:0.4	y_i
Total flow at normal conditions, i.e. at 298K–100kPa ($m^3\ s^{-1}$)	6.67×10^{-6}	Q_i
Total flow at 1008K–130kPa ($m^3\ s^{-1}$)	1.75×10^{-5}	Q_i
Net CH_4 reaction rate (kmol $kg^{-1}\ s^{-1}$)	1.10×10^{-3}	r_A
Activation energy (kJ $kmol^{-1}$)	6.33×10^{4}	E_a
CH_4 reaction order	1.00	n
Standard reaction enthalpy at 1008K (kJ $kmol^{-1}$)	2.60×10^{5}	$\Delta H^0_{r,n}$ (Çengel & Boles, 2015)
Particle diameter (m)	2.32×10^{-3}	d_p
Inner tube diameter (m)	1.05×10^{-2}	d_t
Catalyst density (kg m^{-3})	3200	ρ_c
Catalyst BJH pore volume ($m^3\ kg^{-1}$)	3.30×10^{-5}	v_p
Catalyst internal void fraction or porosity	0.11	$\varepsilon_c = \rho_c v_p$
Catalyst tortuosity	3.25	τ_c, a = 1 eq S19
Nickel volumetric fraction	0.21	v_m
Nickel thermal conductivity (kW $m^{-1}\ K^{-1}$)	7.23×10^{-2}	λ_m (Powell et al., 1965)
Lanthanum oxide thermal conductivity (kW $m^{-1}\ K^{-1}$)	2.20×10^{-3}	λ_s (Fornarini et al., 2008)
Catalyst thermal conductivity (kW $m^{-1}\ K^{-1}$)	3.75×10^{-3}	λ_c, eq S30
Quartz density (kg m^{-3})	2100	ρ_d (Sergeev et al., 1982)
Quartz thermal conductivity (kW $m^{-1}\ K^{-1}$)	1.92×10^{-3}	λ_d (Sergeev et al., 1982)
Volumetric bed dilution	0.99	v_b
Bed density (kg m^{-3})	1100	ρ_b
Bed porosity	0.48	$\varepsilon_b = 1 - \frac{\rho_d}{\rho_b}$
Bed tortuosity	1.40	τ_b, a = 0.5 eq S19
Bed thermal conductivity (kW $m^{-1}\ K^{-1}$)	1.93×10^{-3}	λ_b, eq S31
Bed length (m)	5.30×10^{-3}	L
External particle surface per unit volume particle (m^{-1})	2.58×10^{4}	$a_{vs} = \frac{6}{d_p}$

Table continuation

Parameter	Value	Comments
Superficial velocity (m s^{-1})	0.20	$u_s = \frac{2Q_t}{\pi d_t^2}$
Gas density (kg m^{-3})	0.45	ρ_g, eq S13
Gas viscosity (Pa s^{-1})	3.68×10^{-5}	μ_g, eq S22–25
Gas heat capacity (kJ kg^{-1} K^{-1})	2.03	C_{Pg}, eq S28–29
Gas thermal conductivity (kW m^{-1} K^{-1})	8.14×10^{-5}	λ_g, eq S26–27
Diffusivity of CH_4 in the gas mixture (m^2 s^{-1})	1.25×10^{-4}	$\mathcal{D}_{Ag}$, eq S14–17
Effective diffusivity of CH_4 in the catalyst (m^2 s^{-1})	4.06×10^{-6}	$\mathcal{D}_{A,eff}$, eq S18
Particle Reynolds number	0.58	$Re_p = \frac{d_p \rho_g u_s}{\mu_g}$
Schmidt number	0.65	$Sc = \frac{\mu_g}{\rho_g \mathcal{D}_{Ag}}$
Prandtl number	0.92	$Pr = \frac{C_{Pg}\mu_g}{\lambda_g}$
Péclet number for axial mass transport	0.51	Pe_{Da}, eq S20–21
Effective radial thermal conductivity of the bed (kW m^{-1} K^{-1})	3.41×10^{-4}	$\lambda_{r,eff}$, eq S32
Gas–solid mass transfer coefficient (m s^{-1})	0.93	k_{gs}, eq S34, S36
Gas–solid heat transfer coefficient (kW m^{-2} K^{-1})	0.68	h_{gs}, eq S35–36
Pressure drop (kPa)	0.31	ΔP, eq S37–40
Damköhler number for interphase heat transfer	1.55×10^{-2}	$Da_{h,gs} = \frac{\Delta H\, r_A \rho_c d_p}{2h_{gs}T}$
Arrhenius number	7.64	$Ar = \frac{E_a}{RT}$
Dimensionless heat generation function	1.30×10^{-3}	$\beta = \frac{\Delta H\, \mathcal{D}_{A,eff} C_A}{\lambda_c T}$
Thermal Biot number at the wall	0.85	Bi_w

Diffusivity of A in the gas mixture ($\mathcal{D}_{ig}$), m^2 s^{-1}. The diffusivity of gases at low density can be calculated with **eq S13**, which is known as Chapman–Enskog equation whose parameter values are depicted in **Table S4**.(McCabe et al., 2005) The expression for the diffusivity of A in

the gas mixture (**eq S16**) was developed considering that all components diffuse at the same rate.(Betancourt, 2008)

$$\mathcal{D}_{Ai} = 1.858 \times 10^{-7} \frac{T^{1.5}[(M_A + M_i)/M_A M_i]^{0.5}}{\left(\frac{\sigma_A+\sigma_i}{2}\right)^2 \Omega_{\mathcal{D}} P} \tag{S13}$$

$$\Omega_{\mathcal{D}} = \frac{1.06036}{(T_{Ai}^*)^{0.1561}} + \frac{0.193}{\exp(0.47635 T_{Ai}^*)} + \frac{1.03587}{\exp(1.52996 T_{Ai}^*)} + \frac{1.76474}{\exp(3.89411 T_{Ai}^*)} \tag{S14}$$

$$T_{Ai}^* = \frac{T}{\left(\frac{\epsilon_A}{\kappa}\frac{\epsilon_i}{\kappa}\right)^{\frac{1}{2}}} \tag{S15}$$

$$\mathcal{D}_{Ag} = \frac{1 - y_A}{\sum \frac{y_i}{\mathcal{D}_{Ai}}} \tag{S16}$$

Where, for the i–th compound, M_i is molecular weight, y_i the molar fraction and P the total pressure.

Table S4. *Parameters used to estimate the gas–phase properties*

Component	M_i (g mol^{-1})	ϵ_i/κ_i (K)	σ_i (Å)	C_{P_i} (kJ kmol^{-1} K^{-1})			
				a	b (×10^{-2})	c (×10^{-5})	d (×10^{-9})
CH_4	16.043	148.6	3.758	19.89	5.0240	1.2690	–11.0100
CO_2	44.010	195.2	3.941	22.26	5.9810	–3.5010	7.4690
H_2	2.016	59.7	2.827	29.11	–0.1916	0.4003	–0.8704
CO	28.011	91.7	3.690	28.16	0.1675	0.5372	–2.2220
H_2O	18.015	809.1	2.641	32.24	0.1923	1.0550	–3.5950
N_2	28.013	71.4	3.798	28.90	–0.1571	0.8081	2.8730

Effective diffusivity of A in the catalyst ($\mathcal{D}_{A,eff}$), m^2 s^{-1}. The effective diffusivity of the reacting species A in the catalyst pore is described in **eq S17**. Therein, the catalyst tortuosity (τ_c) is defined as the ratio of the actual distance a molecule travels between two points and the shortest distance between those two points.(Fogler, 1999) One of the most used models of tortuosity is a

logarithmic function of catalyst porosity (ε_c, **eq S18**), where, a is a constant found experimentally to be 0.77 for freely overlapping squares, 0.50 for randomly overlapping spheres of either uniform or non–uniform sizes and 1.00 for high–porosity beds composed of fibers.(Ghanbarian et al., 2013)

$$\mathcal{D}_{A,eff} = \frac{\varepsilon_c}{\tau_c}\mathcal{D}_{Ag} \tag{S17}$$

$$\tau_c = 1 - a\ln(1-\varepsilon_c) \tag{S18}$$

Péclet number for axial mass transport (Pe_{Da}). An accurate mathematical model for the axial dispersive Péclet number in chemical packed beds (**eq S19**) was reported for the range of particle Reynolds number (Re_p) of $0.02 \leq Re_p \leq 89.1$.(de Carvalho & Delgado, 2003) This expression is recommended for random packing of spherical particles that were well–packed,(Delgado, 2006) where Sc is the Schmidt number.

$$\frac{1}{Pe_{Da}} = \frac{Re_p Sc}{5}(1-p)^2 + \frac{(Re_p Sc)^2}{25}p(1-p)^3\left\{\exp\left[-\frac{5}{Re_p Sc\, p(1-p)}\right]-1\right\} + \frac{1}{\tau_b Re_p Sc} \tag{S19}$$

$$p = \frac{0.48}{Sc^{0.15}} + \left(0.5 - \frac{0.48}{Sc^{0.15}}\right)\exp\left(-\frac{75}{Re_p}\right) \tag{S20}$$

Gas–phase viscosity (μ_g), Pa s^{-1}. The gas viscosity for gases at low pressure can be estimated through the Chapman–Enskog equation (**eq S21**) with an average error of 2–3% (**Table 4S**).(McCabe et al., 2005) The viscosity of a gas mixture of known composition can be calculated with **eq S24**, which is simple and sufficiently accurate.(Betancourt, 2008)

$$\mu_i = 2{,}6693 \times 10^{-6}\frac{(TM_i)^{0,5}}{{\sigma_i}^2\Omega_\mu} \tag{S21}$$

$$\Omega_\mu = \frac{1.16145}{(T_i^*)^{0.14874}} + \frac{0.52487}{\exp(0.7732T_i^*)} + \frac{2.16178}{\exp(2.43787T_i^*)} \tag{S22}$$

$$T_i^* = \frac{T}{\frac{\epsilon_i}{\kappa}} \tag{S23}$$

$$\mu_g = \frac{\sum \mu_i y_i \sqrt{M_i}}{\sum y_i \sqrt{M_i}} \tag{S24}$$

Gas–phase thermal conductivity (λ_g) and heat capacity (C_{P_g}), kW m^{-1} K^{-1} and kJ kg^{-1} K^{-1}, respectively. Eucken developed a simple semiempirical method to estimate the thermal conductivity of polyatomic gases at low density (**eq S25**).(Bird et al., 2007) Thermal conductivities for low–density gas mixtures (**eq S26**) can be estimated with a similar method to that provided for viscosity (**eq S24**). On the other hand, the heat capacity is usually calculated employing polynomic functions of the temperature such as **eq S27** (**Table S4**).(Çengel & Boles, 2015)

$$\lambda_i = \left(C_{P_i} + \frac{5}{4}\frac{R}{M_i}\right)\mu_i \tag{S25}$$

$$\lambda_g = \frac{\sum \lambda_i y_i \sqrt{M_i}}{\sum y_i \sqrt{M_i}} \tag{S26}$$

$$C_{P_i} = a + bT + cT^2 + dT^3 \tag{S27}$$

$$C_{P_g} = \sum C_{P_i} y_i \tag{S28}$$

Solid–phase thermal conductivity (λ_s), kW m^{-1} K^{-1}. Among the analytical models to estimate the effective thermal conductivity the most adequate for oxide supported metal catalysts is the Maxwell–Eucken (**eq S29**), while for packed beds made of small catalyst and diluent particles is medium theory (or EMT) model (**eq S30**).(J. Wang et al., 2006) The Maxwell–Eucken model assumes a dispersion of small spheres within a continuous matrix of a different component, while the EMT model assumes a completely random distribution of all the components.(J. Wang et al., 2006)

$$\lambda_c = \frac{\lambda_s v_s + \lambda_m v_m \frac{3\lambda_s}{2\lambda_s + \lambda_m}}{v_s + v_m \frac{3\lambda_s}{2\lambda_s + \lambda_m}} \quad \text{(S29)}$$

$$v_c \frac{\lambda_c - \lambda_b}{\lambda_c - 2\lambda_b} + v_d \frac{\lambda_d - \lambda_b}{\lambda_d - 2\lambda_b} = 0 \quad \text{(S30)}$$

Where, λ_i and v_i are the thermal conductivity and volumetric fraction of metal (m), support (s), catalyst (c), diluent (d) and packed bed (b), respectively.

Effective radial thermal conductivity of the bed ($\lambda_{r,eff}$), kW m^{-1} K^{-1}. The radial thermal conductivity correlations are usually linear functions of the particle Reynolds number as **eq S31** ($50 \leq Re_p \leq 300$),(de Matos et al., 2010) where, ε_b is the bed porosity.

$$\frac{\lambda_{r,eff}}{\lambda_g} = \frac{\lambda^0_{r.eff}}{\lambda_g} + 0.16 Re_p Pr \quad \text{(S31)}$$

$$\frac{\lambda^0_{r.eff}}{\lambda_g} = \left(\frac{\lambda_b}{\lambda_g}\right)^{0.28 - 0.757\log(\varepsilon_b) - 0.057\log\left(\frac{\lambda_b}{\lambda_g}\right)} \quad \text{(S32)}$$

Gas–solid mass (k_{gs}) and heat (h_{gs}) transfer coefficients, m s^{-1} and kJ m^{-2} K^{-1}, respectively. The Chilton–Colburn mass (j_D) and heat (j_H) factors are dimensionless groups widely used to estimate the gas–solid mass (**eq S33**) and heat (**eq S34**) transfer coefficients. The mass factor can be estimated via the Dwivedi–Upadhyay correlation (**eq S35**) that can be used in the range $0.01 \leq Re_p \leq 1.5 \times 10^4$,(Dwivedi & Upadhyay, 1977) and as a result of the Chilton–Colburn analogy ($j_D = j_H$) the heat factor is obtained.(Geankoplis, 1993)

$$k_{gs} = j_D \frac{u_s}{Sc^{\frac{2}{3}}} \quad \text{(S33)}$$

$$h_{gs} = j_H \frac{C_{P_g} \rho_g u_s}{Pr^{\frac{2}{3}}} \quad \text{(S34)}$$

$$\varepsilon_b j_D = \frac{0.765}{Re_p^{0.82}} + \frac{0.365}{Re_p^{0.386}} \quad \text{(S35)}$$

Where, Pr is the Prandtl number and u_s is the superficial velocity.

Total pressure drop (ΔP), kPa. The pressure loss due to friction between solid in the bed and the gas phase can be expressed with **eq S36**, where the friction factor (ψ) can be calculated via the Eisfeld–Schnitzlein equation (**eq S37**) if $Re_p \leq 2 \times 10^4 \, (1 - \varepsilon_b)$. This is an Ergun–type model that accounts for the influence of the container walls on the pressure drop.(Eisfeld & Schnitzlein, 2001)

$$\Delta P = \psi \frac{L \rho_g u_s^2}{2 \times 10^3 d_p} \left(\frac{1 - \varepsilon_b}{\varepsilon_b^3} \right) \quad \text{(S36)}$$

$$\psi = \frac{380 A_w^2 (1 - \varepsilon_b)}{Re_p} + \frac{2 A_w}{B_w} \quad \text{(S37)}$$

$$A_w = \frac{2 d_p}{3 d_t (1 - \varepsilon_b)} + 1 \quad \text{(S38)}$$

$$B_w = \left[1.15 \left(\frac{d_p}{d_t} \right)^2 + 0.87 \right]^2 \quad \text{(S39)}$$

Where, L is the packed bed length, d_p the particle diameter, and d_t the inner diameter of the reactor.

Section D. Estimation of the Parameters of the Kinetic Models

Estimation of the activation energies, standard enthalpy of surface reaction and adsorption as well as the implemented statistical and physicochemical criteria. The estimation of the parameters of the different kinetic models postulated was done by the minimization of the weighted sum of squares of the residuals (SSR) between the experimental ($F_{k,i}$) and model calculated ($\hat{F}_{k,i}$) outlet molar flows, according to the **eq S40**:

$$\mathrm{SSR}(\varphi) = \sum_{i=1}^{n_{resp}} w_i \sum_{k=1}^{n_{exp}} \left(F_{k,i} - \hat{F}_{k,i}\right)^2 \xrightarrow{\varphi_1,\varphi_2,\ldots,\varphi_n} \min \qquad \text{(S40)}$$

Where, φ is the optimal parameter vector, n_{exp} the number of experiments (i.e. 34), n_{resp} the number of responses; namely, the outlet molar flows of CH_4, CO_2, CO, H_2, and H_2O, and w_i the weight factor assigned to the i–th response that, in this study, were equally assigned to each experimental observation (i.e., 1/17). To find the global minimum of the objective function, a procedure that combines the Rosenbrock method(Rosenbrock, 1960) and a Levenberg–Marquardt algorithm(Marquardt, 1963), implemented as ODRPACK(Boggs et al., 1989), was employed. The former was applied at the initial stage of the calculations to bring a fast approximation of the optimal parameters, while the latter was run at the late stages of the optimization procedure.(Castillo-Araiza et al., 2015) The results of this regression procedure were evaluated on both a statistical and a physicochemical basis.

The statistical significance of the kinetic models was assessed by an *F*–test. The *F*–value was defined as the ratio of the mean regression sum of squares and the mean residual sum of squares divided by $n_{exp}n_{resp} - n_p$ (where, n_p is the number of parameters) degrees of freedom of the regression. The regression was considered statistically significant when the calculated *F*–value exceeded the tabulated *F*–value for a theoretical Fisher probability distribution with the same degrees of freedom. The significance of the individual parameters was evaluated by a *t*–test. If the calculated value exceeded the value tabulated for a theoretical *t*–Student probability distribution one at a selected confidence level, e.g., 95%, with $n_{exp}n_{resp} - n_p$ degrees of freedom, the parameter was considered to be statistically different than zero. In practice, adequate *F*– and *t*–values are in the order of 100–onward and 10–100, respectively.(Toch et al., 2015)

The criteria proposed by Boudart & Djega–Mariadassou(Boudart & Djega-Mariadassou, 1984) and further refined by Vannice et al.(Vannice et al., 1979) were used to assess the physicochemical consistency of the estimated kinetic parameters of the models. The first criterium that was tested states that the adsorption enthalpy (ΔH_j^0) is, with very few exceptions, exothermic, **eq S41**:

$$-\Delta H_j^0 > 0 \tag{S41}$$

The second criterium stipulates that the adsorption entropy of the adsorbed species (ΔS_j^0) must be higher than zero and lower than the corresponding standard entropy of the corresponding species in the gas phase (S_g) given their change from a three–dimensional gas phase state to a two–dimensional surface–adsorbed state, **eq S42**:

$$0 < \Delta S_n^0 < S_g \tag{S42}$$

Also, the following inequality must be fulfilled, **eq S43**:

$$41.8 < \Delta S_n^0 < 51.04 - 1.4\Delta H_j^0 \tag{S43}$$

Finally, the sum of the enthalpies (ΔH_n^0) and entropies (ΔS_n^0) for all independent reaction steps in the postulated reaction mechanism from reactants to products must be equal to the overalls reaction standard enthalpy (ΔH_r^0, **eq S44**) and entropy (ΔS_r^0, **eq S45**) of reaction, respectively.(Dumesic et al., 1993)

$$\Delta H_r^0 = \sum_j \sigma_n \Delta H_n^0 \tag{S44}$$

$$\Delta S_r^0 = \sum_j \sigma_n \Delta S_n^0 \tag{S45}$$

Where, σ_n is the stoichiometric number used to describe the number of times that each n–th elementary step must occur to complete the overall reaction.

The so–called Bayesian Information Criterion (or BIC) was as a tool for choosing the most adequate kinetic model. In this sense, the model producing the lowest BIC was preferred among a finite set of models, since lower BIC implies either fewer explanatory variables, better fit, or both, **eq S46**:(Kass & Raftery, 1995)

$$\mathrm{BIC} = \mathrm{N}\ln\left(\frac{\mathrm{RSS}}{\mathrm{N}}\right) + \mathrm{p}\ln\mathrm{N} \tag{S46}$$

Where, N is the number of data points, RSS is the sum of squared residuals, and *p* the number of model parameters.

Finally, the degree of rate control –DRC– ($X_{RCi,n}$ in **eq S47**) for each step of mechanism of kinetic model determined to be the most adequate was analyzed in order to assess their influence on the net dry reforming (or CH_4) rate. This was made by differentially increasing the original forward rate constant of the n−th step ($k_{n,0}$) to a new value (k_n), at the same time that all the equilibrium constants as well as the forward rate constants for the other steps were kept fixed ($k_{m\neq n,}$ K_n). Thus, the original net rate ($r_{i,0}$) change to a new value (r_i). The larger the value of X_{RC}, the bigger is the influence of this step on the overall reaction rate. A positive value indicates that increasing k_n will increase the net rate r_i, and the steps are termed as rate–determining steps (or RDS), while a negative value indicates the opposite, and the steps are termed as inhibition steps.(Campbell, 2017)

$$X_{RCi,n} = \left[\frac{\partial \ln r_i}{\partial \ln k_n}\right]_{k_{m\neq n,}K_n} \approx \left[\frac{\ln\left(r_i/r_{i,0}\right)}{\ln\left(k_n/k_{n,0}\right)}\right]_{k_{m\neq n,}K_n} \tag{S47}$$

In order to validate the differential approximation in **eq S47**, several increments on the rate constants were tested. After doing this, it was found that the calculated $X_{RC,n}$ values did not change significantly (< 2%) in the range from 2% to 15%. Thus, a differential increment of 10% was chosen. After such an increase in the rate constants, the CH_4 and CO_2 conversion were modified less than ± 1%, showing that the DRC analysis was performed within differential reaction conditions.

Estimation of entropy for gas–phase and adsorbed molecules as well as for the transition state complexes. The thermodynamic form of the rate transition state expression (k_n^{TST}) is given by eq S48, if the activation energy ($E_{a,n}^{TST}$) is calculated by means of eq S49, in the Arrhenius form, the pre–exponential factor (A_n^{TST}) become as stated in eq S50:(Chorkendorff & Niemantsverdriet, 2003)

$$k_n^{TST} = \frac{k_B T}{h} e^{\frac{\Delta S_n^{\ddagger}}{R}} e^{-\frac{\Delta H_n^{\ddagger}}{RT}} \quad \text{(S48)}$$

$$E_{a,n}^{TST} = RT^2 \frac{\partial}{\partial T} \ln(k_n^{TST}) = \Delta H_n^{\ddagger} + RT \quad \text{(S49)}$$

$$A_n^{TST} = \frac{e k_B T}{h} e^{\frac{\Delta S_n^{\ddagger}}{R}} \quad \text{(S50)}$$

Where, for the n–th reaction, $\Delta S_n^{\ddagger}$ and $\Delta H_n^{\ddagger}$ are the entropy and enthalpy difference between the reactants and the transition state, or the activation entropy and enthalpy, respectively, k_B the Boltzmann constant and h the Plank constant.

The theoretical calculations of standard molar entropy (i.e. at 100kPa or 1bar) of the gas–phase and adsorbed species as well as the transition states were carried out via the Sackur−Tetrode equation:(McQuarrie, 1973)

$$S_x^0 = R\ln(q_x) + RT\left[\frac{\partial \ln(q_x)}{\partial T}\right] \quad \text{(S51)}$$

where R is the universal gas constant and q_x the partition function describing translational, vibrational, and rotational degrees of freedom (DOF) which were selected based on three cases:

(1) The ideal 3D gas model for gas–phase molecules (i.e. CH_4, CO_2, H_2, CO, and H_2O):(McQuarrie, 1973)

$$S_{3D\ trans}^0 = R\ln\left[\left(\frac{2\pi M k_B T}{h^2}\right)^{3/2}\frac{k_B T}{P^o}\right] + \frac{5}{2}R \quad \text{(S52)}$$

$$S_{3D\ rot}^0 = \begin{cases} 0 & \text{, if monoatomic} \\ R\ln\left(\dfrac{8\pi^2 I k_B T}{\sigma h^2}\right) + R & \text{, if linear molecule} \\ R\ln\left[\dfrac{\sqrt{\pi I_A I_B I_C}}{\sigma}\left(\dfrac{8\pi^2 k_B T}{\sigma h^2}\right)^{3/2}\right] + \dfrac{3}{2}R & \text{, if nonlinear molecule} \end{cases} \quad \text{(S53)}$$

$$S_{3D\ vib}^0 = R\sum_i^{vib\ DOF}\left[\frac{1/T_i}{e^{1/T_i}-1} - \ln\left(1-e^{-1/T_i}\right)\right] \quad , T_i = \frac{k_B T}{h\upsilon_i} \quad \text{(S54)}$$

Where, M is the molecule mass (i.e. molecular weight/Avogadro number), h the planck constant, P^o the standard pressure (1bar), υ_i the frequency of the i–th vibrational mode, σ the symmetry number of the molecule, and I the moment of inertia given by:

$$I = \sum_i m_i d_i^2 \quad \text{(S55)}$$

Where, m_i is the mass of i–th atom in the molecule and d_i its distance from the rotational axis.

(2) The 2D hindered translator/hindered rotor model for adsorbed species, namely CO_2*, H_2O*, CO_2#, and CO#, CH_x*, H*, O*, and CO*: (Sprowl et al., 2016)

$$S^0_{\text{hin trans or rot}} = R\left(\frac{1/T_i}{e^{1/T_i}-1} - \ln\left(1-e^{-1/T_i}\right) - \frac{1}{2} - \frac{r_i}{2T_i}\frac{I_1(r_i/2T_i)}{I_0(r_i/2T_i)} + \ln\left[\left(\frac{\pi r_i}{T_i}\right)^{1/2} I_0\left(\frac{r_i}{2T_i}\right)\right]\right) \quad , r_i = \frac{W_i}{h\upsilon_i} \tag{S56}$$

Where, I_n is the n–th order modified Bessel function of the first kind, W_i the translational (W_{trans}) or rotational (W_{rot}) energy barrier, and υ_i the translational (υ_{trans}) or rotational (υ_{rot}) frequency given by:

$$\upsilon_{trans} = \sqrt{\frac{(\mathcal{M}/\mathcal{A})W_{trans}}{2M}} \quad \text{or} \quad \upsilon_{rot} = \frac{1}{2\pi}\sqrt{\frac{n^2 W_{rot}}{2I}} \tag{S57}$$

Where, n is the number of equivalent energy minima in a full rotation of the adsorbate, $\mathcal{M}/\mathcal{A}$ the number of surface sites per area that could be replaced by $\mathcal{M}/\mathcal{A} = b^2$ [(nearest neighbor distance)^2] for a surface with 4–fold symmetry (like FCC(100) faces) or by $\mathcal{M}/\mathcal{A} = \frac{\sqrt{3}}{2}b^2$ for a surface with 3–fold symmetry (like FCC(111)). The vibrational entropy is given by **eq S54** with 3N–3 (N is the number of atoms in the adsorbate) degrees of freedom.

(3) Finally, the 2D hindered translator (**eq S56**) without rotation for transition state complexes. In the recombination or dissociation steps, an atom is added or removed of a molecule, with which, the transition state complex can be approximated as the product (e.g. CO = *C–O*, H_2O = *H–OH*) or reactant (e.g. CH_4 = *H–CH_3*, CO_2 = *O–CO*) with a partially dissociated atom, hence losing its rotation degree of freedom and a normal mode of stretching (**eq S54**).(Campbell et al., 2013)

The total standard entropy for the i–th specie in its respective model is:

$$S^0_i = S^0_{i,trans} + S^0_{i,rot} + S^0_{i,vib} + S^0_{i,con} \tag{S58}$$

where S^{o}_{con} is a surface concentration–related entropy, i.e., for 3D gas–phase molecules is zero, and it is calculated as:(Campbell et al., 2016)

$$S^{0}_{con} = R - R \ln\left[e^{1/3}\left(\frac{P^{o}}{k_B T}\right)^{2/3}\frac{1}{\mathcal{M}/\mathcal{A}}\right] \quad \text{(S59)}$$

Herein, model La_2O_3(001) and Ni(111) surfaces were chosen, since they are the most thermodynamically stable surface of La_2O_3 hexagonal(Kang Li et al., 2019; S. Wang et al., 2017) and Ni face–centered cubic (FCC)(Fan et al., 2015; Yuan et al., 2016) crystallographic structure over the explored temperature range (838−1008 K). The binding energy, translational energy, and vibrational frequencies for O*, H*, CH_x*, OH* and CO* adsorbates over Ni(111) were taken from Bai et al.(Bai et al., 2019). For the case of CH_4*, CO_2*, H_2O*, CO#, and CO_2# species the binding energy and vibrational frequencies as well as those of gaseous molecules, namely CH_4, CO_2, H_2, CO, and H_2O, were estimated through spin–polarized DFT periodic calculations using the Vienna ab initio Simulation Package (VASP)(Kresse & Furthmüller, 1996) with the projector augmented–wave (PAW) pseudopotentials(Blöchl, 1994) and the Perdew–Wang (PW91) exchange–correlation functional(Perdew & Wang, 1992). The electronic energy was converged to 10^{-8}eV while the maximum force on each relaxed atom was converged to 0.02eV $Å^{-1}$ and the energy cutoff was set to 400eV. The Ni(111) and La_2O_3(001) surfaces were modeled by a four–layer slab with a 2×2 unit cell, corresponding to a surface coverage of 1/4 monolayer (ML) for a single adsorbate per unit cell. A vacuum layer of ~15Å was inserted in the *z*–direction of the unit cell. Methfessel–Paxton(Methfessel & Paxton, 1989) of order two and Gaussian smearing with a width of 0.2eV was used for the nickel and lanthanum oxide, respectively. A Γ–centered Monkhorst–Pack k–point mesh(Monkhorst & Pack, 1976) of (4×4×1) was employed. Gaseous molecules were confined within a 3x3 Ni(111)–like unit cell whose distance between periodic images was ~12Å. The

adsorption energy (E_{ads}) was defined as $E_{ads} = E_{total} - E_{clean} - E_{gas}$ where E_{total}, E_{clean}, and E_{gas} are the total energies of the Ni(111) or La_2O_3(001) slab with adsorbate, the clean slab, and the adsorbate species in the gas–phase, respectively. Vibrational frequencies were determined from the eigenvalues of the Hessian matrix for the minima energy configuration of each compound. Two displacements were used in all three Cartesian directions with a step size of 0.015Å for all atoms in the gaseous and adsorbed species, while the nickel and lanthanum oxide slab atoms were held fixed.

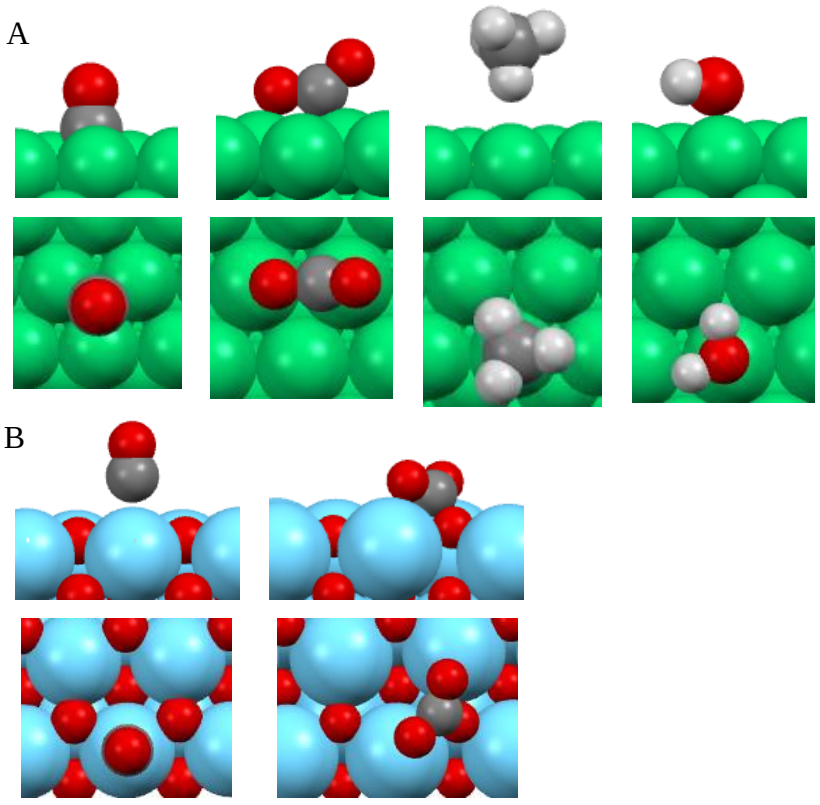

Figure S4. Top and side view of converged structures for adsorbates on the Ni(111) (A) and La_2O_3(001) (B) surfaces. Caption: green (Ni), red (O), gray (C), white (H), blue (La).

The simulation parameters were selected in order to achieve similitude between the results for CO adsorption over Ni(111) and those reported by Bai et al.(Bai et al., 2019), hence reducing the possibility of a systematic bias by incorporating uncorrelated data in entropy estimates (**Table**

S5). The calculated magnetic moment per Ni atom was $0.66\mu_B$, in comparison with the experimental value of $0.62\mu_B$.(Haynes, 2014) The converged structures are depicted in **Figure S4** while **Table S5** and **Table S6** summarize the obtained adsorption energies and some geometric parameters, and the vibrational frequencies, respectively. Finally, the estimated standard entropies for gaseous and adsorbed species (S^0_{ad}) as well as for the transition state (or TST) complexes are presented in **Table S7**. All these results agree with those reported theoretically and experimentally in literature, when available for comparison.

Table S5. *Estimated adsorption energies and geometric parameters of adsorbed species.*

Adsorbate	**E_{ads} (eV)**	**$Z_{A–S}$ (Å)**	**$d_{X–X}$ (Å)**	**$d_{A–B}$ (Å)**
Ni(111)			Ni–Ni	
Clean			2.496 (2.488[a])	
CO (hcp)	–1.96 (–1.99[a])	1.307 (1.311[a])	2.497 (2.496[a])	1.193 (1.197[a])
CO_2 (bridge)	0.12 (0.27[b])	1.836 (1.861[b])	2.507	1.246 (1.232[b])
CH_4 (top)	–0.06 (–0.02[c])	2.646	2.496	1.096 (1.089[b])
H_2O (top)	–0.24 (–0.29[c])	2.165 (2.260[d])	2.516	0.980
La_2O_3(001)			La–O	
Clean			2.354	
CO (top La)	–0.17 (–0.24[e])	1.170 (1.214[e])	2.359 (2.387[e])	1.142 (1.138[e])
CO_2 (bridge)	–0.64 (–0.51[e], –0.60[f])	1.037 (1.130[e], 1.090[f])	2.546 (2.523[e], 2.543[f])	1.263 (1.256[e], 1.264[f])

$Z_{A–S}$ is the vertical distance between the adsorbate and the plane of the surface atoms in contact with it, $d_{A–B}$ indicates the bond length between atoms A and B within an adsorbate, and $d_{X–X}$ corresponds to the distance between two adjacent surface atoms in contact with the adsorbate, see (Bai et al., 2019).

[a] PW91 (Bai et al., 2019)
[b] PBE (S.-G. Wang et al., 2007)
[c] PBE (Zhu et al., 2009)
[d] PBE (Murakhtina et al., 2006)
[e] PW91 (Manoilova et al., 2004)
[f] PBE (S. Wang et al., 2017)

Table S6. *Vibrational frequencies (in cm^{-1}) of each adsorbate on the surface.*

	Ni(111)				**La_2O_3(001)**	
	CO	**CO_2**	**CH_4**	**H_2O**	**CO**	**CO_2**
	hcp	**bridge**	**top**	**top**	**top La**	**top O**
Symmetric IM stretch	1767 (1866[a], 1810[b])	1107 (1129[c], 1137[d])	2947	3563 (3563[e])	2129 (2153[f], 2178[g], 2151[h])	1242 (1258[f], 1396[g])
Asymmetric IM stretch		1742 (1742[c])	3096	3668 (3664[e])		1631 (1691[f], 1604[g])
			3095			
			3043			
AS stretch	341 (349[a], 400[b])	292 (314[c], 371[d])	82	203 (174[e])	125	396
Symmetric deformation			1278			
Wagging		485 (508[c])	73	468 (513[e])		759 (773[g])
			67			
Scissoring		653 (645[c], 653[d])	1500	1538 (1536[e])		814 (842[f], 850[g])
			1501			
Rocking		167 (233[c])	1282	463 (392[e])		503
			1285			

IM stands for intramolecular, while AS stands for adsorbate–surface.

[a] PW91 (Bai et al., 2019)

[b] HREELS (Erley et al., 1979)

[c] PBE Ni(110) (Ding et al., 2007)

[d] HREELS Ni(110) (Ding et al., 2007)

[e] PBE (Murakhtina et al., 2006)

[f] PW91 (Manoilova et al., 2004)

[g] FTIR (Manoilova et al., 2004)

[h] FTIR (Tsyganenko et al., 1989)

Table S7. *Standard entropy estimates for the studied species at 923K.*

	Entropy (J mol^{-1} K^{-1})			
	Translational	**Rotational**	**Vibrational**	**Total**
Gas–phase				
CH_4	167	57	18	242 (242.1[c])
CO_2	180	70	14	263 (264.9[c])
H_2	141	22	1	165 (163.7[c])
CO	174	57		231 (232.0[c])
H_2O	168	58	3	229 (229.6[c])
Adsorbates[b]				
Ni(111)				
H*	29		5	57 (44[d])
C*	35		9	67
O*	39		10	72 (67[d])
CH*	38		51	112
CH_2* [a]	47	17	33	120
CH_3* [a]	51	20	49	143
CH_4*	55	14	67	158 (142[d])
CO*	57		57	137 (134[d])
CO_2*	63	28	61	175 (157[d])
OH*	54		53	130
H_2O*	55	12	43	134 (133[d])
La_2O_3(001)[b]				
CO_2#	62	28	44	157 (157[b])
CO#	59		59	142 (134[b])
TST complexes[b]				
CH_3–H	51		70	144
CH_3–HO	51		119	193
CH_2–H	47		42	112
CH–H	38		28	89
C–H	35		55	113
CO–O	57		49	129
C–O	35		43	101
O–H	39		37	99
OH–H	54		37	114
#CO–OC*	62		98	183
#CO–OH*	62		88	173

[a] The rotational energy barrier for CH_3* and CH_2* species were roughly assumed to be ~1% of their adsorption energy.(Sprowl et al., 2016)

[b] The concentration–related entropy (eq S59) for adsorbates and TST complexes at 923K was 57J.mol^{-1}.K^{-1}, however, to meet the thermodynamic consistency (eq S41–45), it was selected a standard coverage of 0.2 monolayer, with which this entropy was 23J.mol^{-1}.K^{-1}.

[c] Tabulated entropy by Cengel et al.(Çengel & Boles, 2015)

[d] $S^0_{ad}(T) = 0.70\ S^0_{gas}(T) - 3.3R$, this expression allows to estimate the standard entropies for adsorbed molecules (S^0_{ad}) directly from the entropy of the gas–phase molecule (S^0_{gas}) at the same temperature (T).(Campbell & Sellers, 2012)

Section E. Reaction Mechanisms and Kinetic Expressions

Table S8 summarize all the competing models that were discarded according to the statistical, *F*–value and BIC (**eq S46**), and thermodynamic, **eq S41–S45**, criteria. Therein, the model 1 was based on a single–site mechanism in which, both, CO_2 and CH_4 are activated over Ni–sites (symbolized by *). Specifically, it considers that the first C–H bond cleavage on methane takes places over a metal–metal site (*–*, step 1), which is followed by a cascade of C–H cleavage steps until chemisorbed C adatoms (step 3–5), in parallel to this, the CO_2 is adsorbed (step 12) and dissociated into chemisorbed CO and O (step 6); afterwards, the interaction between chemisorbed C and O adatoms produce another molecule of CO (step 7). Finally, the interaction of chemisorbed H and O adatoms produce OH species (step 10) which reacts with another H adatom to yield water (steps 13). The model 2 was based on the same considerations as those made for the model 1, but it contemplates that first C–H bond cleavage on methane takes places over both a metal–metal site (*–*, step 1) and metal–oxygen pair site (*–O*, step 2).

The model 3 considers a dual–site mechanism, where C–H bond in methane is activated over a metal–metal site as model 1 (step 1), while CO_2 is adsorbed over the La_2O_3 phase (denoted by #) generating an oxycarbonate species (CO_2#, step 15) that reacts with chemisorbed C adatoms to form CO* and CO# (step 8). In this case, it is assumed that CO_2# oxidizes the chemisorbed H adatoms into OH (step 11) which recombines with another chemisorbed H adatom to yield water (step 13). The model 4 was based on the same considerations as those made for the model 3, but it considers that the CO_2 is adsorbed over the interphase Ni–La_2O_3 sites (denoted by ^{IN}) leading to the formation of a bridged carbonate–like structure complex (CO_2^{IN}, step 16), where the oxygen atom of the CO_2 that does not interact with the $La_3^{+}{-}O_2^{-}$ acid–base pair sites is bound to the Ni–sites. The model 5 was based on the same considerations as those made for the model 1, but it

contemplates that CO_2 is adsorbed over both the Ni–sites (step 18) and the interphase Ni–La_2O_3 sites (step 16) as well as that the latter species contribute to the oxidation of chemisorbed carbon adatoms (step 12).

Table S8. *Dry reforming and RWGS reaction steps with their corresponding stoichiometric numbers (ν_i).*

Step	Elementary step	Dry reforming					RWGS					Kinetic descriptor
		ν_1	ν_2	ν_3	ν_4	ν_5	ν_1	ν_2	ν_3	ν_4	ν_5	
1	$CH_4 + * + * \rightleftharpoons CH_3* + H*$	1	1	1	1	2						k_1, K_1
2	$CH_4 + O* + * \rightleftharpoons CH_3* + OH*$		1									k_2, K_2
3	$CH_3* + * \rightleftharpoons CH_2* + H*$	1	2	1	1	2						k_3, K_3
4	$CH_2* + * \rightleftharpoons CH* + H*$	1	2	1	1	2						k_4, K_4
5	$CH* + * \rightleftharpoons C* + H*$	1	2	1	1	2						k_5, K_5
6	$CO_2* + * \rightleftharpoons CO* + O*$	1	2			1	1	1			1	k_6, K_6
7	$C* + O* \rightleftharpoons CO* + *$	1	2			1						k_7, K_7
8	$C* + CO_2\# \rightleftharpoons CO* + CO\#$			1								k_8, K_8
9	$C* + CO_2^{IN} \rightleftharpoons CO* + CO^{IN}$				1	1						k_9, K_9
10	$H* + O* \rightleftharpoons OH* + *$		–1				1	1			1	k_{10}, K_{10}
11	$H* + CO_2\# \rightleftharpoons OH* + CO\#$								1			k_{11}, K_{11}
12	$H* + CO_2^{IN} \rightleftharpoons OH* + CO^{IN}$									1		k_{12}, K_{12}
13	$OH* + H* \rightleftharpoons H_2O* + *$						1	1	1	1	1	k_{13}, K_{13}
14	$CO_2 + * \rightleftarrows CO_2*$	1	2			1	1	1			1	K_{CO_2}
15	$CO_2 + \# \rightleftarrows CO_2\#$			1					1			$K^{\#}_{CO_2}$
16	$CO_2 + {}^{IN} \rightleftarrows CO_2^{IN}$				1	1				1		$K^{IN}_{CO_2}$
17	$H_2 + * + * \rightleftarrows H* + H*$	–2	–4	–2	–2	–4	1	1	1	1	1	K_H
18	$CO + * \rightleftarrows CO*$	–2	–4	–1	–1	–3	–1	–1			–1	K_{CO}
19	$CO + \# \rightleftarrows CO\#$			–1					–1			$K^{\#}_{CO}$
20	$CO + {}^{IN} \rightleftarrows CO^{IN}$				–1	–1				–1		K^{IN}_{CO}
21	$H_2O + * \rightleftarrows H_2O*$						–1	–1	–1	–1	–1	K_{H_2O}
	Global reaction											
A	$CH_4 + CO_2 \rightleftharpoons 2CO + 2H_2$	1	2	1	1	2						
B	$CO_2 + H_2 \rightleftharpoons CO + H_2O$						1	1	1	1	1	

Key to symbols: *, an unoccupied metal site; #, an unoccupied oxide site; $\rightleftarrows$, a quasi–equilibrated step; and $\rightleftharpoons$, a reversible step; k_n and K_n are the forward reaction rate constant and the reaction equilibrium coefficient of the n–th elementary reaction step

The CO_2 and CO adsorption steps over both the support (#) and interphase (^{IN}) sites were assumed to be quasi–equilibrated, **eq S60**. Also, such adsorbates were accounted for the active site balances, **eq S61**:

$$[\mathrm{i^X}] = \mathrm{K_i^X}\frac{\mathrm{p_i}}{\mathrm{p^0}}\,[\mathrm{X}] \tag{S60}$$

$$[\mathrm{X}]_{\mathrm{tot}} = [\mathrm{CO_2^X}] + [\mathrm{CO^X}] + [\mathrm{X}] \tag{S61}$$

where, $\mathrm{p_i}$ is the partial pressure of the i–th specie, $\mathrm{p^0}$ the standard pressure (1bar or 100kPa), $[\mathrm{A^X}]$ is the surface concentration of the i–th specie over an X site, $[\mathrm{X}]$ is the concentration of free X active sites and $[\mathrm{X}]_{\mathrm{tot}}$ is the total concentration of X active sites that were considered to be 2 and 1μmol.g_{cat}^{-1} over the La_2O_3(S. Wang et al., 2017) and interphase(Foppa et al., 2017), respectively. The pseudo–steady state approximation was applied to the concentration of the intermediates,(Otyuskaya et al., 2018; Rajkhowa et al., 2017) with this, a system of differential–algebraic equations (or DAE) per model was obtained. For simplicity, only the kinetics expressions corresponding to the model 1 and 3 are presented:

- Model 1 (C–H bond cleavage over *–* sites)

$$\frac{\mathrm{dF_{CH_4}}}{\mathrm{dw}} = -k_1\frac{\mathrm{p_{CH_4}}}{\mathrm{p^0}}[*]^2 + \frac{k_1}{\mathrm{K_1}}[\mathrm{CH_3^*}][\mathrm{H^*}] \tag{S62}$$

$$\frac{\mathrm{dF_{CO_2}}}{\mathrm{dw}} = -k_6[\mathrm{CO_2^*}][*] + \frac{k_6}{\mathrm{K_6}}[\mathrm{CO^*}][\mathrm{O^*}] \tag{S63}$$

$$\frac{\mathrm{dF_{CO}}}{\mathrm{dw}} = k_6[\mathrm{CO_2^*}][*] - \frac{k_6}{\mathrm{K_6}}[\mathrm{CO^*}][\mathrm{O^*}] + k_7[\mathrm{C^*}][\mathrm{O^*}] - \frac{k_7}{\mathrm{K_7}}[\mathrm{CO^*}][*] \tag{S64}$$

$$2\frac{\mathrm{dF_{H_2}}}{\mathrm{dw}} = k_1\frac{\mathrm{p_{CH_4}}}{\mathrm{p^0}}[*]^2 - \frac{k_1}{\mathrm{K_1}}[\mathrm{CH_3^*}][\mathrm{H^*}] + \mathrm{k_3}[\mathrm{CH_3^*}][*] - \frac{k_3}{\mathrm{K_3}}[\mathrm{CH_2^*}][\mathrm{H^*}] + k_4[\mathrm{CH_2^*}][*] - \frac{k_4}{\mathrm{K_4}}[\mathrm{CH^*}][\mathrm{H^*}]$$
$$+ k_5[\mathrm{CH^*}][*] - \frac{k_5}{\mathrm{K_5}}[\mathrm{C^*}][\mathrm{H^*}] - k_{10}[\mathrm{H^*}][\mathrm{O^*}] + \frac{k_{10}}{\mathrm{K_{10}}}[\mathrm{OH^*}][*] - k_{13}[\mathrm{OH^*}][\mathrm{H^*}] \quad \text{(S65)}$$
$$+ \frac{k_{13}}{\mathrm{K_{13}}}[\mathrm{H_2O^*}][*]$$

$$\frac{\mathrm{dF_{H_2O}}}{\mathrm{dw}} = k_{13}[\mathrm{OH^*}][\mathrm{H^*}] - \frac{k_{13}}{\mathrm{K_{13}}}[\mathrm{H_2O^*}][*] \quad \text{(S66)}$$

$$k_1\frac{\mathrm{p_{CH_4}}}{\mathrm{p^0}}[*]^2 - \frac{k_1}{\mathrm{K_1}}[\mathrm{CH_3^*}][\mathrm{H^*}] - k_3[\mathrm{CH_3^*}][*] + \frac{k_3}{\mathrm{K_3}}[\mathrm{CH_2^*}][\mathrm{H^*}] = 0 \quad \text{(S67)}$$

$$k_3[\mathrm{CH_3^*}][*] - \frac{k_3}{\mathrm{K_3}}[\mathrm{CH_2^*}][\mathrm{H^*}] - k_4[\mathrm{CH_2^*}][*] + \frac{k_4}{\mathrm{K_4}}[\mathrm{CH^*}][\mathrm{H^*}] = 0 \quad \text{(S68)}$$

$$k_4[\mathrm{CH_2^*}][*] - \frac{k_4}{\mathrm{K_4}}[\mathrm{CH^*}][\mathrm{H^*}] - k_5[\mathrm{CH^*}][*] + \frac{k_5}{\mathrm{K_5}}[\mathrm{C^*}][\mathrm{H^*}] = 0 \quad \text{(S69)}$$

$$k_5[\mathrm{CH^*}][*] - \frac{k_5}{\mathrm{K_5}}[\mathrm{C^*}][\mathrm{H^*}] - k_7[\mathrm{C^*}][\mathrm{O^*}] + \frac{k_7}{\mathrm{K_7}}[\mathrm{CO^*}][*] = 0 \quad \text{(S20)}$$

$$k_5[\mathrm{CO_2^*}][*] - \frac{k_5}{\mathrm{K_5}}[\mathrm{CO^*}][\mathrm{O^*}] - k_7[\mathrm{C^*}][\mathrm{O^*}] + \frac{k_7}{\mathrm{K_7}}[\mathrm{CO^*}][*] - k_{10}[\mathrm{H^*}][\mathrm{O^*}] + \frac{k_{10}}{\mathrm{K_{10}}}[\mathrm{OH^*}][*] = 0 \quad \text{(S70)}$$

$$k_{10}[\mathrm{H^*}][\mathrm{O^*}] - \frac{k_{10}}{\mathrm{K_{10}}}[\mathrm{OH^*}][*] - k_{13}[\mathrm{OH^*}][\mathrm{H^*}] + \frac{k_{13}}{\mathrm{K_{13}}}[\mathrm{H_2O^*}][*] = 0 \quad \text{(S71)}$$

- Model 3 (CO_2 adsorption over # sites)

$$\frac{\mathrm{dF_{CH_4}}}{\mathrm{dw}} = -k_1\frac{\mathrm{p_{CH_4}}}{\mathrm{p^0}}[*]^2 + \frac{k_1}{\mathrm{K_1}}[\mathrm{CH_3^*}][\mathrm{H^*}] \quad \text{(S72)}$$

$$\frac{\mathrm{dF_{CO_2}}}{\mathrm{dw}} = -k_8[\mathrm{C^*}][\mathrm{CO_2^\#}] + \frac{k_8}{\mathrm{K_8}}[\mathrm{CO^*}][\mathrm{CO^\#}] \quad \text{(S73)}$$

$$\frac{\mathrm{dF_{CO}}}{\mathrm{dw}} = k_8[\mathrm{C^*}][\mathrm{CO_2^\#}] - \frac{k_8}{\mathrm{K_8}}[\mathrm{CO^*}][\mathrm{CO^\#}] + k_{11}[\mathrm{H^*}][\mathrm{CO_2^\#}] - \frac{k_{11}}{\mathrm{K_{11}}}[\mathrm{OH^*}][\mathrm{CO^\#}] \quad \text{(S74)}$$

$$2\frac{\mathrm{dF_{H_2}}}{\mathrm{dw}} = k_1\frac{\mathrm{p_{CH_4}}}{\mathrm{p^0}}[*]^2 - \frac{k_1}{\mathrm{K_1}}[\mathrm{CH_3^*}][\mathrm{H^*}] + k_3[\mathrm{CH_3^*}][*] - \frac{k_3}{\mathrm{K_3}}[\mathrm{CH_2^*}][\mathrm{H^*}] + k_4[\mathrm{CH_2^*}][*] - \frac{k_4}{\mathrm{K_4}}[\mathrm{CH^*}][\mathrm{H^*}] + k_5[\mathrm{CH^*}][*] - \frac{k_5}{\mathrm{K_5}}[\mathrm{C^*}][\mathrm{H^*}] - k_{11}[\mathrm{H^*}][\mathrm{CO_2^\#}] + \frac{k_{11}}{\mathrm{K_{11}}}[\mathrm{OH^*}][\mathrm{CO^\#}] - k_{13}[\mathrm{OH^*}][\mathrm{H^*}] + \frac{k_{13}}{\mathrm{K_{13}}}[\mathrm{H_2O^*}][*] \quad \text{(S75)}$$

$$\frac{\mathrm{F_{H_2O}}}{\mathrm{dw}} = k_{13}[\mathrm{OH^*}][\mathrm{H^*}] - \frac{k_{13}}{\mathrm{K_{13}}}[\mathrm{H_2O^*}][*] \quad \text{(S76)}$$

$$k_1\frac{\mathrm{p_{CH_4}}}{\mathrm{p^0}}[*]^2 - \frac{k_1}{\mathrm{K_1}}[\mathrm{CH_3^*}][\mathrm{H^*}] - k_3[\mathrm{CH_3^*}][*] + \frac{k_3}{\mathrm{K_3}}[\mathrm{CH_2^*}][\mathrm{H^*}] = 0 \quad \text{(S77)}$$

$$k_3[\mathrm{CH_3^*}][*] - \frac{k_3}{\mathrm{K_3}}[\mathrm{CH_2^*}][\mathrm{H^*}] - k_4[\mathrm{CH_2^*}][*] + \frac{k_4}{\mathrm{K_4}}[\mathrm{CH^*}][\mathrm{H^*}] = 0 \quad \text{(S78)}$$

$$k_4[\mathrm{CH_2^*}][*] - \frac{k_4}{\mathrm{K_4}}[\mathrm{CH^*}][\mathrm{H^*}] - k_5[\mathrm{CH^*}][*] + \frac{k_5}{\mathrm{K_5}}[\mathrm{C^*}][\mathrm{H^*}] = 0 \quad \text{(S79)}$$

$$k_5[\mathrm{CH^*}][*] - \frac{k_5}{\mathrm{K_5}}[\mathrm{C^*}][\mathrm{H^*}] - k_8[\mathrm{C^*}][\mathrm{CO_2^\#}] + \frac{k_8}{\mathrm{K_8}}[\mathrm{CO^*}][\mathrm{CO^\#}] = 0 \quad \text{(S80)}$$

$$k_{11}[\mathrm{H^*}][\mathrm{CO_2^\#}] - \frac{k_{11}}{\mathrm{K_{11}}}[\mathrm{OH^*}][\mathrm{CO^\#}] - k_{13}[\mathrm{OH^*}][\mathrm{H^*}] + \frac{k_{13}}{\mathrm{K_{13}}}[\mathrm{H_2O^*}][*] = 0 \quad \text{(S81)}$$

In the case of the models 4 and 5, the occupied IN–sites (i.e., $[\mathrm{CO_2^{IN}}] + [\mathrm{CO^{IN}}]$) must be added to the Ni–sites balance because a IN–site is formed by a metal–support pair site (*–#). Thus, such models can present two different behaviors depending on the standard adsorption entropy and enthalpy of the CO_2^{IN} and CO^{IN} species. The first case is that such adsorption parameters are greater than or equal to those of CO_2# and CO# species, i.e., a "weak" Ni–effect on the CO_2 and CO adsorption, with which the term $[\mathrm{CO_2^{IN}}] + [\mathrm{CO^{IN}}]$ reduce the availability of the free Ni–sites. The second is the opposite, a reduction in the standard adsorption entropy and enthalpy, i.e., a "strong" Ni–effect on the CO_2 and CO adsorption, in specific, these values were considered to be an average between those on Ni and La_2O_3, as a result the term $[\mathrm{CO_2^{IN}}] + [\mathrm{CO^{IN}}]$ virtually

disappears from the Ni–sites balance. The above scenarios were explored by means of the model 4, in the first and second case, this model was termed as model 4B and 4A, respectively. As observed in **Figure S5**, the model 4A presented the higher *F*–value and lower BIC (**eq S46**), which implies a better fitting of the experimental data, hence this case were considered for the model 5.

The parameter estimates from the weighted regression are presented in **Table S9**. The concordance between the experimental and calculated net rates with corresponding *F*–values and BIC is depicted in **Figure S5**. As observed, all models showed a *F*–value that exceeded the tabulated *F*–value of 2.79. Furthermore, all parameters were estimated statistically significant with *t*–values ranged in 10–400, which are larger than the tabulated *t*–value of 1.96. The physicochemical analysis of the kinetic and adsorption parameters showed that all adsorption enthalpies and entropies presented thermodynamic consistency (**eq S41–S45**) and both forward and reverse activation energies in the model were within the range 21–210kJ.mol^{-1}.(Santacesaria, 1997) Moreover, the overall dry reforming standard reaction enthalpy for all models were 260 ± 14kJ.mol^{-1} in close agreement with the experimental value of 260.3kJ.mol^{-1} at 923K.(Çengel & Boles, 2015)

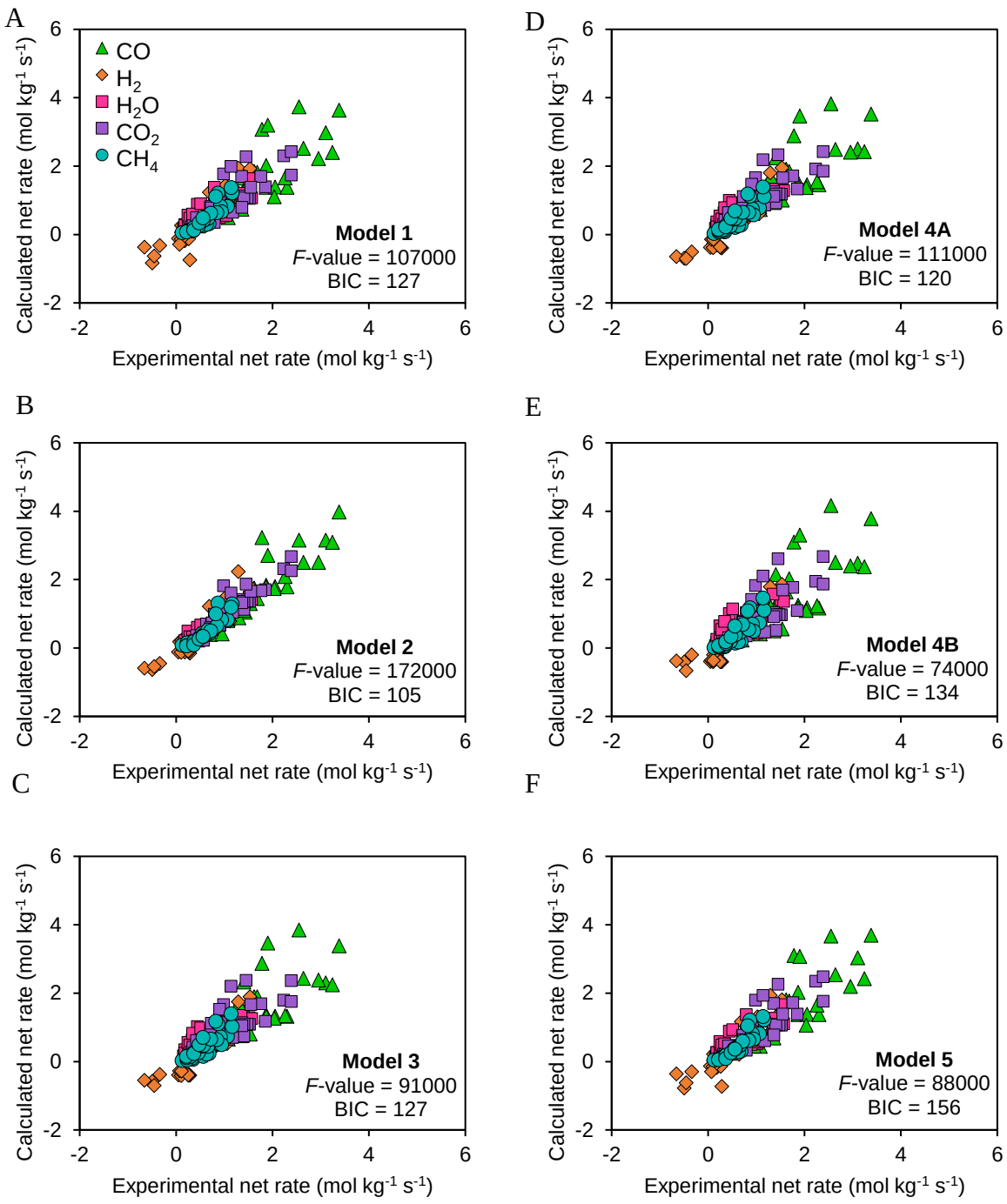

Figure S5. Parity diagrams for comparing the experimental and calculated net rates of reactants and products.

Table S9. *Kinetic parameters with their t–Student confidence intervals built at a 95% confidence level.*

Kinetic descriptor	A_n (kg mol^{-1} s^{-1})	Model 1	Model 2	Model 3	Model 4A	Model 4B	Model 5
		$E_{a,n}$ (kJ mol^{-1})					
k_1	2.3×10^{10} (7.6×10^{9})[c]	116 ± 1	115 ± 3	117 ± 1	118 ± 1	116 ± 1	116 ± 1
k_2	1.4×10^{9}		93 ± 1				
k_3	7.1×10^{13}	87 ± 6	88 ± 3	88 ± 6	88 ± 8	84 ± 7	83 ± 8
k_4	6.1×10^{13}	81 ± 5	80 ± 3	78 ± 8	78 ± 8	77 ± 2	75 ± 7
k_5	3.1×10^{15}	92 ± 5	90 ± 6	92 ± 10	94 ± 7	94 ± 6	92 ± 8
k_6	1.2×10^{13} (3×10^{14})[b]	68 ± 5	66 ± 2				79 ± 7
k_7	2.8×10^{13} (8×10^{13})[b]	94 ± 4	88 ± 4				88 ± 11
k_8	7.3×10^{13}			88 ± 3			
k_9	8.9×10^{13}				59 ± 5	89 ± 7	62 ± 5
k_{10}	7.4×10^{13}	94 ± 15	92 ± 4				91 ± 3
k_{11}	7.3×10^{13}			141 ± 3			
k_{12}	8.9×10^{13}				94 ± 1	144 ± 2	
k_{13}	4.1×10^{11} (2×10^{11})[b]	57 ± 3	53 ± 4	43 ± 5	47 ± 3	45 ± 3	52 ± 3
	ΔS_n^0 (J mol^{-1} K^{-1})	ΔH_n^0 (kJ mol^{-1})					
K_1	–43	–1 ± 1	–1 ± 1	–1 ± 1	–1 ± 1	–1 ± 1	–1 ± 1
K_2	–41		–11 ± 1				
K_3	34	48 ± 4	63 ± 8	55 ± 6	49 ± 4	57 ± 4	48 ± 4
K_4	49	55 ± 3	55 ± 2	49 ± 5	45 ± 4	48 ± 2	52 ± 4
K_5	12	–42 ± 3	–34 ± 1	–14 ± 2	–23 ± 2	–15 ± 1	–39 ± 5
K_6	34	–3 ± 1	–52 ± 3				–3 ± 1
K_7	–2	–75 ± 3	–43 ± 3				–57 ± 5
K_8	54			–24 ± 3			
K_9	45				–28 ± 1	–22 ± 2	–41 ± 3
K_{10}	2	19 ± 2	38 ± 2				22 ± 2
K_{11}	49			45 ± 7			
K_{12}	58				49 ± 7	43 ± 4	
K_{13}	–53	–37 ± 3	–28 ± 1	–39 ± 4	–37 ± 3	–39 ± 4	–39 ± 3
K_{CO_2}	–89	–12 ± 1	–15 ± 1				–13 ± 1
$K_{CO_2}^{\#}$	–106			–89 ± 2			
$K_{CO_2}^{IN}$	–97				–43 ± 1	–87 ± 4	–47 ± 5
K_H	–51	–60 ± 3	–67 ± 3	–66 ± 5	–60 ± 2	–64 ± 5	–59 ± 5
K_{CO}	–94	–84 ± 3	–89 ± 2	–86 ± 7	–85 ± 7	–85 ± 11	–88 ± 2
$K_{CO}^{\#}$	–89			–67 ± 8			
K_{CO}^{IN}	–89				–54 ± 4	–67 ± 5	–60 ± 4
K_{H_2O}	–96	–63 ± 3	–70 ± 3	–63 ± 6	–63 ± 5	–60 ± 4	–62 ± 2

Table continuation

	ΔS_n^0 (J mol^{-1} K^{-1})	ΔH_n^0 (kJ mol^{-1})					
DRM	286	260 ± 2	260 ± 8	261 ± 7	260 ± 4	260 ± 14	260 ± 6
RWGS	32	53 ± 3	35 ± 5	–19 ± 4	26 ± 5	–20 ± 9	58 ± 7

Pre–exponential factor for LH reactions according to Dumesic et al.(Dumesic et al., 1993): 10^{11}kg.mol^{-1}.s^{-1} for mobile transition state with rotation; 10^{13}kg.mol^{-1}.s^{-1} for mobile transition state without rotation; and 10^{15}kg.mol^{-1}.s^{-1} for immobile transition state without rotation.

[b] Theorical estimate via the methodology proposed by Campbell et al.(Campbell et al., 2013)

[c] Experimental estimate reported by Wei & Iglesia(Wei & Iglesia, 2004b)